A FINITE ELEMENT INVESTIGATION OF THE DEFORMATIONS, FORCES, STRESS FORMATIONS, AND ENERGY LOSSES IN ELASTO-PLASTIC SLIDING CONTACTS

A thesis
Presented to
The Academic Faculty

By

Raghvendra Vijaywargiya

In Partial Fulfillment
Of the Requirements for the Degree
Master of Science in Mechanical Engineering

Georgia Institute of Technology

August 2006

A FINITE ELEMENT INVESTIGATION OF THE DEFORMATIONS, FORCES, STRESS FORMATIONS, AND ENERGY LOSSES IN ELASTO-PLASTIC SLIDING CONTACTS

Approved by:

Dr. Itzhak Green, Advisor
G. W. W. School of Mechanical Engineering
Georgia Institute of Technology

Dr. Richard Neu
G. W. W. School of Mechanical Engineering
Georgia Institute of Technology

Dr. Jeffrey Streator
G. W. W. School of Mechanical Engineering
Georgia Institute of Technology

Date Approved: May 13, 2006

To my parents and friends

ACKNOWLEDGEMENTS

I am grateful to Dr. Itzhak Green for his unstinting support and guidance throughout my stay at Georgia Tech. I would like to thank Mr. John Moody for helping me finish all the analyses and making this a comprehensive piece of work. I am also thankful to the graduate students in the Tribology research group for all their help. Last but not least, I would like to thank my dear friends at Georgia Tech for making this a memorable experience.

This research is supported in part through the Department of Defense Multidisciplinary Research Program of the University Research Initiative as Office of Naval Research Grant N00014-04-1-0601, entitled "Friction & Wear under Very High Electromagnetic Stress." Dr. P. Peter Schmidt serves as Program Officer. Information conveyed in this manuscript does not necessarily reflect the position or policy of the Government, and no official endorsement should be inferred.

TABLE OF CONTENTS

LIST OF TABLES

LIST OF FIGURES

NOMENCLATURE

b = contact half width

C = critical yield stress coefficient

E = elastic modulus

E' = equivalent modulus of elasticity, $\frac{1}{E'} = \frac{1-\nu_1^{\,2}}{E_1} + \frac{1-\nu_2^{\,2}}{E_2}$

F_x = horizontal reaction force at the base of the bottom cylinder

F_y = vertical reaction force at the base of the bottom cylinder

i = load step number

L = length of contact

n = number of load steps employed to simulate a quasi-static sliding process

P = contact force

P^* = non-dimensional load, P / P_c

p_o = maximum contact pressure

R = radius of the cylinder

R = equivalent radius, $\frac{1}{R} = \frac{1}{R_1} + \frac{1}{R_2}$

S_y = yield strength

U = potential (strain) energy

u = maximum vertical displacement

x = horizontal sliding distance covered by the top cylinder up to the i^{th} load step

Δx = total horizontal distance covered by the top cylinder to complete sliding

δx = equal increments in which the total sliding horizontal sliding is covered

ν = Poisson's ratio

μ = coefficient of friction

σ_e = maximum equivalent von Mises stress

ω = interference between cylinder surfaces

ω^* = non-dimensional vertical interference between cylinders, ω / ω_c

Superscripts

* = dimensionless

Subscripts

′ = equivalent

1 = bottom cylinder

2 = top cylinder

Al = of Al 6061-T651 (Al)

c = critical value at onset of plastic deformation

Cu = of Glidcop (Cu)

net = net value after sliding is completed

res = residual value after sliding is completed

x = corresponding to horizontal axis

y = corresponding to vertical axis

SUMMARY

This work presents the results of Finite Element Analyses (FEA) used to simulate sliding in two (2D) and three dimensions (3D) between two interfering elasto-plastic bodies. Cylinders are used to model sliding contact in 2D, simplified by the assumption of plane strain. Sliding is studied between two cylinders modeled with material properties of steel, and separately with a Copper (Glidcop) cylinder sliding over an Aluminum (Al 6061-T651) cylinder. All materials are modeled as elastic-perfectly plastic and follow the von Mises yield criterion. Both frictionless as well as frictional sliding is investigated. The FEA provide trends for the deformations, reaction forces, stresses, and net energy losses as a function of sliding distance. All these results are found to be related to the magnitude of vertical interference. In addition, empirical equations representing the pattern followed by the residual deformation for each of these interference cases are derived. Contour plots of the von Mises stresses are also presented to show the formation and distribution of stresses with increasing plastic deformation as sliding progresses. This work shows that for the plastic loading cases of frictionless sliding, the ratio of the vertical force to the horizontal reaction force is not zero at the point where the bodies are perfectly aligned about the vertical axis. This work also presents empirical equations that relate the net energy loss due to sliding under an elasto-plastic deformation as a function of the sliding distance. In addition, a "load ratio" of the horizontal reaction force to the vertical one is defined for frictionless sliding. Although this is analogous to the common definition of the coefficient of friction between sliding surfaces, it just contains the effect of energy loss in plasticity. The contact dimensions are obtained for different vertical

interferences as sliding progresses. Comparisons are drawn between the FEA results of frictional and frictionless sliding.

Solid spheres are modeled to simulate sliding between asperities in 3D. A benchmark FE model is formulated to study behavior of asperities in loading conditions such as those explored in the 2D case. It is found that significantly larger computational resources are required to carry out a thorough study of elasto-plastic sliding between asperities in 3D. The model presented in this work is used to generate preliminary representative results.

CHAPTER 1: INTRODUCTION

Sliding contact between two elasto-plastic cylinders and spheres has important engineering applications in both the macro and the micro scale. The models presented in this work are normalized to be valid in both scales as long as continuum mechanics prevails. In micro scale, it is well known that asperities deform plastically during sliding contact between rough surfaces. Thus, it is important to know the effect the contact has on the surface material and the geometry through plastic deformations and residual stresses. In macro scale, this information may be useful in analyzing the friction, wear, and deformation of contacts such as in needle bearings, gears, rolling element bearings, wheel on rail, when sliding may occur (in addition to rolling). Sealing and thermal and electrical conductivity between contacting rough surfaces can be also be studied by using the results presented herein. The prime motivation for this study is its value in understanding the Electromagnetic Launcher (EML) technology that is presently being explored to facilitate high-speed projectile launching. Figure 1 shows a schematic of the EML set-up. High density current passed through the armature in conjunction with the magnetic field around the rails propels the projectile in the direction shown at a very high velocity (about 1-3 km/s). Sliding under pressure takes place between the surfaces of the armature and the rail, and results in the development of high stresses and temperatures at the contact interface. To understand how plasticity caused by such sliding contact affects the performance of the EML, the two surfaces have to be considered as rough, and are assumed to be made up of asperities. The interaction between asperities on the two surfaces then needs to be analyzed to understand its role on the whole system behavior

under operating conditions. The asperities in turn are assumed to be hemispherical and attached to the bulk material at the base. It is also assumed that bulk deformation has negligible effect on the development of stresses at and around the contact interface.

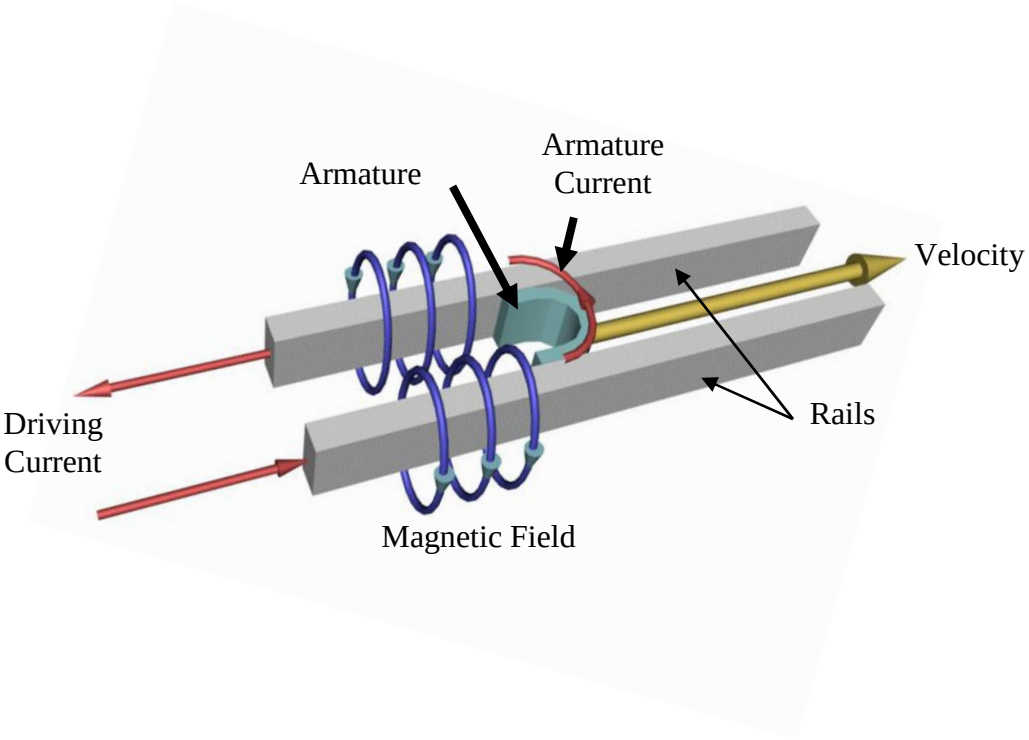

Figure 1: Schematic of the EML set-up

FEA is used to probe the mechanics of this problem as the high temperature and pressure conditions mean that the phenomena of interest, such as deformation and stress formation, occur in the elasto-plastic regime. As no closed-form solutions are available for the calculation of these parameters, numerical techniques such as FEA have to be employed. An advantage of using FEA is that actual physical visualization of the simulated process can be easily developed. In this application the interference between the armature and the rail of the EML is preset, and hence it is appropriate to use this as a driving boundary condition. Given the complexity of the problem, a 2D FE model is

formulated first and thoroughly analyzed to determine what trends may be expected for the 3D simulations. Results for sliding in 2D are presented for both the frictionless as well as frictionless cases. A plane strain condition is specified for the 2D models, meaning the contact can be visualized as occurring between two cylinders of infinite length. The frictionless sliding simulations help in isolating the purely mechanical process of sliding, omitting the role played by friction (or other effects, such as adhesion). The thermal effects of sliding lead to eventual transition from metal-metal contact to arcs/plasmas at the rail-armature interface as discussed in [1]. These effects are not included in this study. Thus, the role that plastic deformation plays in elasto-plastic sliding contact is exposed. On the other hand, frictional sliding directly correlates to the conditions in the EML, and gives an overall idea of what in fact happens when the armature slides over the rails of the EML. A steel material that is widely used in common Engineering applications is chosen as a base case for the aforementioned study, along with a specific investigation involving sliding between materials Glidcop (Cu) and Al 6061-T651 (Al) that are used to respectively form the rail and armature in the EML. Once the trends are established for the 2D models, an attempt is made to simulate sliding in 3D using thus established FE techniques. While the EML is a specific application for which this study is specifically directed, it is envisioned that the results may generally be applied to other Engineering applications. Chapter 3 discusses frictionless sliding in 2D with the assumption of plane strain, i.e., between two cylinders of infinite length. In Chapter 4, FEA of sliding in 2D with friction is discussed and the results are contrasted with those from Chapter 3. The 3D methodology developed after the establishment of the FE technique is then presented in Chapter 5.

CHAPTER 2: LITERATURE REVIEW

Sliding contact between two elasto-plastic cylinders and spheres has important engineering applications in both the macro and the micro scale. The current models are normalized to be valid in both scales as long as continuum mechanics prevails. In micro scale, it is well known that asperities deform plastically during sliding contact between rough surfaces. Thus, it is important to know the effect the contact has on the surface material and the geometry through plastic deformations and residual stresses. In macro scale, this information may be useful in analyzing the friction, wear, and deformation of contacts such as in needle bearings, gears, rolling element bearings, wheel on rail, when sliding may occur (in addition to rolling). The results presented here may also be valuable in analyzing human joints, such as that investigated by Chen et al [2], wherein 2D plane strain finite elements are employed to model the temporomandibular joint using hyperelastic (Mooney-Rivlin) material. The approach is similar to the one taken in the current study only that here metallic-like material behavior is prevailing.

Both elastic and elastic-plastic spherical contacts have been analyzed in great detail in the last four decades. A wide array of works have analyzed the contact of rough surfaces as reviewed by Liu et al. [3]. Most of these works are based on the contact behavior of a single asperity in a statistical model of multiple asperity contact. All these works, share the common methodology of Thomas [4] and Greenwood [5] that is as follows:

1) Replacing the two rough surfaces by a smooth surface in contact with an equivalent rough surface

2) Replacing asperities with simple geometrical shapes

3) Assume a probability distribution for asperity parameters.

Some of these works are restricted mainly to pure elastic regime, such as the ground-breaking paper by Greenwood and Williamson [6]. Other works, such as Greenwood and Tripp [7], Lo [8], Whitehouse and Archard [9], Tsukizoe and Hisakado [10], and Bush et al [11] and [12], extend the Greenwood and Williamson model in the elastic regime to a variety of geometries and different basic assumptions. Other works concentrate on pure plastic deformation, and are based on the models of Abbott and Firestone [13] and Tsukizoe and Hisakado [10].

Normal spherical contacts in the elastic-plastic regime have been investigated by Chang et al [14], and is widely known as the CEB model. Due to an assumption on the contact pressure distribution for the plastically deformed sphere the CEB model suffers from a discontinuity in the contact load at the transition from the elastic to the elastic-plastic regime. Assumptions on the contact pressure distribution and other mathematical considerations were used by Evseev et al. [15], Chang [16], and Zhao et al. [17] to overcome the deficiencies of the CEB model. FEA has been used by Vu-Quoc et al. [18] to analyze contact between two spheres, which by symmetry is equivalent to that of one sphere in contact with a frictionless rigid plane, but the analysis is restricted to specific parameters and lack generality. Recently, Kogut and Etsion [19], Jackson and Green [20] and Wang and Keer [21] have explored elastic-plastic contact in 3D. However, the characteristics of normal contact as opposed to sliding contact are quite different, and thus the latter is explored in this work. Hamilton and Goodman [22] presented implicit equations and graphs of yield parameter and tensile stress distribution for circular sliding

contact using the von Mises criterion for the prediction of yielding. Hamilton [23] further developed the implicit results in [22] to obtain explicit formulae for the stresses beneath a sliding, normally loaded Hertzian contact. However, these studies [22, 23] concentrated on the effect of increasing friction in a sliding contact against a rigid flat, and on the resulting development of impending failure regions, but a coefficient of friction had a priori been imposed. In contrast, this works isolates the effects of purely frictionless sliding of interfering cylinders, and hence the development of stresses, energy loss, and other phenomena occur solely due to mechanical deformation. Also, sliding between two spheres has been analyzed by Kogut and Etsion [24] and Faulkner and Arnell [25]. The first is based on some postulations and analytical heuristics (again modeling hemisphere traction against a rigid flat), while the latter marks perhaps one of the earliest attempts in tackling interference sliding, but quotes extremely long execution times even for very coarse FEA meshes (~960 hours for each simulation), and leaves out generalization of results. Steady-state dry frictional sliding between two elastic bodies by using Fourier series and integral transform techniques has been examined by Nosonovsky and Adams [26].

It is clear from the literature survey that a thorough investigation of the actual forces, deformations, stress formations, and most importantly energy losses due to plasticity for sliding in the elastic-plastic regime is missing. The equivalent model of "elliptical contact against a rigid flat" is the consequence of the elastic Hertzian theory. Even though it had been used in normal elasto-plastic contact, such an "equivalent model" has no physical grounds or mathematical proof once plasticity takes place, certainly not when the two sliding bodies have distinct material properties. These

parameters are critical in understanding the sliding phenomenon under high pressure and temperature as in the EML, and play a pivotal role in the design and construction of such systems. This work helps in understanding the aforementioned factors, and now the thermal and electromagnetic aspects of the problem can be amalgamated with these findings to form a comprehensive understanding of such sliding. In this work, elastic-perfectly plastic cylinders in 2D and hemispheres in 3D sliding over each other are treated as whole bodies, and not as a part of a statistically generated surface. By means of FEA actual sliding in simulated, wherein the two interfering bodies are both fully modeled, without resorting to the common model of an equivalent body against a flat.

CHAPTER 3: FRICTIONLESS 2D ANALYSIS

3.1 Steel on Steel Sliding

3.1.1 Approach and Assumptions

Two semi-circles representing the sliding cylinders are modeled and one is made to traverse over the other with a preset vertical interference ω between the two (see Figure 2). Sliding is first simulated as a frictionless process, i.e., no coefficient of friction is input in the FE model. Also, repeated sliding is not considered, and hence the top cylinder is made to pass over the bottom cylinder just once. This is defined as 'one-pass' sliding. Following are the assumptions that are used to simplify the problem discussed in this section:

1) The two cylinders are considered to be infinitely long in the direction perpendicular to sliding. This enables the FE model to be in 2D under the assumption of plane strain behavior.
2) The sliding bodies are idealized to have elastic-perfectly plastic behavior. This is a first order approximation to describe stress-strain behavior.
3) Sliding is assumed to be a frictionless process, and hence no coefficient of friction is input in the FE model. This is done in order to isolate the effect of plasticity during sliding that causes elastic-plastic deformation.
4) It is assumed that the mesh that is validated up to the onset of plasticity is also robust for analysis of the elastic-plastic regime, since no closed form solutions are available for this purpose.

5) Deformations in the bulk area are assumed not to have a significant bearing on the effects of sliding in the contact region.
6) Sliding is simulated as a quasi-static process, i.e., time-dependent phenomena are not analyzed. Hence, dynamic effects are ignored and material properties used do not depend on the strain rate.
7) Temperature effects that occur due to sliding are not considered, and the material properties used are assumed to be at room temperature.

In the elastic domain and up to the onset of plasticity, the Hertzian solution [27] provides at the onset of plasticity critical values of load, contact half-width, and strain energy [28]. As explained by Jackson et al [20, 29], hardness is not implemented as a unique material property as it varies with the deformation itself as well as with other material properties such as yield strength, Poisson's ratio, and the elastic modulus. Instead, the critical vertical interference, ω_c, as derived by Green [28] for cylindrical contact, is employed. This quantity is derived by using the distortion energy yield criterion at the site of maximum von Mises stress by comparing the stress value with the yield strength, S_y. The critical values of force per unit length, half contact width, and interference are respectively given in [28]:

$$\frac{P_c}{L}=\frac{\pi R\left(CS_y\right)^2}{E'}\ ;\ b_c=\frac{2R(CS_y)}{E'}\ ;\ \omega_c=R\left(\frac{CS_y}{E}\right)^2\left[2\ln\left(\frac{2E'}{CS_y}\right)-1\right] \tag{1}$$

$$C=\frac{1}{\sqrt{1+4(\nu-1)\nu}} \qquad \nu\le 0.1938$$

$$C=1.164+2.975\,\nu\text{-}2.906\,\nu^2 \qquad \nu>0.1938 \tag{2}$$

The value of *C* is obtained from elasticity considerations, and the critical parameters are obtained at the point of yielding onset, where R and E' are the equivalent radius and equivalent modulus of elasticity, respectively. The maximum elastic energy that can possibly be stored (up to the point of yielding onset) is used to normalize the net energy loss due to plastic deformation after sliding, and is given by Green [28] as:

$$\frac{U_c}{L} = \frac{\pi \left(CS_y\right)^4 R^2}{4E'^3} \left\{ 4\ln\left[\frac{2E'}{CS_y}\right] - 3 \right\} \tag{3}$$

For this section, the critical values are calculated for a steel material with properties as follows: $\mathrm{E}_1 = \mathrm{E}_2 = 200\,\mathrm{GPa}$, $\nu_1 = \nu_2 = 0.32$, and $S_y = 0.9115\,\mathrm{GPa}$. This material has been tested by Jackson et al. [20], and its yield strength lies in the middle of the range of the five steel materials investigated in that work. The results obtained in this work are thus not representative of all steel materials, but only of that tested by Jackson et al. [20]. Since all the quantities are subsequently being normalized by the aforementioned Equations (1), (2), and (3), the ensuing results apply for any geometry scale (as long as homogeneous and isotropic continuum mechanics prevails); therefore, the radii for the cylinders in the FE model are subjectively (and conveniently) chosen to be $R_1 = R_2 = 1m$. The calculated values of the above parameters are shown in Table 1, and are likewise used to establish convergence of the finite element model.

Table 1: Critical values of parameters at the onset of plasticity for sliding between two steel cylinders

Parameter	Value
C	1.818
CS_y	1.657 GPa
ω_c	0.974 mm
P_c/L	0.0387 GN/m
b_c/L	0.014874
U_c/L	0.2594 kN

The approach used in this work to simulate sliding contact involves the application of displacement boundary conditions to facilitate interference sliding. This approach also results in a rapid convergence of the solution as compared to the boundary condition where forces are applied instead of displacements. The material of the cylinders is assumed elastic-perfectly plastic with identical behavior in tension and compression. Throughout this discussion, the Y-axis corresponds to the vertical direction, and the X-axis to the horizontal (see Figure 2).

3.1.2 Geometry, Meshing, and Boundary Conditions

As shown in Figure 2, the nodes at the base of the bottom cylinder are constrained from displacement in the X and Y directions. The nodes at the base of the top cylinder are also constrained from displacement in the Y direction, but are allowed to displace freely in the X direction upon sliding. A reasonably large range of vertical interferences, coupled with horizontal sliding distance, Δx (from one side where the cylinders are just in contact to the other side where they just come out of contact), is used to simulate the sliding process (See Figure 3).

The horizontal sliding distance, Δx, is calculated from geometry and is a function of the interference, ω, where clearly Δx increases with the preset interference ω. That total distance is divided into n equal load steps, $\delta x = \Delta x / n$. Hence, at load step i the location of the center of the traversing cylinder relative to the center of the stationary cylinder is:

$$x = i \cdot \delta x - \frac{\Delta x}{2}; \quad i = 0, n \tag{4}$$

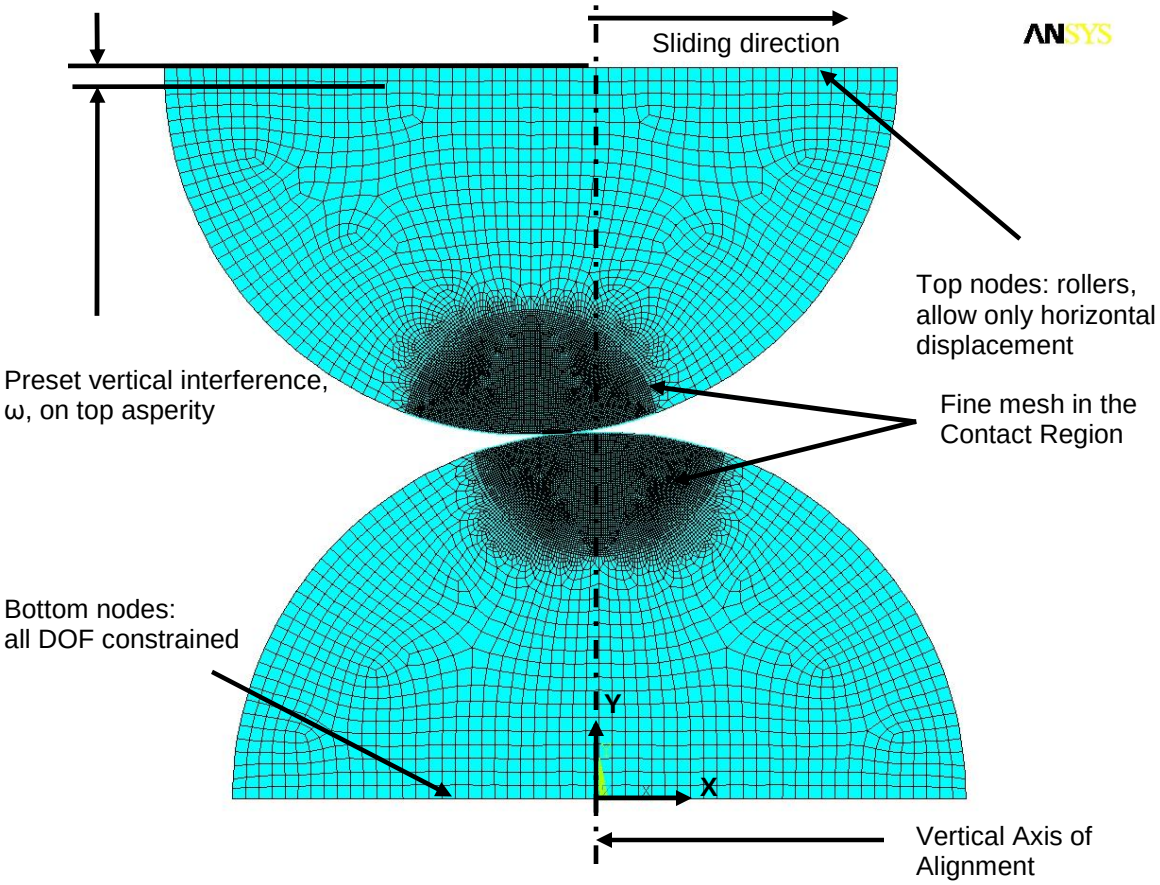

Figure 2: Schematic of the FEA for sliding between cylinders

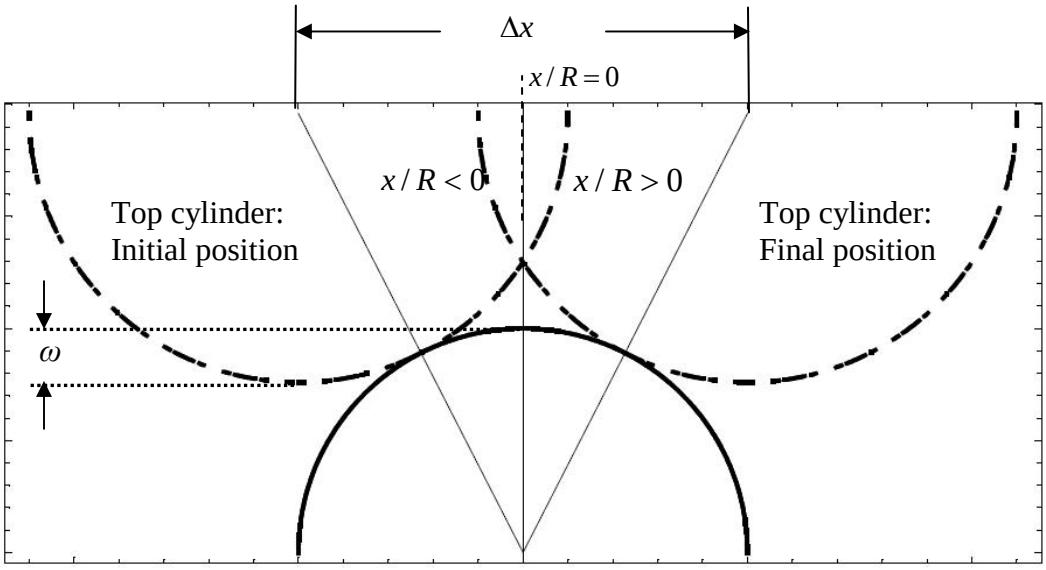

Figure 3: Schematic of the sliding process

The following regimes correspond to these vertical loading ranges as defined by Jackson et al [29], namely: (1) the elastic regime considers deformation absent of plasticity, (2) the elastoplastic regime contains plastically deformed material but the contact area still contains an elastic region, and (3) the fully plastic regime defines the case of a contact whose area of contact yields entirely. Loading is defined by the phase where the top cylinder is pressed horizontally against the bottom one before passing the vertical axis of alignment. Unloading occurs when the top cylinder has passed the vertical axis of alignment, and hence the cylinders are repelling each other.

To establish confidence in the mesh for different loading schemes (ranging from elastic to highly plastic), a 2D plane strain FEA simulation of the cylindrical line contact is performed. The modeling and meshing for this simulation is similar in approach to that employed by Jackson and Green [20]. However, instead of a quarter-circle and a rigid flat as in [20], contact in this case is between two elasto-plastic semi-circles representing the two cylinders. In addition, a new meshing scheme is introduced wherein a semicircular dense region of elements is used to capture the high stresses in the small region of contact (see Figure 2 and Figure 3). This mesh is symmetric about the vertical axes of the cylinders. Jackson and Green [20] employed a rectangular region for the same purpose.

The commercial FEA software ANSYS® is used to perform the analyses. The mesh is constructed using quadratic eight node quadrilateral elements (Plane 82 in ANSYS) and surface-to-surface contact elements (Contact 172 and Target 169 in ANSYS). A symmetric contact pair wherein either surface has a layer of contact as well as target elements is defined. This ensures robustness of the contact model. Also, contact detection is set to be on nodes normal to the target surface and not at Gauss points to

ensure symmetrical results. Once the predetermined regions are established, ANSYS is used to automatically mesh the said regions. Various mesh schemes are tried to achieve convergence. The optimized model has 83372 nodes, 25570 elements, and 200 contact elements in the region of interest (see zoomed contact region in Figure 4).

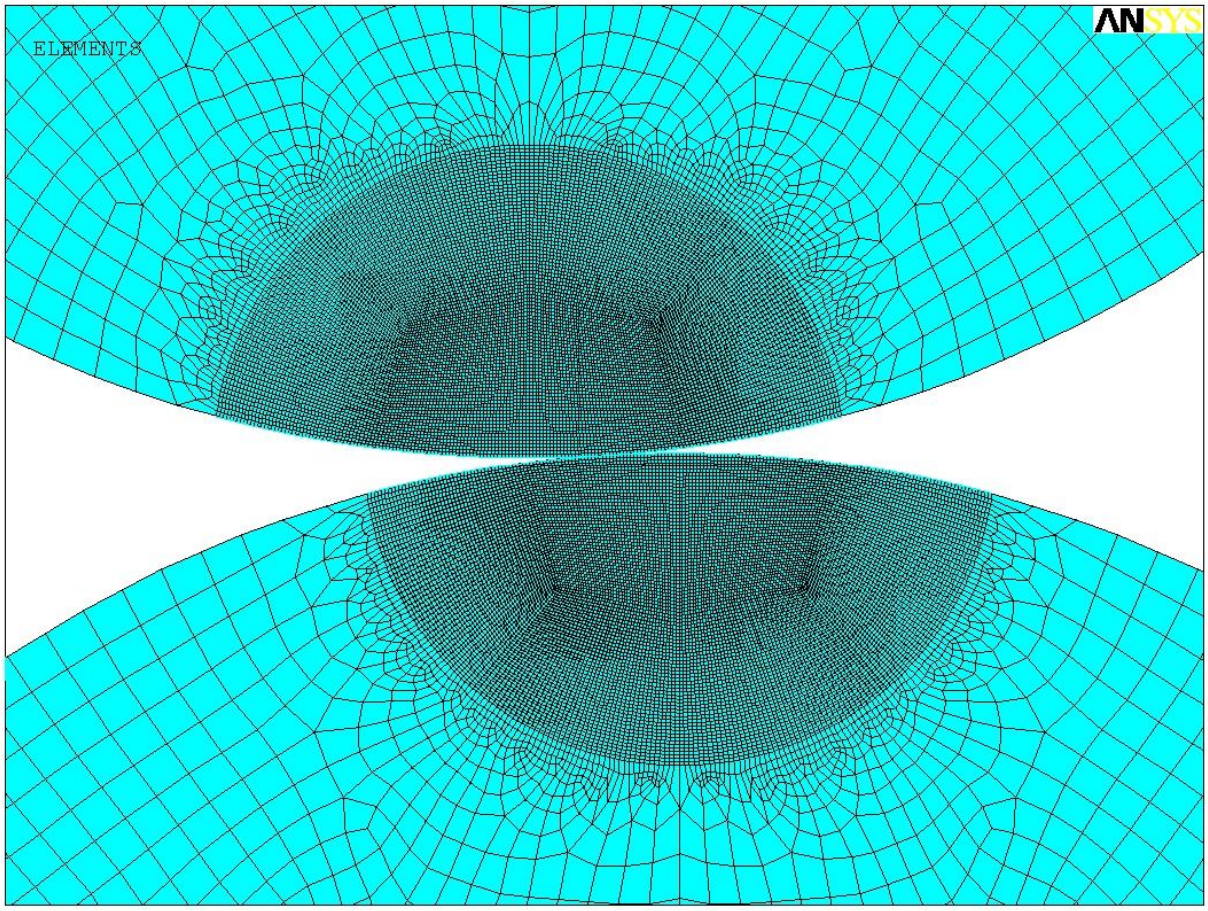

Figure 4: Description of the meshing scheme employed

3.1.3 Validation

The mesh is validated first under non-sliding normal elastic contact, against the analytical solution obtained by Green [28], as summarized in the appendix. In the FEA model the values of interference are imposed and the contact half-width, the maximum von Mises stresses, and the maximum pressure are extracted. Corresponding to the imposed interferences, ω, the values of the load P/L and the contact half-width are obtained from Eq. (1). The maximum contact pressure and the maximum von Mises stresses values are calculated from the equations given in the theoretical background in the appendix (Equations 15 and 20 in [28]) . The results of this validation are shown in Table 2, where the last row represents the critical values at $\omega = \omega_c$ (or $\omega^* = 1$). The maximum disagreement between the FEA values and the theoretical values occurs at the lowest applied vertical interference of $\omega^* = 0.2$. The accord between the FEA and the theoretical values gets progressively better as higher vertical interferences approaching criticality are applied. Extremely good agreement is found between the parameters calculated at critical interference for sliding contact between two cylinders and those for non-sliding normal contact. The contact half width, b_c, differs by only 3.4%, where the maximum equivalent von Mises stress, σ_e, and the maximum contact pressure, p_o, differ by less than 1%. The larger error in the contact half-width is attributed to the finite FEA grid, i.e., the resolution or spacing between the contact elements. The smaller the interference the smaller number of contact elements are in effect, leading to a larger error, and vice versa. In this analysis, sliding takes place under interference values sufficiently larger than the critical interference, and thus additional mesh convergence tests are undertaken.

Table 2: Validation of the meshing scheme employed

ω^*	*ANSYS b (m)*	*Theoretical b (m)*	*%diff*	*ANSYS* σ_e *(GPa)*	*Theoretical* σ_e *(GPa)*	*%diff*	*ANSYS* p_o *(GPa)*	*Theoretical* p_o *(GPa)*	*%diff*
0.2	0.00663	0.00579	-14.3	0.338	0.355	4.8	0.615	0.646	4.7
0.3	0.00784	0.00726	-8.0	0.433	0.445	2.7	0.786	0.809	2.9
0.5	0.01010	0.00964	-4.8	0.585	0.591	1.0	1.058	1.074	1.5
0.7	0.01202	0.01162	-3.4	0.709	0.712	0.5	1.279	1.294	1.2
1.0	0.01445	0.01397	-3.4	0.858	0.856	-0.2	1.545	1.556	0.7

As no closed-form solutions are available for the elastic-plastic domain with which the FE model can be validated, additional combinations of reasonable boundary conditions and meshing schemes are checked to attest the results obtained by the method described above. These are all done at an interference value of $\omega^* = 9$. They are as follows:

- To verify the meshing scheme employed, both the top and bottom cylinders are meshed such that the nodes and elements generated mirror each other across their respective axes of symmetry. This is different from the automated meshing technique wherein the mesh is not necessarily mirrored, and hence may not be exactly symmetric. However, the result parameters obtained via both approaches are found to be approximately within 2% of each other.
- To verify the boundary conditions used, the cylinders are laterally translated towards each other (instead of completely affixing the bottom cylinder and sliding the top one across it). Again, this method yields results that differ from the one described earlier by only about 2%.
- Instead of an 8-node quad element, a 6-node triangular element in a perfectly symmetric meshing is used in the case where the two cylinders are slid against

each other. Again, this resulted in no change in the intermediate load steps and the final results with a finer triangular mesh are within 2% of those obtained earlier.

- Likewise, affixing the upper cylinder and sliding the bottom cylinder, with either meshing scheme, also yields results that are approximately within 2% of those found from the employed boundary condition. That is, the upper cylinder and lower cylinder maintained their own stress and deformation patterns.

The symmetric mesh such as the one shown in Figure 4 is employed for the entire study. Since the problem is non-linear, small load steps are used toward incremental (quasi-static) sliding from one end to the other. Values of the contact force, stress tensor, von Mises stress, and displacement are recorded at each load step. The contact forces are determined by summing the reaction forces at the base of the bottom cylinder.

It is noteworthy that the computational cost is considerably smaller when using the boundary conditions where displacement is applied to only one of the cylinders. The model as described above is upheld and used for the entire study since for such contact in the elastic regime, the results obtained through the employed boundary conditions and meshing scheme match the theoretical values closely. It is thus postulated that the FEA mesh used is trustworthy in the elastic-plastic regime. The upper value of the range of vertical interferences is chosen arbitrarily. However, it is sufficiently high to cause significant plasticity in sliding for the tested materials. Results for higher values may be extrapolated within reason, however, there could certainly be cases where this upper bound is insufficient. Extremely high vertical interferences cause excessive element distortion, which result in higher, almost prohibitive computational times. Also, the

results that are discussed show similar trends, and hence are deemed to sufficiently represent sliding in the elastic-plastic regime.

3.1.4 Results and Discussion

The results are presented for a range of preset normalized vertical interferences, ω^*, from *1* (elastic limit) to *20* (elastic-plastic). The material properties used for the cylinders are chosen to be steel, which is commonly employed in many engineering applications. The computation time is about an hour for sliding with small vertical interferences to about *4* hours for sliding with larger interferences on a dual processor Xeon *3* GHz PC with hyperthreading turned on to utilize four virtual processors.

3.1.4.1 Deformations

Since both cylinders are modeled with the same material properties, the deformation pattern followed by the two is identical. The displacements of the nodes on the cylinder surfaces are monitored in order to understand the deformation of the cylinders. The maximum vertical displacement, $u_{y,}$ is defined as the maximum displacement in the Y direction among the nodes on the contact surfaces of the two cylinders. u_y is effectively normalized by the critical interference ω_c given in Table 1. Sliding is attained piecewise as the top cylinder traverses a total displacement, Δx (see Figure 3). For the presentation of the results, x is being normalized by the equivalent radius of the cylinders, R, such that $x/R < 0$ signifies loading, and $x/R > 0$ signifies unloading. The cylinders are perfectly aligned at $x/R = 0$. Plots of the normalized maximum vertical displacement, u_y/ω_c, with respect to the normalized sliding distance of the top cylinder, x/R, are presented for the aforementioned range of ω^* in Figure 5.

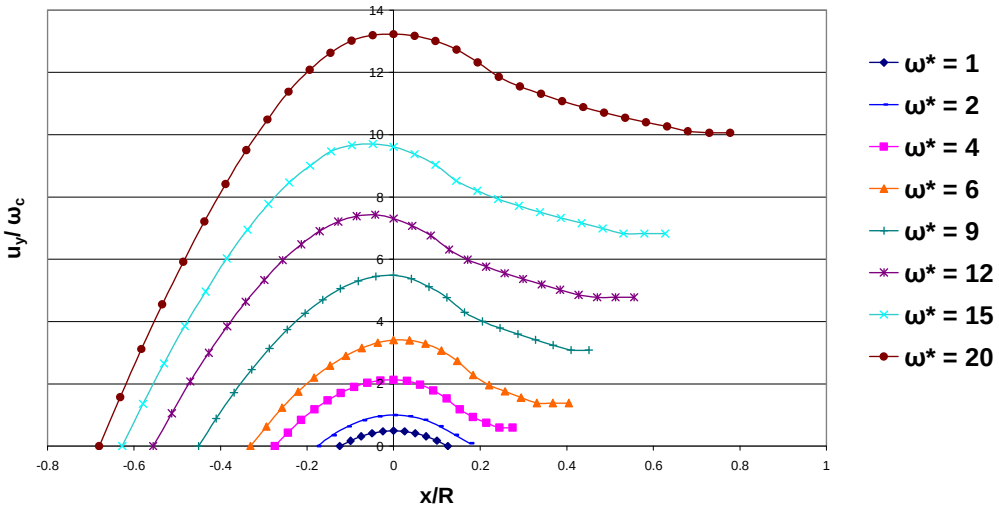

Figure 5: Normalized maximum vertical displacement vs. normalized sliding distance

As expected, for $\omega^* = 1$, the vertical displacements are symmetric about the axis of alignment. Also, displacements increase with the increase in vertical interference ω^*, i.e., with increase in load. For normal loading, the total maximum vertical displacement is always at the center of contact in both cylinders and is equal to the applied vertical interference. However, in sliding contact the location of the points where maximum deformation occurs is found to be at two different locations along the sliding direction, i.e., these points are not vertically aligned as in the normal loading case. This explains the magnitudes of the vertical deformations being higher than the applied interference. It can be seen that for $\omega^* > 1$, there is plastic deformation where the curves do not come back down to the zero displacement line, i.e., to the X axis. Instead, it flattens out and preserves the plastic deformation that has occurred as can be seen from the last few data points on each curve. This normalized vertical residual deformation, u_{res}/ω_c, increases with the increase in vertical interference between the cylinders as shown in Figure 6.

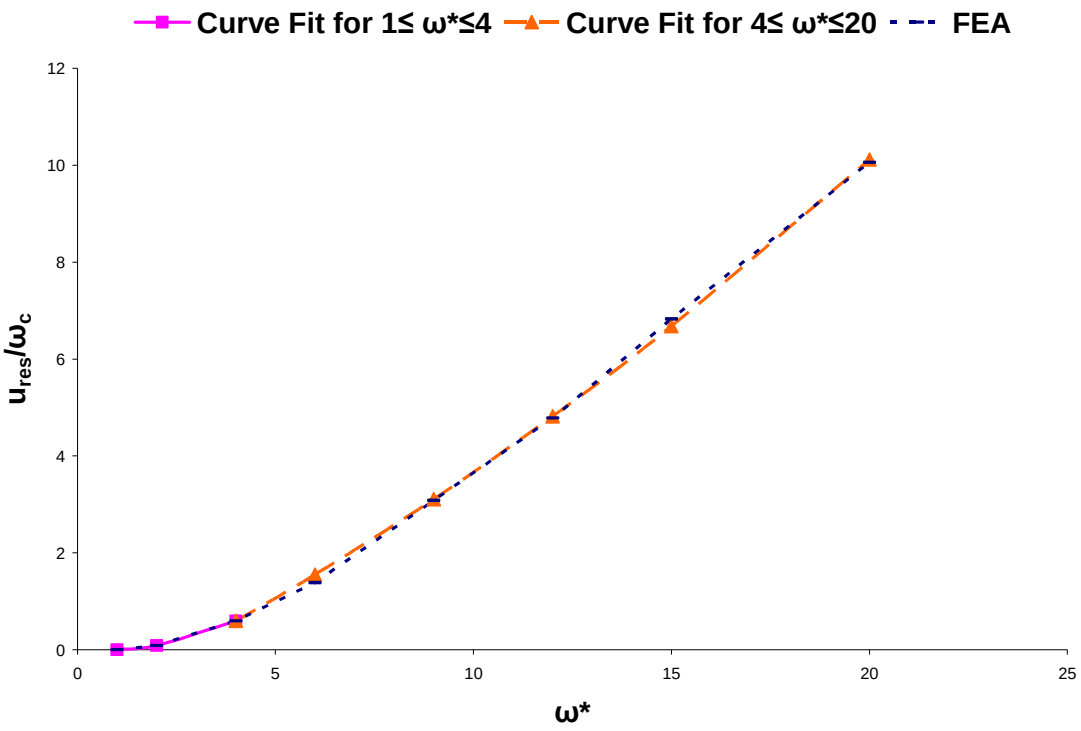

Figure 6: Development of residual deformation with increase in vertical interference

To capture the residual deformations the last points in Figure 6 are extracted for different ranges of the applied vertical interference, and equations are fitted to the numerical data, all shown in Figure 6:

$$\frac{u_{res}}{\omega_c} = 0 \qquad \omega^* \le 1$$

$$\frac{u_{res}}{\omega_c} = 0.03045(\omega^* - 1) + 0.05556(\omega^* - 1)^2 \qquad 1 \le \omega^* \le 4 \qquad (5)$$

$$\frac{u_{res}}{\omega_c} = 0.59139 + 0.47795(\omega^* - 4) + 0.01391(\omega^* - 4)^2 \qquad 4 \le \omega^* \le 20$$

3.1.4.2 Forces

Reaction forces at the base nodes of the bottom cylinder are summed for each load step and plotted against the normalized horizontal sliding distance x/R. Both the normal reaction force, F_x, and the tangential reaction force, F_y, are normalized by the critical load, P_c given in Table 1. Figure 7 and Figure 8 show the trends followed by F_x/P_c and F_y/P_c, respectively, as the top cylinder slides across the bottom one.

As expected, it is apparent that for the vertical interference $\omega^* = 1$, the curve is anti-symmetric in Figure 7, and symmetric in Figure 8, signifying no loss of energy once sliding is completed. However, for the elastic-plastic loading cases, where $\omega^* > 1$, permanent plastic deformation occurs and some energy is lost in the process. This is evident from Figure 7 as the area under (energy invested in sliding) is larger than that above (energy restored in rebound) for all the curves in the elastic-plastic regime. This shows that more work is done by the driver in pushing the top cylinder across the bottom one in the loading phase ($x<0$), than done on the driver during the unloading phase ($x>0$) where the cylinders are repelling each other.

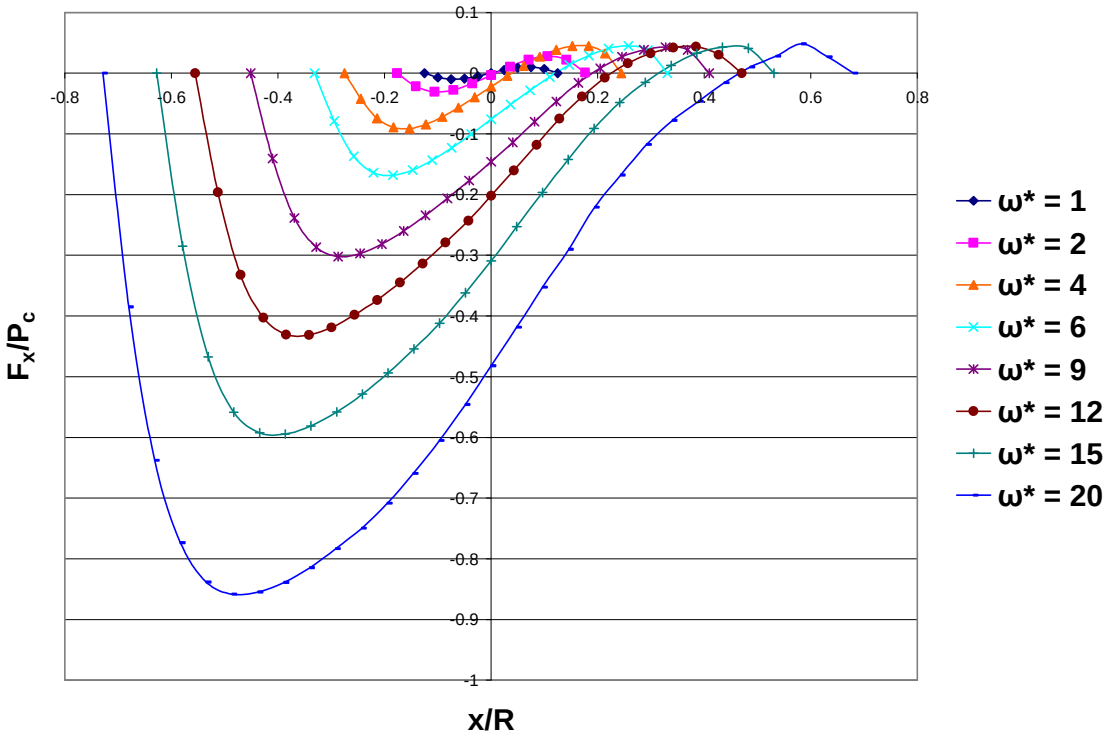

Figure 7: Normalized horizontal reaction force vs. normalized sliding distance

From Figure 8 it is also apparent that the normalized vertical reaction force, F_y, is symmetric for $\omega^* = 1$, but becomes higher and increasingly skewed towards the loading side as the applied vertical interference is increased. This is because the cylinders are coming out of contact and hence do not induce as much reaction force.

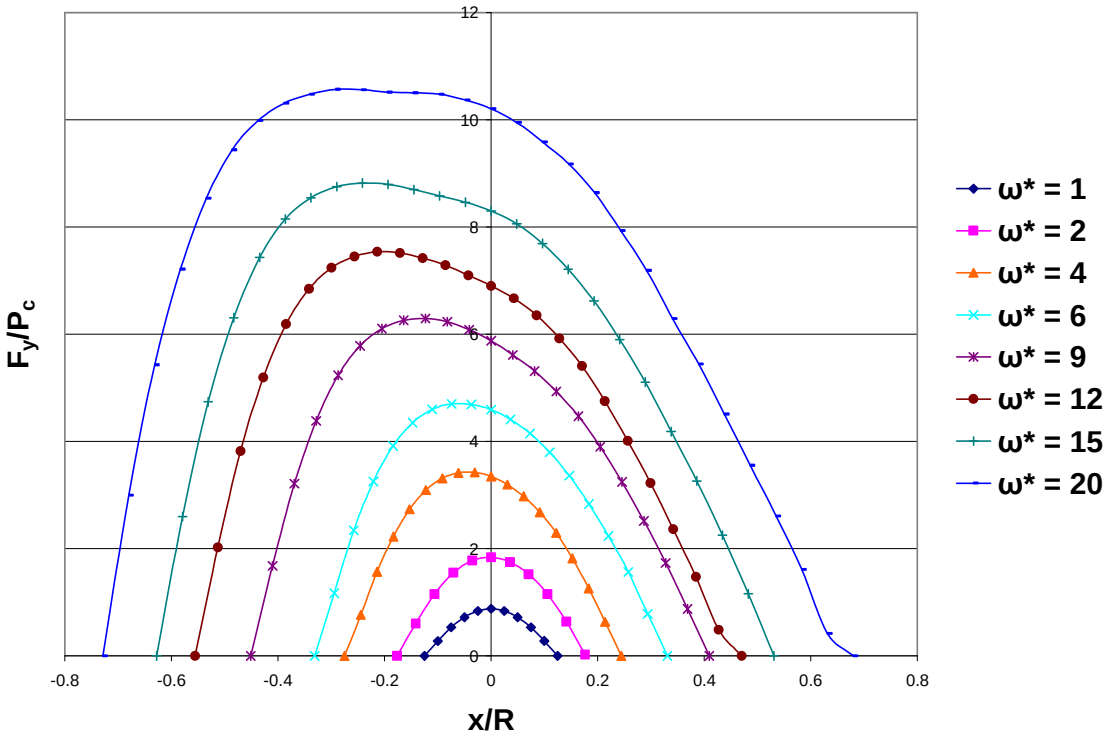

Figure 8: Normalized vertical reaction force vs. normalized sliding distance

Now, a "load ratio" is defined as F_x/F_y, being the ratio of the horizontal reaction force and the vertical reaction force. This ratio is generated and plotted versus the normalized sliding distance as shown in Figure 9. While each of the data points on these curves can be thought of as a quantity similar to the instantaneous local coefficient of friction, it is emphasized that this is not a "coefficient of friction" in the standard sense since other effects (e.g., adhesion, contamination) are not accounted for. This load ratio applies only to this isolated mechanical sliding process. Moreover, in the region where the cylinders are moving away from each other, the positive "load ratio" does not truly indicate a "negative coefficient of friction."

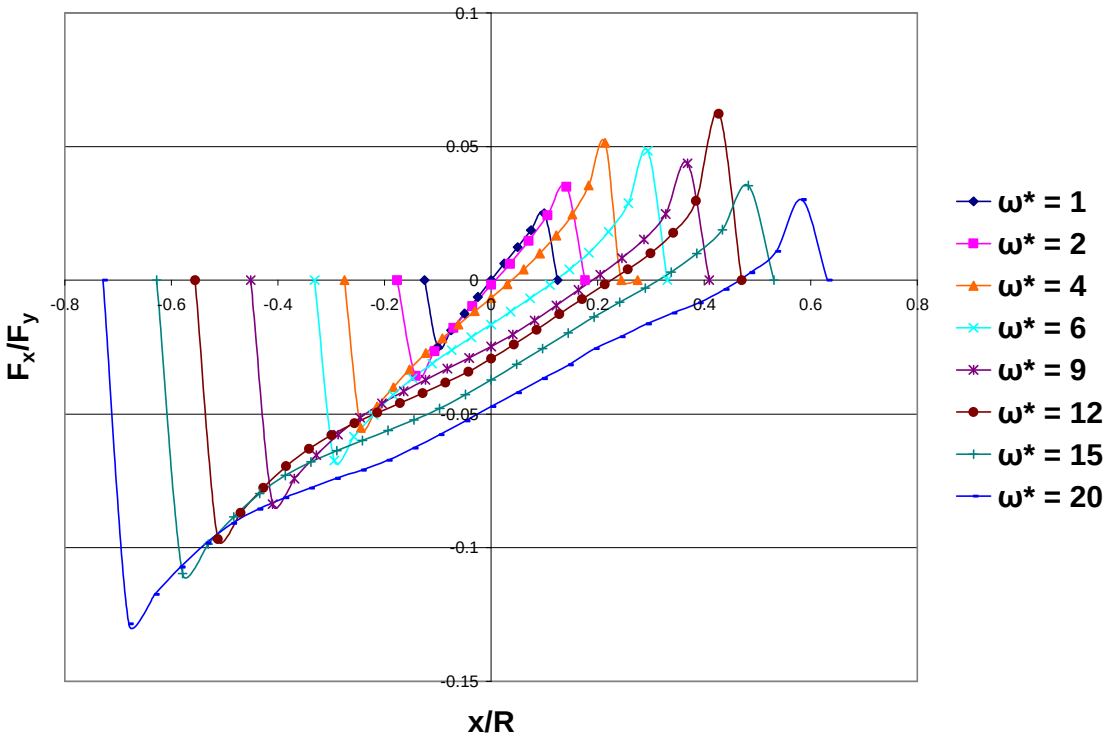

Figure 9: "Load Ratio" vs. normalized sliding distance

For the elastic loading case of $\omega^* = 1$, the curve in Figure 9 is anti-symmetric. For the elastic-plastic loading cases with ω^* ranging from *2* to *20*, it can be seen that the maximum magnitude of the "load ratio" increases steadily as ω^* increases. However, once the top cylinder has passed the vertical alignment axis, the maximum "load ratio" magnitude increases up to $\omega^* = 4$, and then steadily decreases as ω^* approaches 20. This is evident from the plot in Figure 9 . In addition, the plot clearly shows that for all vertical interferences, the magnitude of the "load ratio" during elasto-plastic loading is always greater than that during unloading.

It is also clear from the plot that for the plastic loading cases, the ratio of the horizontal to the vertical reaction force is not zero at the point where the cylinders are

perfectly aligned about the vertical axis. It is noteworthy that sliding as simulated by Kogut and Etsion [24] is preceded by normal loading of the spheres, and hence is not similar to the complete sliding between cylinders from one end to the other that is presented in this paper. However, it is interesting to contrast the findings of these two studies. According to the postulation by Kogut and Etsion [24], spherical contact under a normal load P is capable of supporting additional tangential load only as long as $\omega^* < 6$. For such a contact, as soon as the plastic region reaches the sphere surface, the elastic core is incapable of supporting any additional tangential load. It is clear from Figure 7, Figure 8, and Figure 9 that for sliding between cylinders, indeed additional tangential load can be supported for $\omega^* > 6$, even if the contact interface has become plastic, where in fact the tangential load increases with the interference (as evident from Figure 7).

3.1.4.3 Stress Formations

The stress regions formed in both cylinders are by and large anti-symmetric about the axis of alignment throughout the course of the sliding process, since identical material properties and geometries are used to model both cylinders. This holds for the elastic, as well as all of the elastic-plastic ranges. At low interferences, the high stress region develops below the contact interface. As sliding progresses and load on the cylinders increases for the elastic-plastic loading ranges, yielding occurs and a sub-surface plastic core develops (see Figure 10). Elastic material surrounds this plastic core, and provides the greater part of resistance to sliding. As the load increases with the progression of sliding (i.e., rendering an increase in the effective interference), the elastic region diminishes, making way for the growth and propagation of a plastic core, which

diminishes the resistance to sliding. Plasticity is observed to reach the contact interface at approximately $\omega^* = 6$. Since the next highest vertical interference tested is $\omega^* = 9$, it can be roughly assessed that yielding at the contact interface occurs for sliding with $\omega^* = 6$.

At the vertical axis of alignment, as seen from Figure 10, the von Mises stress distribution in both cylinders is identical (in an anti-symmetric pattern), with regions of slightly higher concentrations in the direction of sliding signifying resistance to sliding. For lower elastic-plastic vertical interferences, such as $\omega^* = 4$, high stresses remain near the area of contact, i.e., there is no significant stress formation at the base of the cylinders (where they may be connected to a bulk material). As the vertical interference increases, however, stresses can be seen developing in the body of the cylinder as well as at the base (see Figure 10). This signifies shear tugging at the cylinder base, and for vertical interference causing extreme plastic deformations, this might very well be the region with the highest stresses. This work concentrates on the elastic-plastic regime at the vicinity of contact, and hence only those results are presented here.

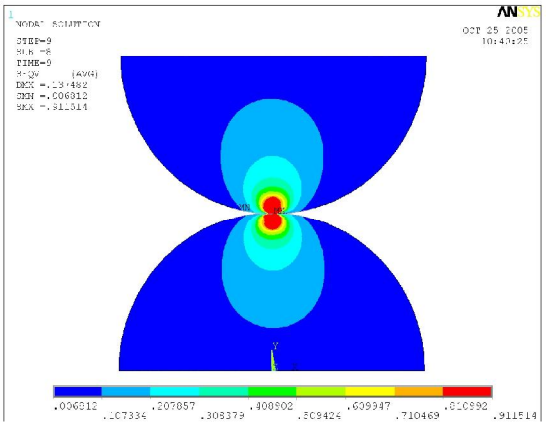

(i) ω* = 4

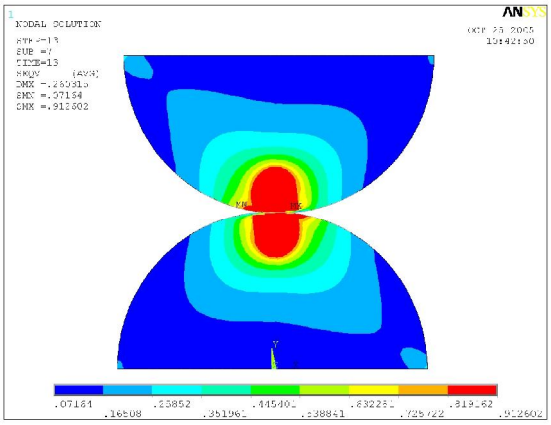

(ii) ω* = 12

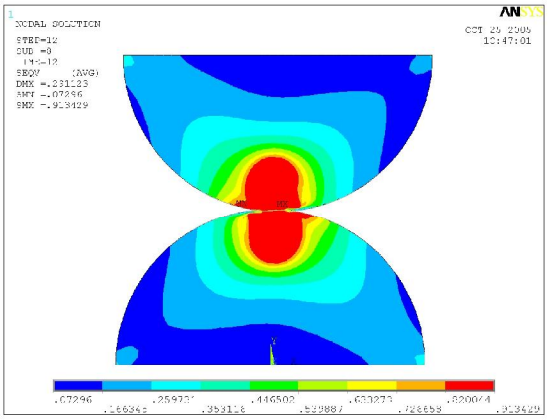

(iii) ω* = 15

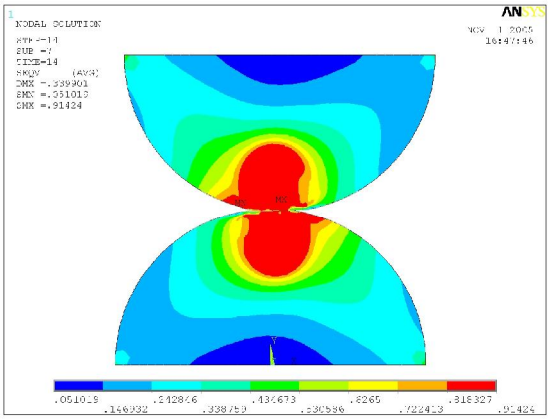

(iv) ω* = 20

Figure 10: von Mises stress contours for sliding cylindrical contact at vertical interferences of (i) ω* = 4, (ii) ω* = 12, (iii) ω* = 15, and (iv) ω* = 20 at the vertical axis of alignment

Figure 11 shows the distribution of the residual stresses after sliding is completed for the highest tested vertical interference values of $\omega^* = 15$, and $\omega^* = 20$. As expected, the residual stresses for the case with $\omega^* = 20$ are more widely spread than those for $\omega^* = 15$. The residual stress distribution of one cylinder is mirrored in that of the other. Some of these stresses remain at the yield value (i.e., residual plastic strain). Also, it can be seen that there are remnants of the stress in the bulk of the cylinders away from the area of contact as well as at their bases. As discussed earlier, for highly plastic vertical interferences, this occurrence would become significant as the mode of failure might be the initiation of cracks or the shearing-off of the cylinders.

In the absence of displacement in the vertical direction in the overall sliding process, the net energy loss in sliding can be defined as

$$U_{net} = \int_{x_1}^{x_2} F_x dx \tag{6}$$

where x_1 and x_2 respectively represent the starting and ending sliding positions of the top cylinder. This represents the net work done when sliding the top cylinder over the bottom. Thus, energy loss in sliding for individual preset vertical interference cases is essentially the area under the true horizontal reaction curve plotted against the true sliding distance. Figure 7, as discussed earlier, shows the normalized curves. The value thus obtained from the area under the horizontal reaction curve is called the net energy, U_{net}, and is normalized by U_c from Table 1.

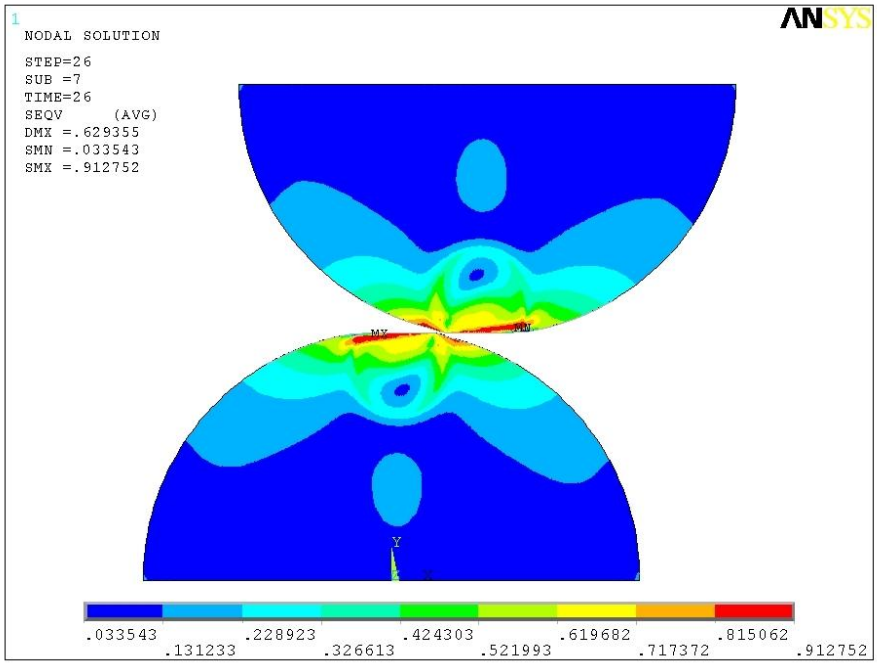

(a) ω* = 15

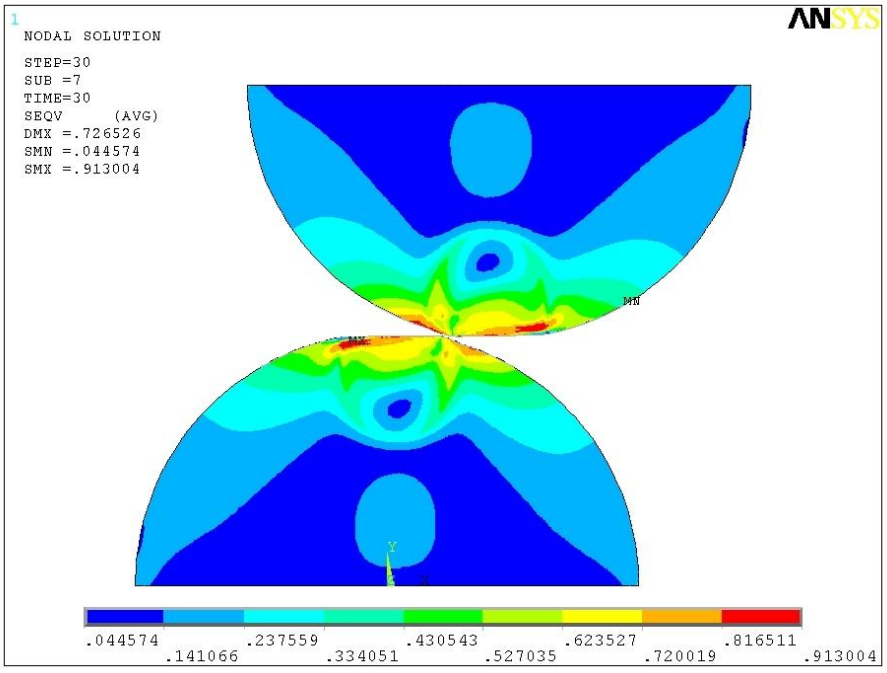

(b) ω* = 20

Figure 11: Residual von Mises stress contours for sliding steel cylinders for (a) ω* = 15, and (b) ω* = 20

3.1.4.4 Energy Loss

Figure 12 shows the plot of U_{net}/ U_c for each of the preset vertical interferences, ω^*, as calculated from the FE simulations.

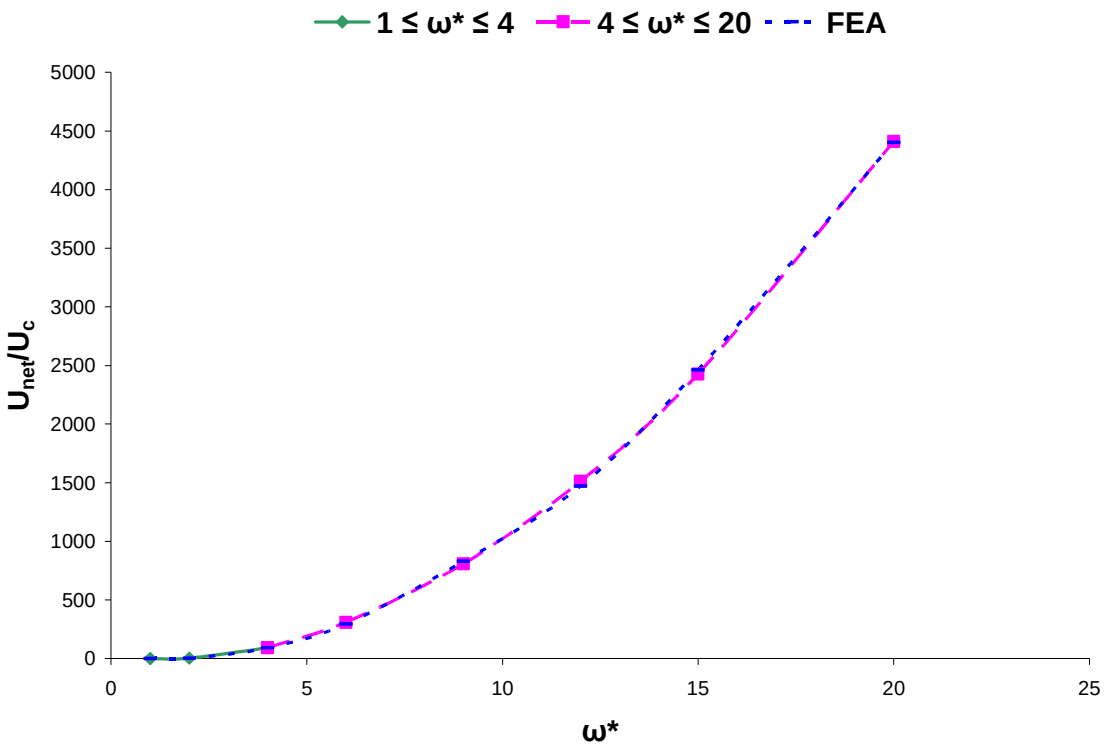

Figure 12: Normalized energy loss vs. normalized vertical interference

Second order polynomial curves are then fitted to the numerical data. They represent the trend followed by energy loss for different ranges of the applied vertical interference, ω^*, and are found to closely capture the increasing energy loss with increasingly elastic-plastic loading. The fitted equations are as follows:

$$\frac{U_{net}}{U_c} = 0 \qquad \omega^* \le 1$$

$$\frac{U_{net}}{U_c} = -9.487(\omega^* - 1) + 13.409(\omega^* - 1)^2 \qquad 1 \le \omega^* \le 4 \qquad (7)$$

$$\frac{U_{net}}{U_c} = 92.221 + 85.238(\omega^* - 4) + 12.133(\omega^* - 4)^2 \qquad 4 \le \omega^* \le 20$$

3.1.4.5 Contact Half-width

Figure 13 shows the trend followed by the contact half-width, *b*, as it changes with each load step as sliding with different vertical interferences progresses. It is normalized by the critical contact half-width, b_c, given in Table 1 and is hence plotted as the ratio b^*. It is observed that the contact half width curve for sliding with vertical interference $\omega^* = 1$ is symmetric about the vertical axis of alignment where the cylinders are exactly on top of each other. As ω^* increases, the curves get more and more skewed at the loading phase of the sliding process. Also in Figure 13, the value of the contact half-width is given by the symbol 'x' for perfectly symmetric, normal contact simulation between the same cylinders, designated by ω_n. For $\omega^* = 1$, as expected the contact half-widths for the sliding and normal loading cases is found to be the same. However, for interferences $\omega^* \geq 1$, the contact half-widths, b^*, for normal loading of cylinders are consistently higher than those for sliding interference at the vertical axis of alignment.

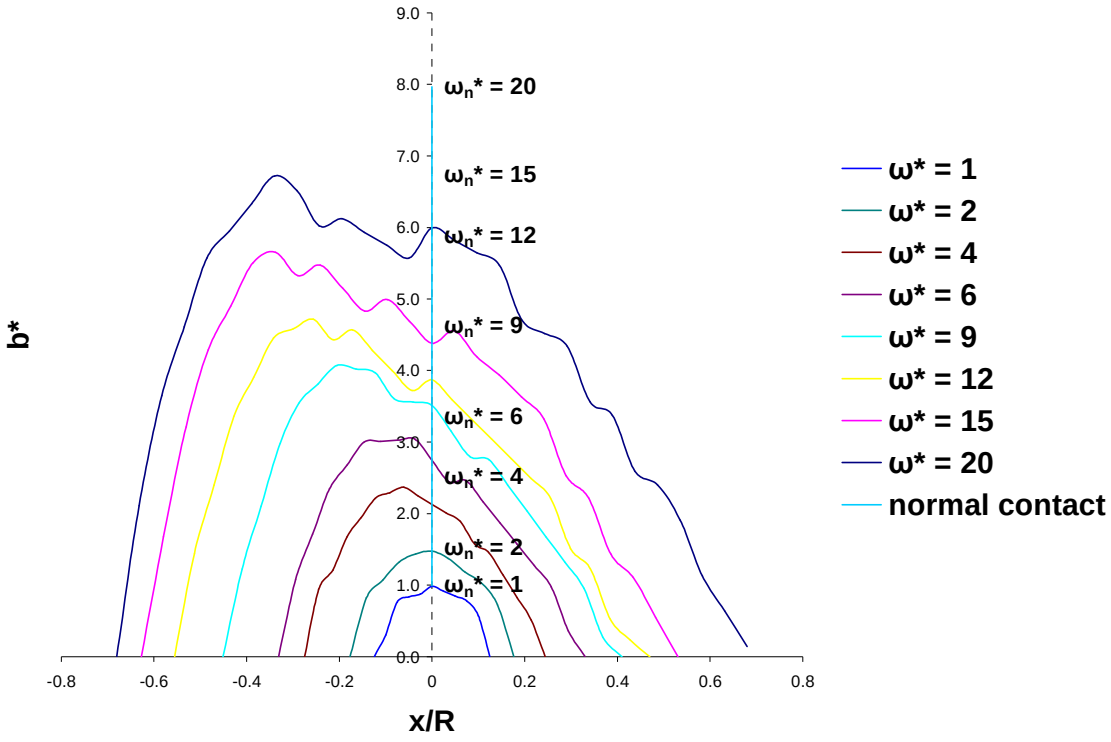

Figure 13: Normalized contact half-width for each load step vs. normalized sliding distance

This is due to the fact that for normal loading, the vertical deformation of the nodes in the contact region is much greater than that in the horizontal. On the other hand, the horizontal component of the displacement of the nodes in the contact region becomes more and more dominant as the applied vertical interference is increased during sliding. For sliding in the elastic-plastic loading regime, there is plastic deformation and because of material flow, the contact width also 'slides' along with the sliding of the top cylinder over the bottom cylinder. Thus, at any give stage of sliding, less number of nodes are in contact than there are for normal contact under the same vertical interference.

3.2 Glidcop (Cu) on Al 6061-T651 (Al) Sliding

3.2.1 Approach

FEA of the sliding of a Glidcop cylinder (99.63% Cu, 0.16% Al, 0.0016% Fe, 0.0005% Pb, 0.020% B) over an Al 6061-T651 cylinder (97.5% Al, 0.3% Cr, 0.15% Cu, 0.7% Fe, 0.8% Mg, 0.15% Mn, 0.4% Si) are discussed in this section. These particular materials are chosen for analysis because of their use in the EML under investigation. While the rail in the EML is made of Glidcop, the armature that serves to propel the projectile is an Aluminum alloy Al 6061-T651. In the actual EML environment, material properties depend on the temperatures that result from high-speed sliding. These temperature effects are ignored and the aforementioned properties are taken to be at room temperature. The methodology employed is very similar to the approach used in section 3.1.1. For this section, the critical values of P_c/L, b_c, ω_c, and U_c/L shown in Table 3 are calculated for the two cylinders with material properties as follows: $E_{Al} = 68.9$ GPa, $E_{Cu} = 130$ GPa, $\nu_{Al} = 0.330$, $\nu_{Cu} = 0.326$, $S_{y_{Al}} = 0.310$ GPa, and $S_{y_{Cu}} = 0.331$ GPa. Since $(CS_y)_{Al} < (CS_y)_{Cu}$, $(CS_y)_{Al}$ is used for evaluating the critical values.

Table 3: Critical values of parameters at the onset of plasticity for sliding between Al and Cu cylinders

Parameter	Value
C_{Al}	1.829
$(CS_y)_{Al}$	0.567 GPa
ω_c	0.591 mm
P_c/L	9.98 MN/m
b_c/L	0.01123
U_c/L	0.2795 kN

Again, only one-pass sliding is simulated. The FE model used in this analysis is the same as that used in section 3.1. The geometry, meshing, and boundary condition imposed are exactly as described in section 3.1.2. In the FE model, the lower cylinder is assigned the material properties of Al 6061-T651, and the upper cylinder those of Glidcop. Although both materials are modeled as elastic-perfectly plastic, a small value of the tangent modulus is specified in the FE material models to aid in convergence of the solutions. It is found that this helps in achieving convergence for sliding with small vertical interferences. It should be noted that these materials are alloys used in the specific application of the EML under investigation, and selection of different material properties for this study may very well yield results that vary significantly from those presented here. Hereafter, Glidcop is referred to as Cu, and Al 6061-T651 as Al for the sake of convenience.

3.2.2 Results and Discussion

The results are presented for a range of preset normalized vertical interferences, ω^*, from *1* (elastic limit) to *20* (elastic-plastic). The computation time is about an hour for sliding with small vertical interferences to about *4* hours for sliding with larger interferences on a dual processor Xeon *3* GHz PC with hyperthreading turned on to utilize four virtual processors.

3.2.2.1 Deformations

The deformation pattern followed by the cylinders in this case differ significantly for the two cylinders unlike in section 3.1.4.1, where both cylinders are modeled with the same material properties. This is obviously due to the fact that they have different material properties. The maximum vertical displacements of the nodes on either cylinder surface are monitored in order to understand the deformation of the cylinders. The maximum vertical displacement, $u_{y,}$ thus obtained is effectively normalized by the critical interference ω_c given in Table 3. Sliding is attained piecewise as the top cylinder (Cu) traverses a total displacement, Δx (see Figure 3). For the presentation of the results, x is being normalized by the equivalent radius of the cylinders, R, such that $x/R < 0$ signifies loading, and $x/R > 0$ signifies unloading as in 3.1.4.1. The cylinders are perfectly aligned at $x/R = 0$. Plots of the normalized maximum vertical displacement, u_y/ω_c, with respect to the normalized sliding distance of the top cylinder, x/R, are presented for the aforementioned range of ω^* for the bottom (Al) as well as the top (Cu) cylinders in Figure 14 and Figure 15, respectively. It can be seen from these deformation plots that the maximum nodal displacements on the Al cylinder are much higher than those on the

Cu cylinder. Figure 14 shows an increase in u_y for the Al cylinder even after sliding is completed. This is due to material pile-up that is caused by tugging and the excessive plastic deformation.

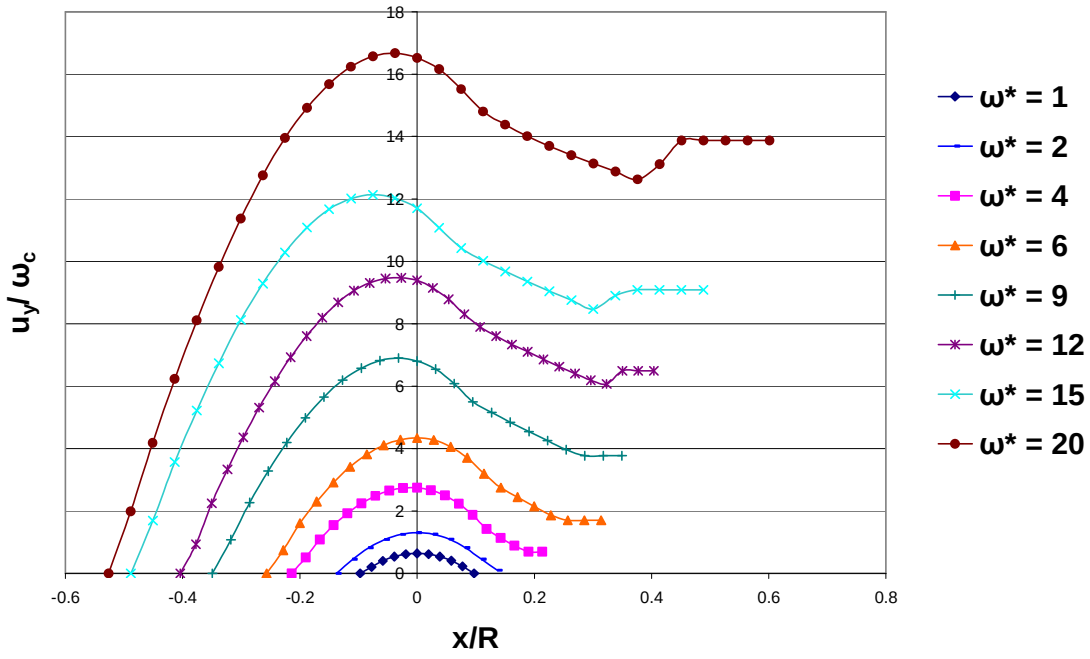

Figure 14: Normalized maximum vertical displacement vs. normalized sliding distance for the Al 6061-T651 cylinder for frictionless Al-Cu sliding

The Cu cylinder, on the other hand, experiences deformations of smaller magnitude as shown in Figure 15. It is also observed that there is no increase in u_y in the Cu cylinder after sliding is completed (i.e., no pile-up is created for Cu). The maximum deformation that occurs at the vertical axis of alignment is found to be significantly smaller on the Cu cylinder as compared to that on the Al cylinder for all value of the

applied vertical interference, ω_c. Also, the sum of the maximum deformations on the Al and Cu cylinders is greater than the vertical interference as the maximum is not at the center of contact as in the normal loading case. Also, the points where the maximum values are found are not necessarily vertically aligned with each other.

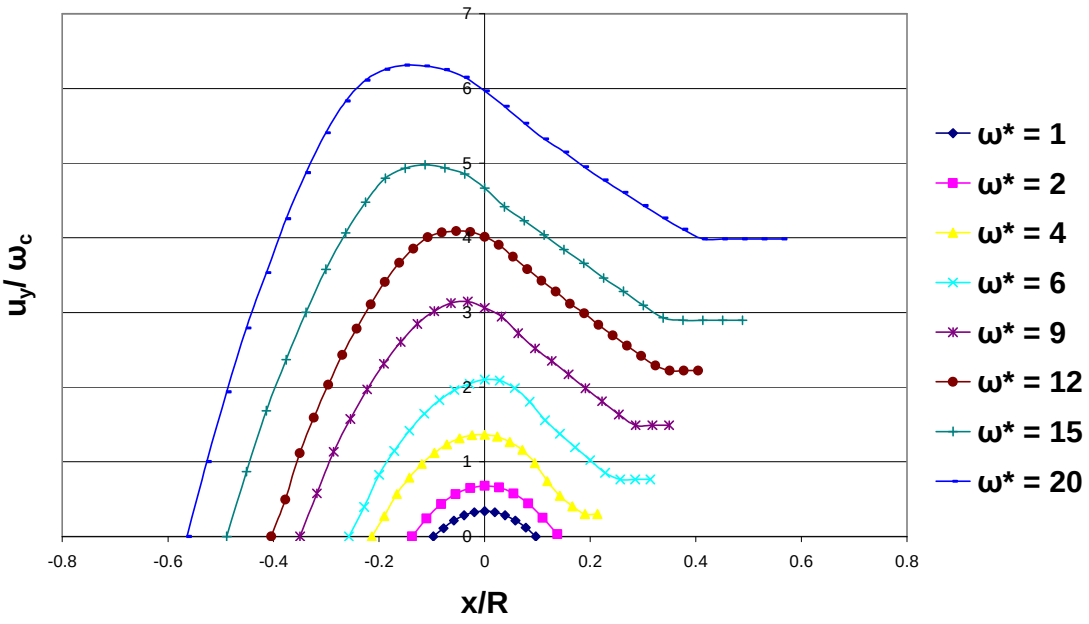

Figure 15: Normalized maximum vertical displacement vs. normalized sliding distance for the Glidcop cylinder for frictionless Al-Cu sliding

3.2.2.2 Forces

Reaction forces at the base nodes of the bottom Al cylinder are summed for each load step and plotted against the normalized horizontal sliding distance *x/R*. Both the normal reaction force, F_x, and the tangential reaction force, F_y, are normalized by the

critical load, P_c given in Table 3. Figure 16 and Figure 17 show the trends followed by F_x/P_c and F_y/P_c, respectively, as the top (Cu) cylinder slides across the bottom (Al) one.

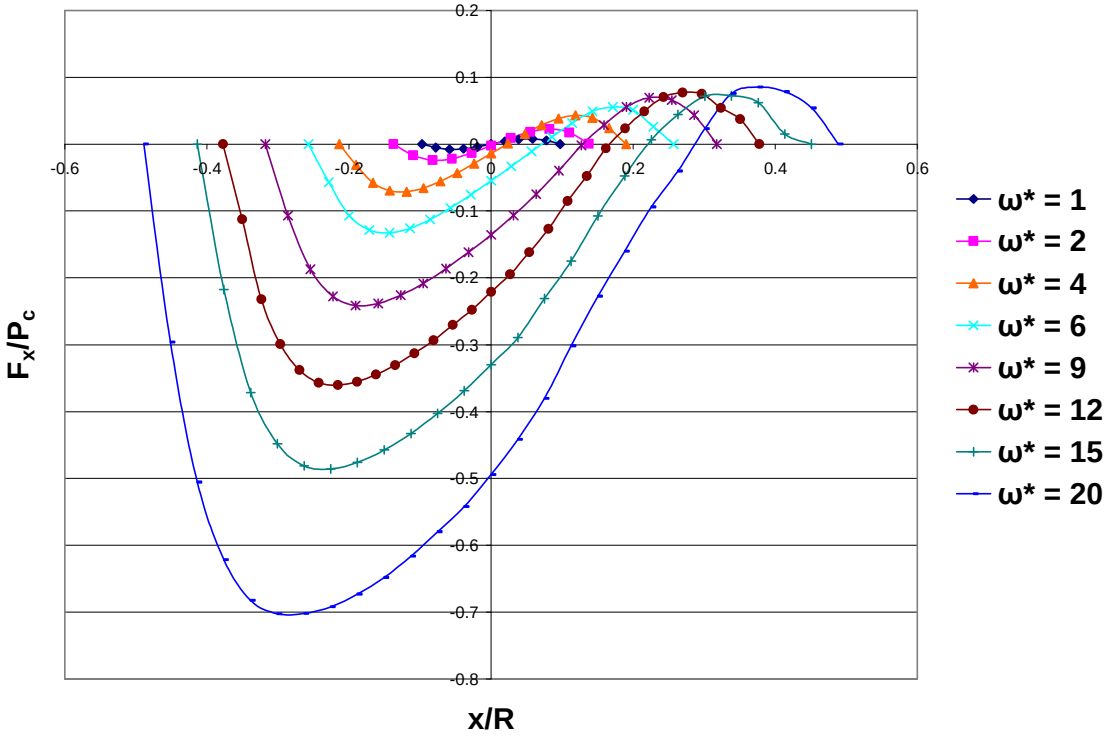

Figure 16: Normalized horizontal reaction force vs. normalized sliding distance for frictionless Al-Cu sliding

The normalized peak values of F_x/P_c induced in the Al-Cu sliding case are much lower that those in steel-steel sliding (for example, F_x/P_c = -0.7 for Al-Cu and F_x/P_c = -0.85 for steel-steel sliding) before the top cylinder passes the horizontal axis of alignment at x/R = 0. This is noted from Figure 7 and Figure 16, respectively, for steel-steel and Al-Cu sliding. However, the peak values of F_y/P_c for Al-Cu and steel-steel sliding before x/R = 0 are found be almost the same (for example, F_y/P_c = 11.5 for Al-Cu and F_y/P_c = 10.5

for steel-steel sliding at $x/R = 0$).These patterns are observed because of the higher yield strength of steel compared to that of Cu and Al.

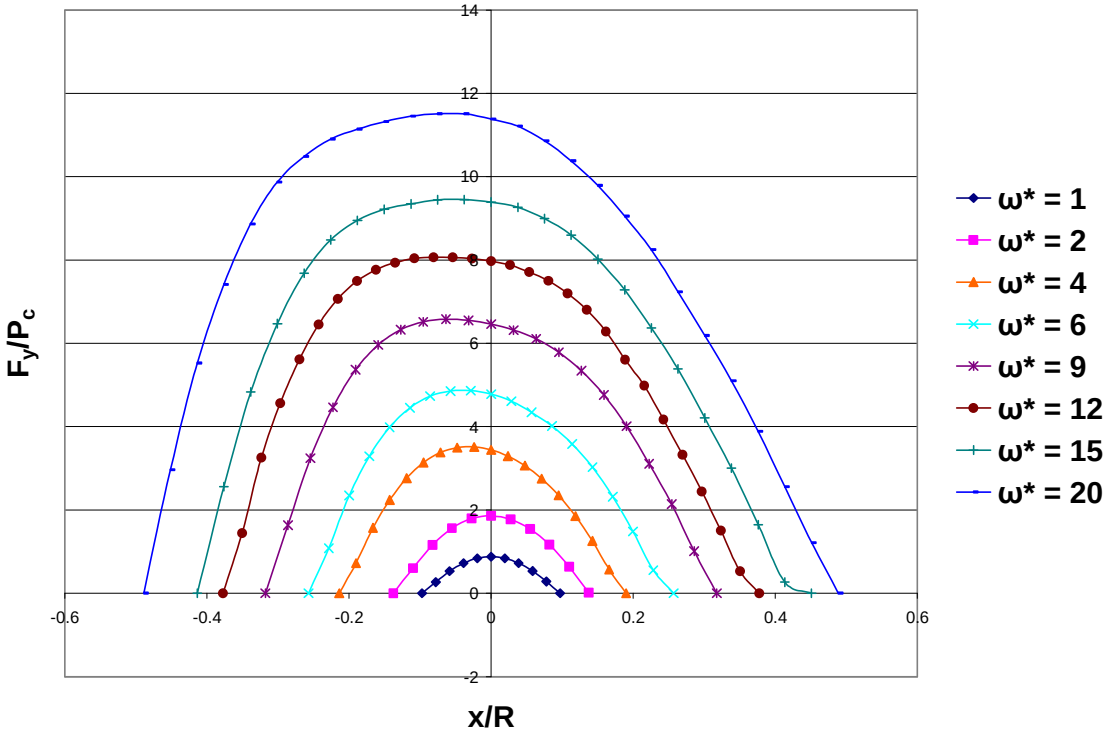

Figure 17: Normalized vertical reaction force vs. normalized sliding distance for frictionless Al-Cu sliding

As discussed in 3.1.4.2, it is apparent that for the vertical interference $\omega^* = 1$, the curve is anti-symmetric in Figure 16, and symmetric in Figure 17 signifying no loss of energy once sliding is completed. However, for the elastic-plastic loading cases, where $\omega^* > 1$, permanent plastic deformation occurs and some energy is lost in the process. This is evident from Figure 16 as the area under (energy invested in sliding) is larger than that above (energy restored in rebound) for all the curves in the elastic-plastic regime. This

shows that more work is done in pushing the top cylinder across the bottom one in the loading phase, than what is earned once it has passed the vertical axis of alignment in the unloading phase where both cylinders are repelling each other. Also, it is apparent from Figure 17 that the normalized vertical reaction force, F_y, is symmetric for $\omega^* = 1$, but becomes higher and increasingly skewed during loading than unloading as the applied vertical interference is increased. This may be attributed to predominantly elastic resistance during loading which diminishes once plasticity spreads in the contact.

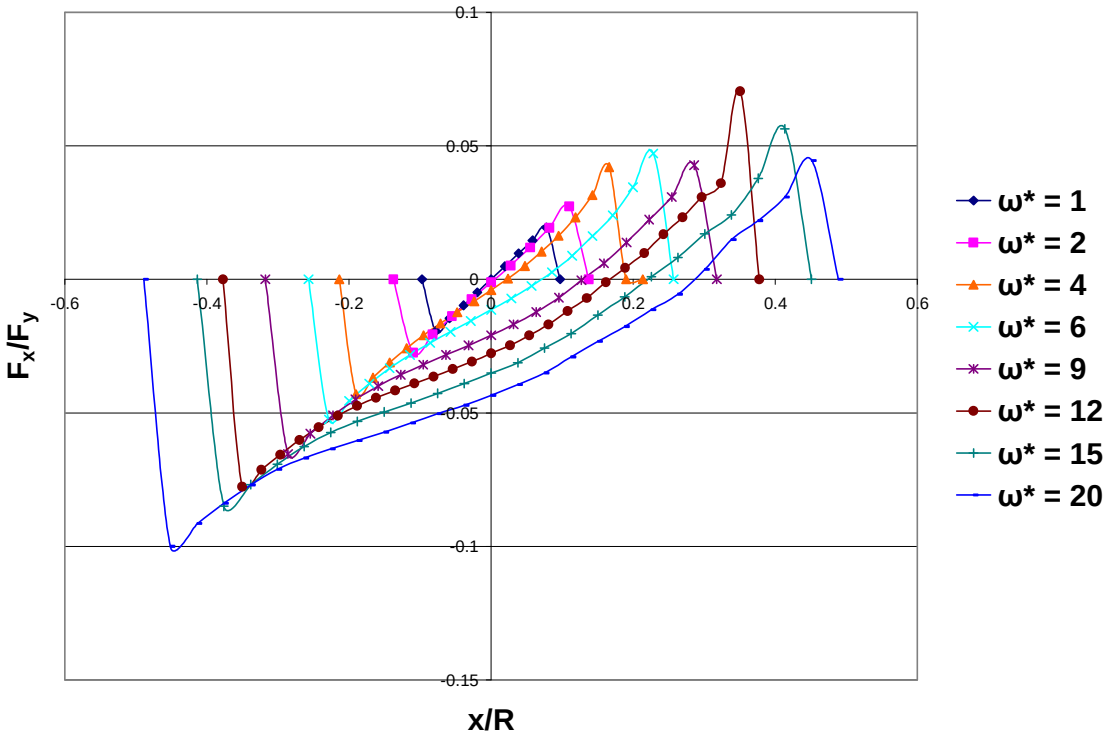

Figure 18: "Load Ratio" vs. normalized sliding distance for frictionless Al-Cu sliding

The peak values of F_x/F_y induced in the Al-cu sliding are lower (for example, F_x/F_y = -0.1 for Al-Cu and F_x/F_y = -0.13 for steel-steel sliding) before the top cylinder

passes the horizontal axis of alignment at $x/R = 0$. This is noted for steel-steel and Al-Cu sliding from Figure 9 and Figure 18, respectively.

Again, it can be seen from Figure 18 that for the plastic loading cases, the ratio of the horizontal to the vertical reaction force is not zero at the point where the cylinders are perfectly aligned about the vertical axis as postulated by Kogut and Etsion [24].

3.2.2.3 Stress Formations

The stress regions formed in Cu and Al cylinders are expectedly found to be quite different as both have significantly different material properties. As in the steel-steel sliding case discussed in 3.1.4.3, at low interferences the high stress region develops below the contact interface. As sliding progresses and load on the cylinders increases for the elastic-plastic loading ranges, yielding occurs and a sub-surface plastic core develops (see Figure 19). This core is more widely spread in the Al cylinder as compared to the Cu one. Also, as can be seen from Figure 19 (ii), (iii), and (iv), for higher interferences the plastic core in the bottom Al cylinder shows a skew towards the direction of sliding. This goes to show that being the weaker material, Al experiences yielding earlier than Cu and region of yield shows a more evident effect of sliding.

As in the steel-steel sliding case, for lower elastic-plastic vertical interferences such as $\omega_c = 4$, high stresses remain near the area of contact, i.e., there is no significant stress formation at the base of the cylinders (where they may be connected to a bulk material). As the vertical interference increases, however, stresses can be seen developing in the body of the cylinder as well as at the base (see Figure 19). This effect is more prominent on the Al cylinder than the Cu one. This signifies shear tugging at the cylinder

base, and for vertical interference causing extreme plastic deformations, this might very well be the region with the highest stresses. This work concentrates on the elastic-plastic regime at the vicinity of contact, and hence only those results are presented here.

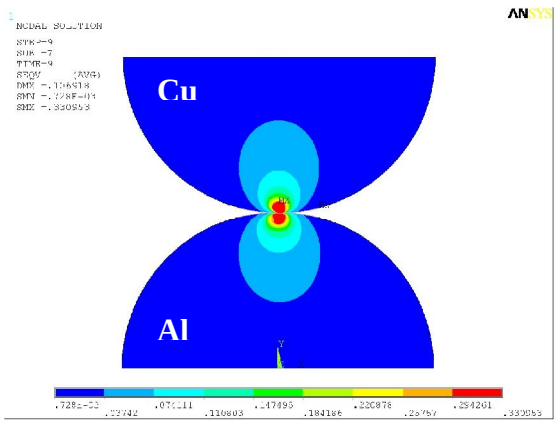

(i) ω* = 4

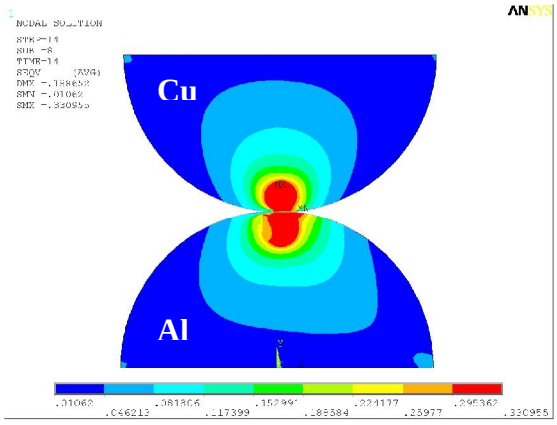

(ii) ω* = 12

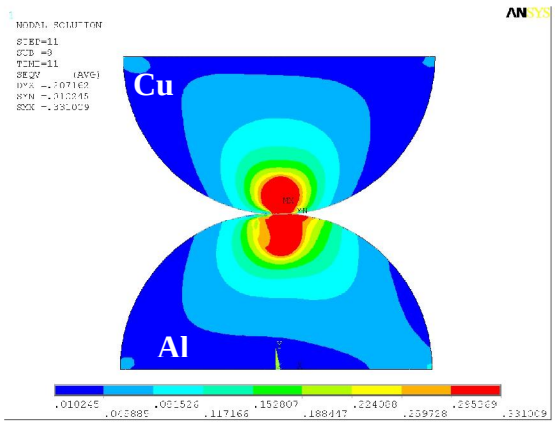

(iii) ω* = 15

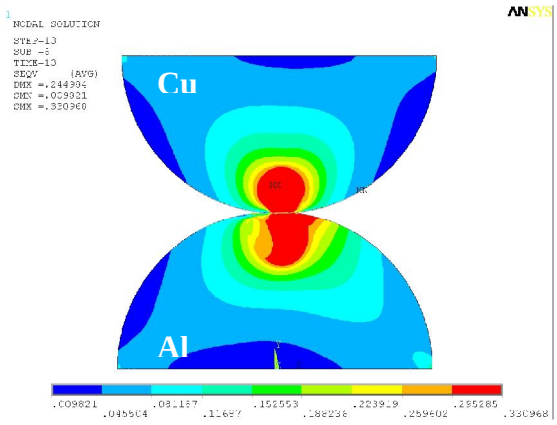

(iv) ω* = 20

Figure 19: von Mises stress contours for sliding cylindrical contact at vertical interferences of (i) ω* = 4, (ii) ω* = 12, (iii) ω* = 15, and (iv) ω* = 20 at the vertical axis of alignment for Al-Cu sliding

Figure 20 shows the distribution of the residual stresses after sliding is completed for the highest tested vertical interference values of $\omega^* = 15$, and $\omega^* = 20$. As expected, the residual stresses for the case with $\omega^* = 20$ are more widely spread than those for $\omega^* = 15$. The residual stress distribution in the Al cylinder is wider than in the Cu cylinder. Some of these stresses remain at the yield value (i.e., residual plastic strain). Although unlike the steel-steel sliding case, even for a high vertical interference such as $\omega^* = 20$ residual stresses are not found at the base of either cylinder. However, a spot indicating the presence of remnant stresses after sliding is seen in the Al cylinder for $\omega^* = 20$ in Figure 20 (ii). This indicates that for much larger vertical interferences, residual stresses can be expected to remain in the bulk of the cylinder and possibly spread towards the base as discovered in the case of steel-steel sliding. The magnitudes of the residual stress values are relatively lower for the Al-Cu sliding case as compared to that in the steel-steel sliding. This is due to the relatively lower yield strengths and elastic moduli of Al and Cu as compared to that of the steel material used. Plasticity is observed to reach the contact interface at approximately $\omega^* = 6$. Since the next highest vertical interference tested is $\omega^* = 9$, it can be roughly assessed that yielding at the contact interface occurs for sliding with $\omega^* = 6$.

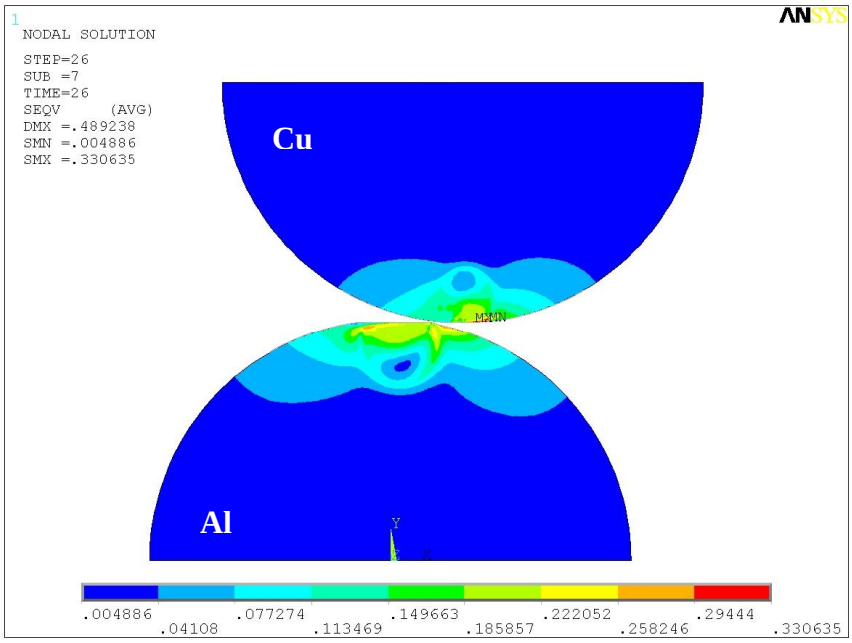

(a) ω* = 15

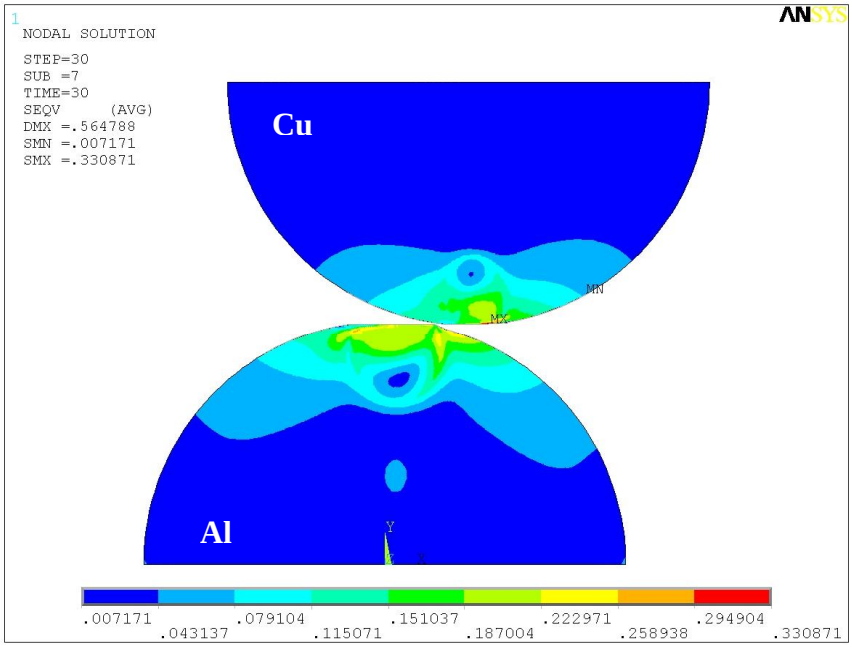

(b) ω* = 20

Figure 20: Residual von Mises stress contours for sliding steel cylinders for (a) ω* = 15, and (b) ω* = 20 for Al-Cu sliding

3.2.2.4 Energy Loss

Energy loss in sliding for individual preset vertical interference cases is separately calculated by evaluating the areas under each of their respective horizontal reaction curves in Figure 16. This represents the net work done when sliding the top Cu cylinder over the bottom Al one. The value thus obtained, U_{net}, is normalized by U_c listed for the specific materials Al 6061-T651 and Glidcop in Table 3. Figure 21 shows the plot of U_{net}/U_c for each of the preset vertical interferences, ω^*, as calculated from the FE simulations.

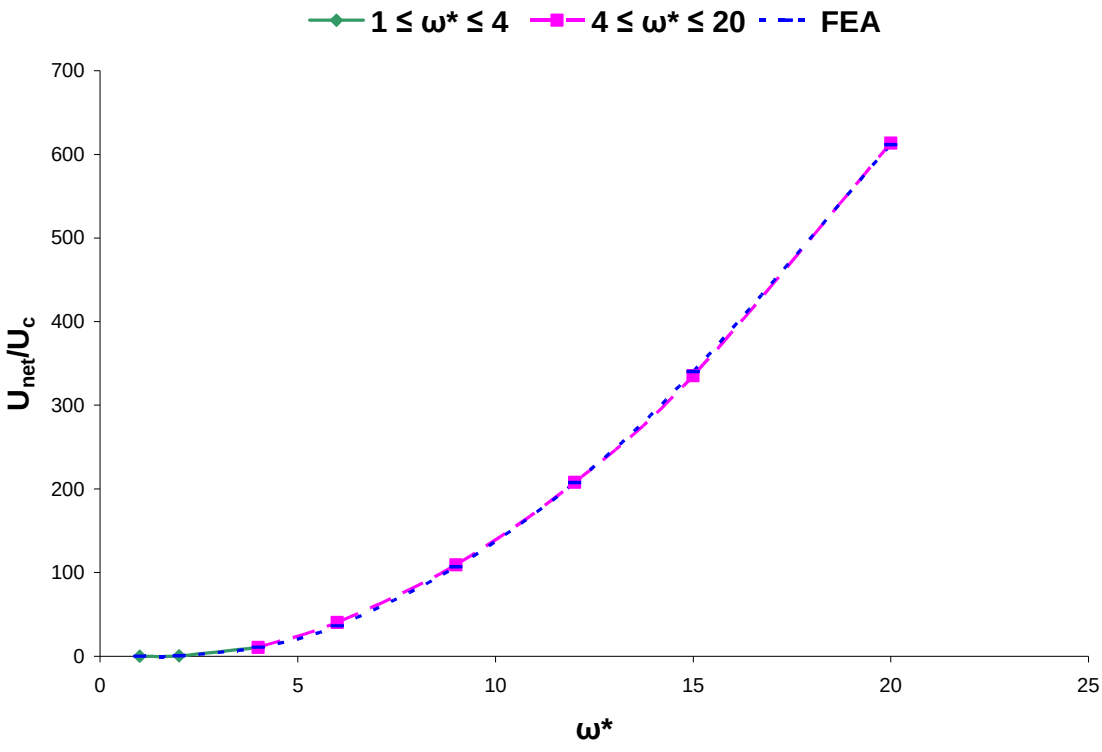

Figure 21: Normalized energy loss vs. normalized vertical interference for Al-Cu sliding

Second order polynomial curves are then fitted to the numerical data. They represent the trend followed by energy loss for different ranges of the applied vertical interference, ω^*, and are found to closely capture the increasing energy loss with increasingly elastic-plastic loading. The fitted equations are as follows:

$$\frac{U_{net}}{U_c} = 0 \qquad \omega^* \le 1$$

$$\frac{U_{net}}{U_c} = \text{-}1.087(\omega^* - 1) + 1.549(\omega^* - 1)^2 \qquad 1 \le \omega^* \le 4 \qquad (8)$$

$$\frac{U_{net}}{U_c} = 10.679 + 11.585(\omega^* - 4) + 1.630(\omega^* - 4)^2 \qquad 4 \le \omega^* \le 20$$

A comparative plot of the net energies as derived for sliding between steel-steel and Al-Cu cylinders is shown in Figure 22. It is clearly seen that the magnitudes of the net energy lost due to plasticity in the process of sliding is much higher in the case of sliding between two steel cylinders. This can be attributed to the fact that steel is stronger than both Al and Cu, and thus more work is required to be done in deforming it for the same applied vertical interference. Also, the Elastic modulus of steel (200GPa) is much higher than that of Al (68.9GPa) or Cu (130GPa). This means that more strain energy, U, can be stored during elastic deformation in steel than Al or Cu. It is also notable that for higher vertical interferences, the ratio of net energies for these two separate cases of sliding stabilizes at a value of about 7.

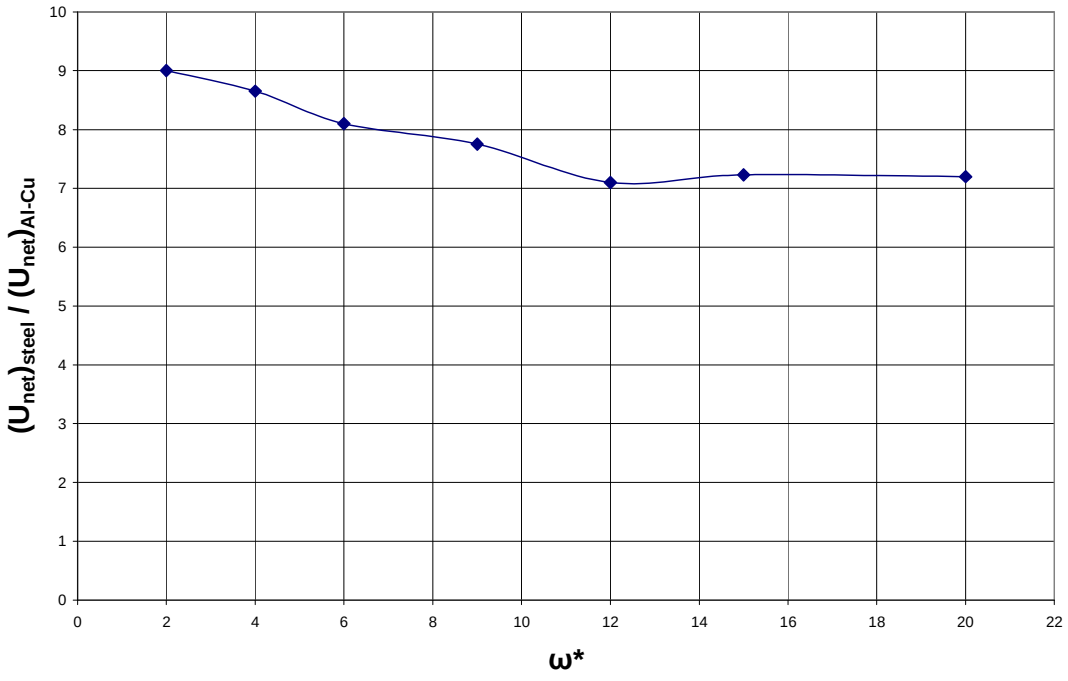

Figure 22: Ratio of net energies of steel-steel and Al-Cu sliding vs. normalized vertical interference

3.2.2.5 Contact Half-widths

Figure 23 shows the trend followed by the contact half-width, *b*, as it changes with each load step as sliding with different vertical interferences progresses. It is normalized by the critical contact half-width, b_c, given in Table 3 and is hence plotted as the ratio b^*. It is observed that the contact half width curve for sliding with vertical interference $\omega^* = 1$ is symmetric about the vertical axis of alignment where the cylinders are exactly on top of each other. As ω^* increases, the curves get more and more skewed at the loading phase of the sliding process.

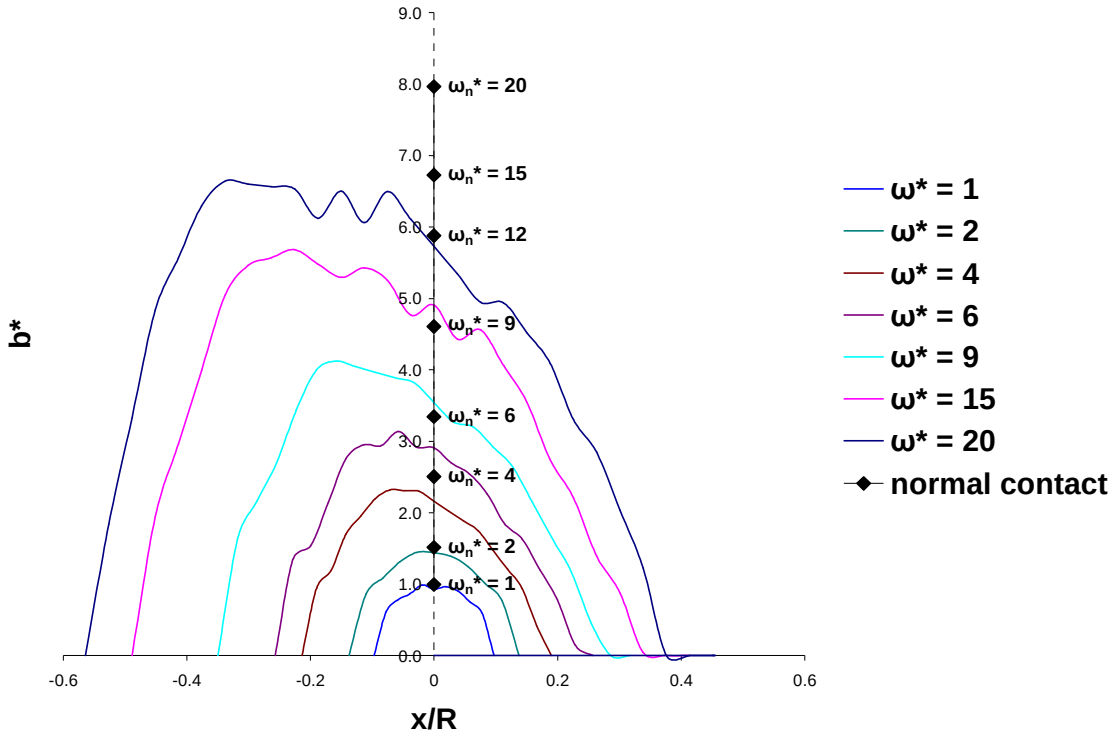

Figure 23: Normalized contact half-width for each load step vs. normalized sliding distance

The contact half-width patterns seen in Figure 23 found for Al-Cu sliding with various vertical interferences are found to be remarkably similar to those found on the case of steel-steel sliding (see Figure 13). The magnitudes of b^* match closely for the entire spectrum analyzed. Thus, it can be concluded that the material properties do not have much effect on the dimensions of contact between two sliding in frictionless sliding.

3.3 Conclusions

The results of the FEA of frictionless sliding in the elastic-plastic domain between two cylinders are discussed in this chapter. Sliding contact is analyzed for sliding between two steel cylinders and between an Al and a Cu cylinder. The resultant parameters such as deformations, forces, stresses, and energy losses that occur purely due to plasticity are understood. It can be deduced that such sliding under high vertical interferences, the stresses spread to the base of the cylinders and may very well be the key factor in the shear-off of the cylinder from the bulk. Also, for Al-Cu sliding, while the weaker material (Al) is found to have developed significant pile-up at the end of sliding, no such physical effects of sliding are found in the stronger material (Cu). Equations are derived to characterize the energy loss due to plastic deformation in both cases, and it is found the magnitudes of the net energy at the end of sliding are larger in the case of the stronger material (steel) that is analyzed. It is also found that the dimensions of the contact region are not affected by the material properties assigned to the sliding bodies.

CHAPTER 4: 2D ANALYSIS WITH FRICTION

4.1 Steel on Steel Sliding with μ = 0.3

4.1.1 Approach and Assumptions

In reality, there is no such phenomenon sliding between any two surfaces without friction. Friction plays an important, and in most cases pivotal, role in the behavior of surfaces as they slide over each other. Now that the part played by pure plastic deformation in elastic-plastic sliding has been analyzed, the next step is to see how friction combines with the aforementioned to affect the sliding process. This analysis is thus closer to the actual setting found in most applications, and hence a relatively common coefficient of friction of 0.3 is used for the purpose of the FEA. This helps in highlighting the part played by each of the two aforementioned factors.

The methodology employed for this analysis is the same as the approach used in section 3.1.1, except that in this case a coefficient of friction is introduced between the two sliding cylinders to study the effect of friction in such sliding. The coefficient of friction, μ, is given a value of 0.3 for this purpose. Only one-pass sliding is simulated. For this section, the critical values of P_c/L, b_c, ω_c, and U_c/L as listed in Table 1 are utilized. The FE model used in this analysis is the same as that used in section 3.1. The geometry, meshing, and boundary condition imposed are exactly as described in section 3.1.2. The assumptions listed in section 3.1.1 hold for this section as well; except that there is a coefficient of friction used and hence sliding is not frictionless.

4.1.2 Results and Discussion

The results are presented for a range of preset normalized vertical interferences, ω^*, from *1* (elastic limit) to *20* (elastic-plastic). The material properties used for the cylinders are chosen to be steel, which is commonly employed in many engineering applications. Convergence of the FE solution is more difficult to achieve for the low vertical interference cases as compared to the higher ones. Consequently, the computational times for these FEA are higher for the low vertical interference cases than for the high vertical interferences that induce much more plasticity.

4.1.2.1 Deformations

Since both cylinders are modeled with the same material properties, the deformation pattern followed by the two is identical. The maximum vertical displacements of the nodes on the cylinder surfaces are monitored in order to understand the deformation of the cylinders. The maximum vertical displacement, $u_{y,}$ is effectively normalized by the critical interference ω_c given in Table 1. Plots of the normalized maximum vertical displacement, u_y/ω_c, with respect to the normalized sliding distance of the top cylinder, x/R, are presented for the aforementioned range of ω^* in Figure 24.

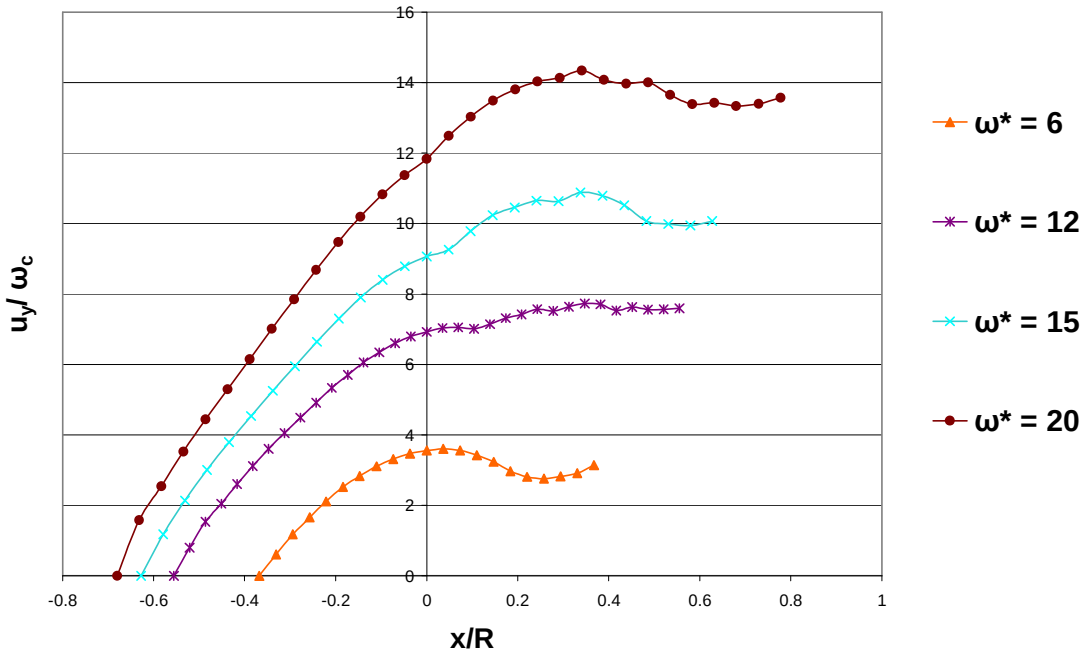

Figure 24: Normalized maximum vertical displacement vs. normalized sliding distance for steel-steel sliding with friction

The deformation curves in Figure 24 for all the vertical interferences shown are almost linear up to the vertical axis of alignment, i.e., $x/R = 0$. The normalized maximum vertical deformation, u_y/ω_c, keeps increasing even after the cylinders have passed $x/R = 0$. It is also notable that the deformation does not seem to decrease by much even after the cylinders have geometrically started moving out of contact. In fact, after a slight dip in the values, it seems to climb a fraction as can be seem from the curves in Figure 24. This implies severe plastic deformation at the contact interface, and results in negligible material elastic recovery after sliding is complete. Hence, there is significant material pile-up on both cylinders for high vertical interferences after frictional sliding. Figure 25

shows a zoomed-in contour of the material pile-up found at the contact interface after sliding in the case of $\omega^* = 15$.

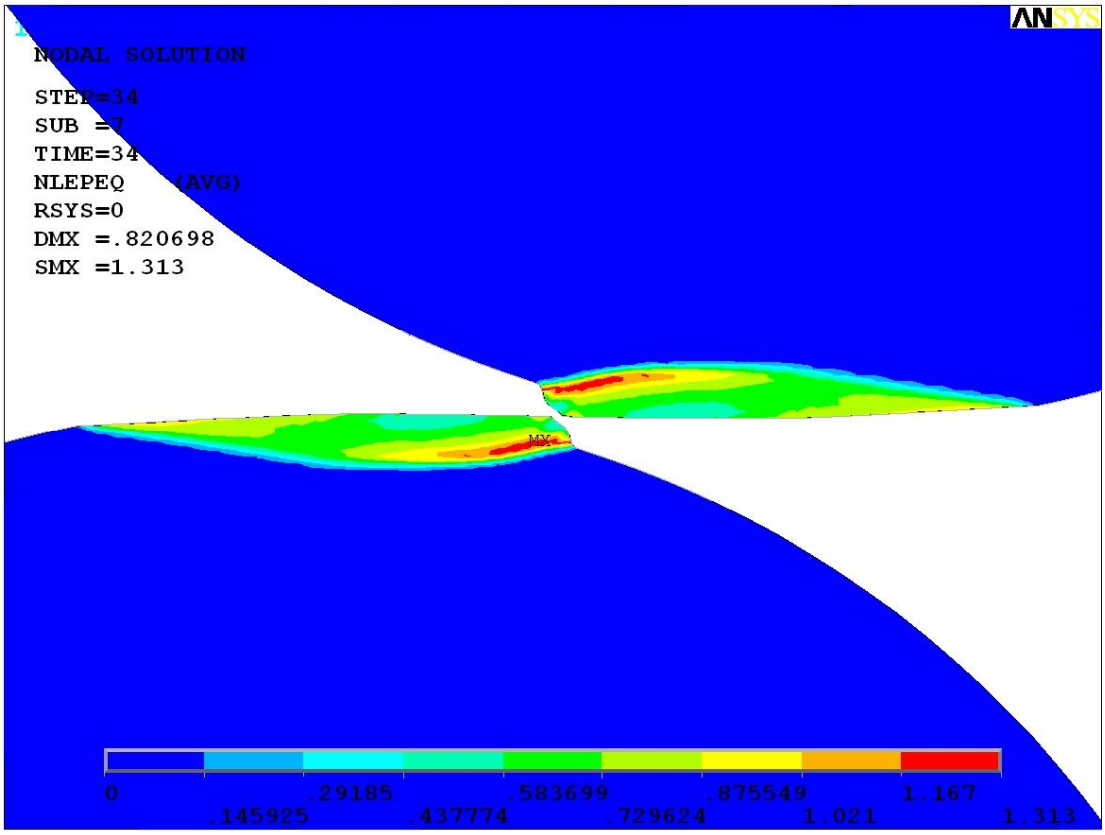

Figure 25: Equivalent plastic strain plot showing material pile-up for $\omega^* = 15$ for steel-steel sliding with friction

4.1.2.2 Forces

Reaction forces at the base nodes of the bottom cylinder are summed for each load step and plotted against the normalized horizontal sliding distance *x/R*. Both the normal reaction force, F_x, and the tangential reaction force, F_y, are normalized by the

critical load, P_c given in Table 1. Figure 26 and Figure 27 show the trends followed by F_x/P_c and F_y/P_c, respectively, as the top cylinder slides across the bottom one.

The curves seen in Figure 26 and Figure 27 show smooth trends for the normalized horizontal as well as vertical reaction forces for such frictional sliding. It is noteworthy that as the pre-applied vertical interference ω^* increases, the magnitudes of the reaction forces increase correspondingly. Also, the curves skew more and more towards the left of $x/R = 0$ for higher and higher applied vertical interferences.

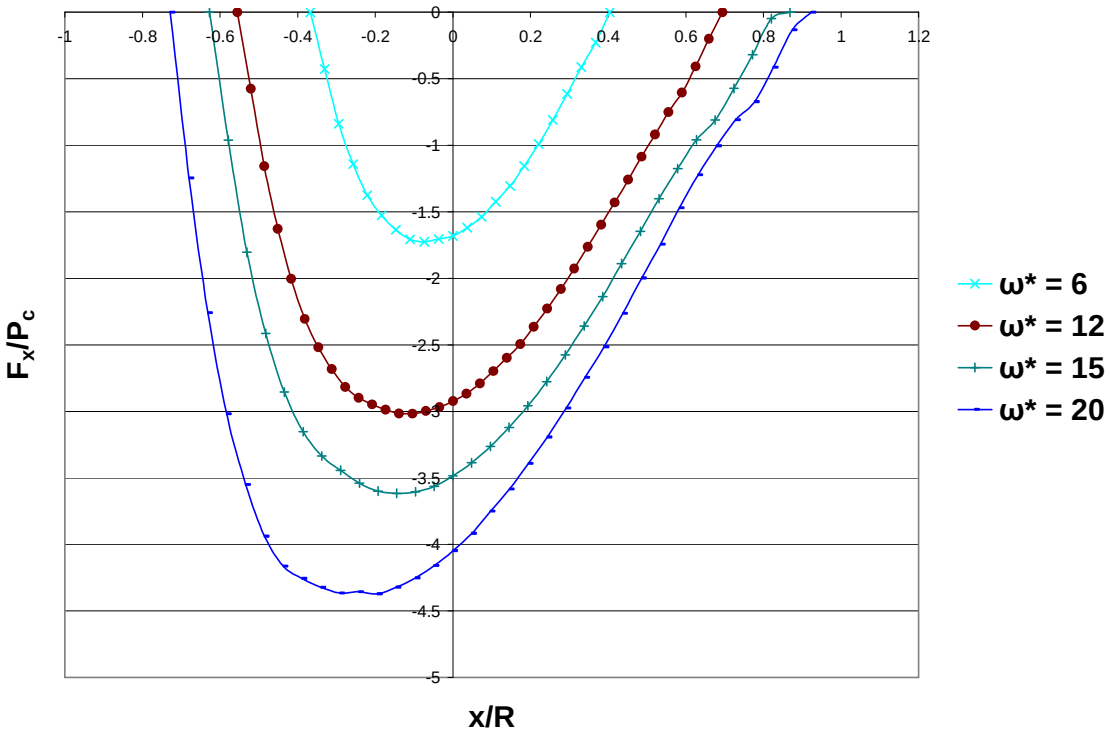

Figure 26: Normalized horizontal reaction force vs. normalized sliding distance for steel-steel sliding with friction

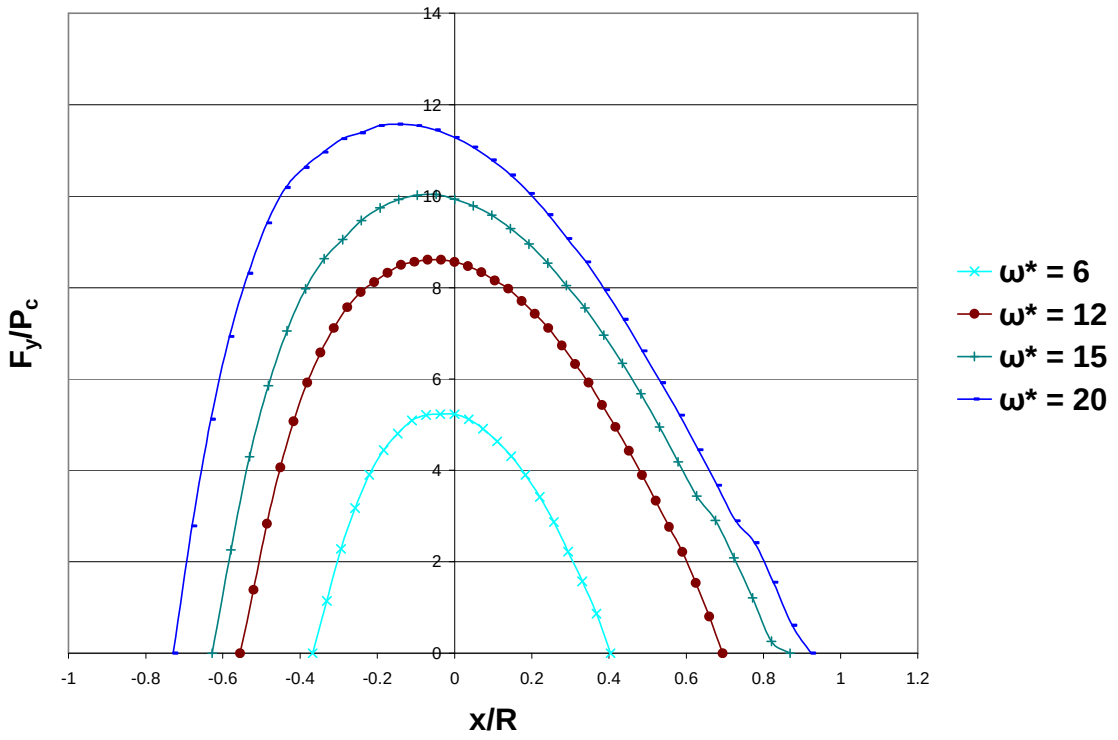

Figure 27: Normalized vertical reaction force vs. normalized sliding distance for steel-steel sliding with friction

As expected, the load ratio, F_x/F_y, never reaches a positive value for frictional sliding. This load ratio is plotted against x/R in Figure 28. It is evident that by and large the load ratio is greater than 0.3. The additional resistance to sliding is due to plasticity. Thus, F_x/F_y incorporates the effect of plastic deformation in sliding along with that of friction. The coefficient of friction, μ, which is assigned a value of 0.3 is also plotted as a reference line in Figure 28. This line serves as the demarcation between the resistance that is offered by plasticity to sliding and that by friction itself. It is observed that the load ratios are lower than 0.3 in the last stages of sliding. This is attributed to elastic recovery or rebound in the repelling cylinders.

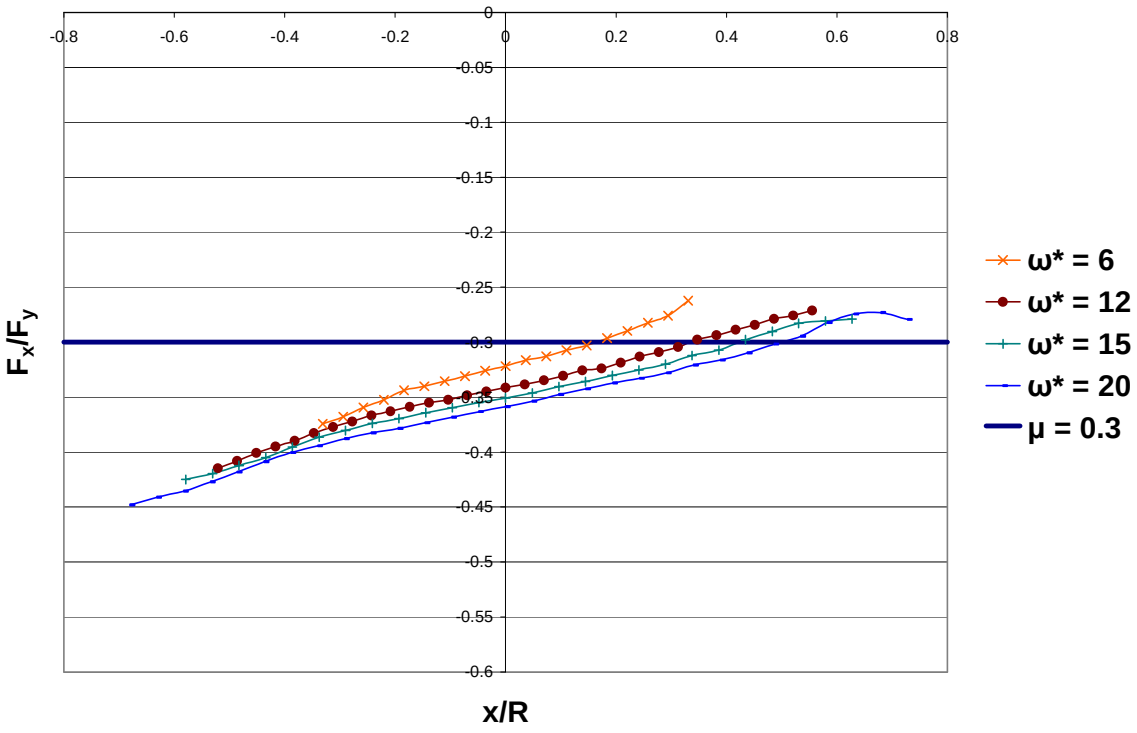

Figure 28: "Load Ratio" vs. normalized sliding distance for steel-steel sliding with friction

4.1.2.3 Stress Formations

The stress regions formed in both cylinders are anti-symmetric about the normal to the contact interface throughout the course of the sliding process, since identical material properties and geometries are used to model both cylinders. This holds for the elastic, as well as all of the elastic-plastic ranges. At low interferences, the high stress region develops below the contact interface. As sliding progresses and load on the cylinders increases for the elastic-plastic loading ranges, yielding occurs and a sub-surface plastic core develops. Elastic material surrounds this plastic core, and provides

the greater part of resistance to sliding. As the load increases with the progression of sliding (i.e., rendering an increase in the effective interference), the elastic region diminishes, making way for the growth and propagation of a plastic core, which reduces the resistance to sliding.

At the vertical axis of alignment, as seen from Figure 29, the von Mises stress distribution in both cylinders is mostly identical (in an anti-symmetric pattern about the normal to the contact interface). A larger portion of this stress concentration is seen to be in the direction opposite to sliding. This is the effect of friction between the two surfaces that hinders sliding and results in a tug opposing sliding and resulting in higher stress. For lower elastic-plastic vertical interferences, such as $\omega^* = 4$ (see Figure 29(i)—(a)), high stresses remain near the area of contact, i.e., there is no significant stress formation at the base of the cylinders (where they may be connected to a bulk material). As the vertical interference increases, however, stresses can be seen developing in the body of the cylinder as well as at the base (see Figure 29(ii)—(a) and (iii)—(a)). These stress concentrations at the base are found to be in the corners of the cylinders that are following their sliding motion, while no such stresses are seen on the other side. This signifies heavy shear tugging in that region, and for vertical interference causing extreme plastic deformations, this might very well be the region with the highest stresses. Contour plots for the same vertical interference for frictionless sliding are shown in Figure 29(i)—(b), (ii)—(b) and (iii)—(b). The stresses clearly develop very differently, and for higher vertical interferences of $\omega^* = 12$ and $\omega^* = 15$ there is a much larger stress build at the corners of the cylinders when friction is present.

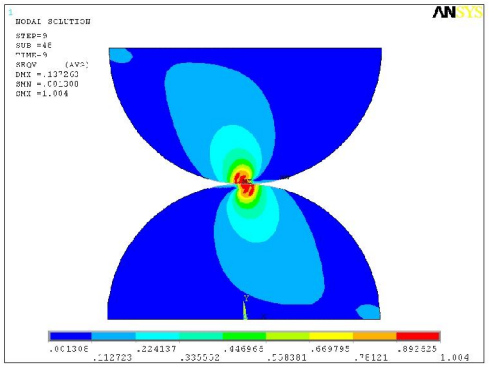

(i) – (a) $\omega^* = 4$ with friction

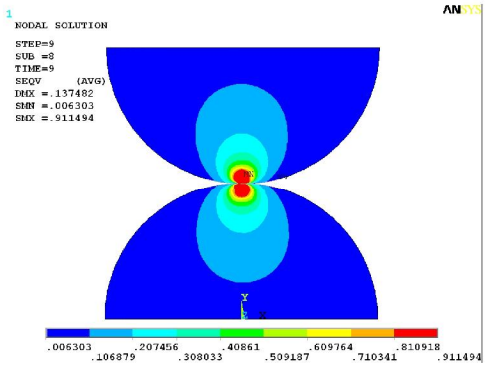

(i) – (b) $\omega^* = 4$ frictionless

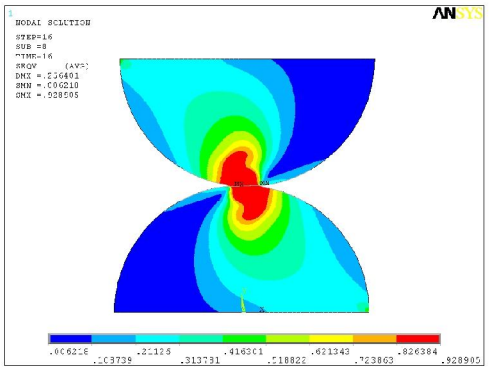

(ii) – (a) $\omega^* = 12$ with friction

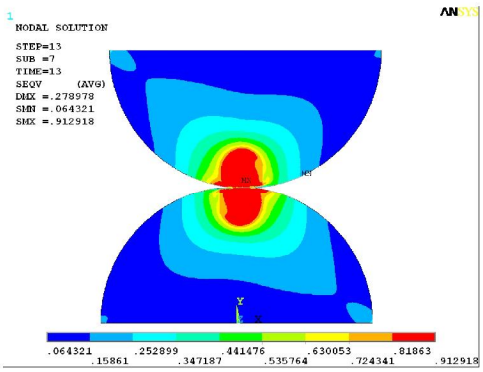

(ii) – (b) $\omega^* = 12$ frictionless

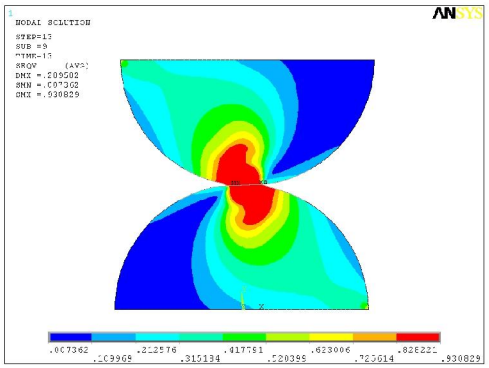

(iii) – (a) $\omega^* = 15$ with friction

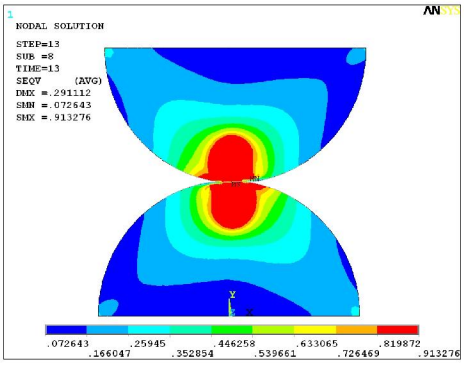

(iii) – (b) $\omega^* = 15$ frictionless

Figure 29: von Mises stress contours for (a) frictional and (b) frictionless steel-steel sliding cylindrical contact for vertical interferences of (i) $\omega^* = 4$, (ii) $\omega^* = 12$, (iii) $\omega^* = 15$, and (iv) $\omega^* = 20$ at the vertical axis of alignment for steel-steel sliding with friction

Figure 30 shows the distribution of the residual stresses after sliding is completed for the highest tested vertical interference values of $\omega^* = 15$, and $\omega^* = 20$. As expected, the residual stresses for the case with $\omega^* = 20$ are more widely spread than those for $\omega^* = 15$. The magnitude of the maximum residual von Mises stress after sliding with $\omega^* = 15$ is found to be 0.606GPa, whereas for sliding with $\omega^* = 20$ it is 0.672GPa. Thus higher residual stresses remain after sliding with higher vertical interferences. Also, there is considerable material pile-up as a result of which the surfaces of the sliding bodies are found to flatten because of severe plastic deformation. Plasticity is observed to reach the contact interface at approximately $\omega^* = 4$. Since the next highest vertical interference tested is $\omega^* = 6$, it can be roughly assessed that yielding at the contact interface occurs for sliding with $\omega^* = 4$. By comparison, this occurs at a lower interference than that in frictionless sliding.

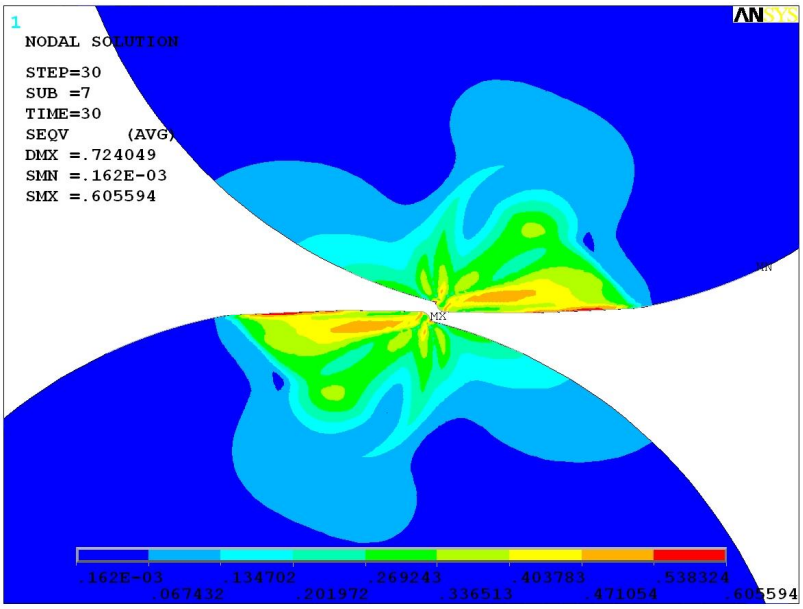

(a) $\omega^* = 15$

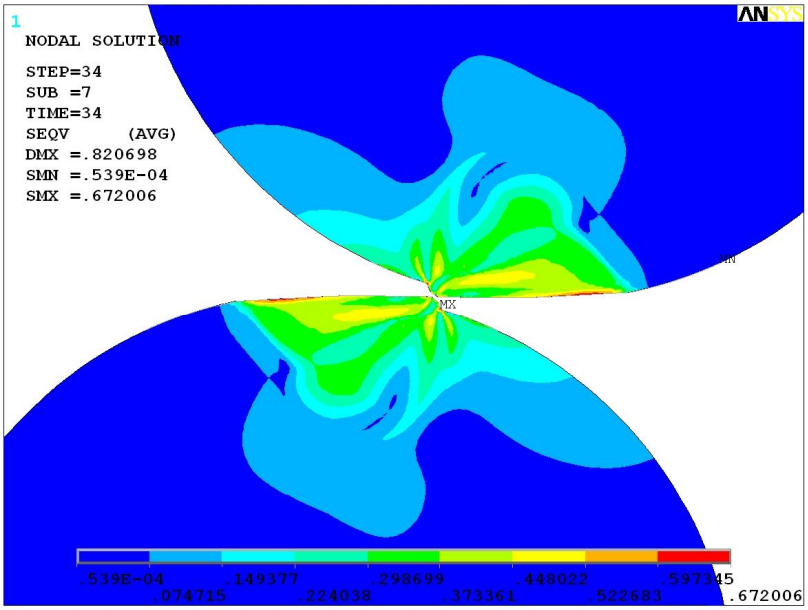

(b) $\omega^* = 20$

Figure 30: Residual von Mises stress contours for steel-steel sliding with friction for (a) ω* = 15, and (b) ω* = 20

4.1.2.4 Energy Loss

In the absence of displacement in the vertical direction in the overall sliding process, the net energy loss purely due to plastic deformation in frictional sliding can be defined as:

$$U_{net} = U_{total} - U_{friction}$$
$$U_{net} = \int_{x_1}^{x_2} F_x dx - \mu \int_{x_1}^{x_2} F_y dx \tag{9}$$

where x_1 and x_2 respectively represent the starting and ending sliding positions of the top cylinder. Thus, energy loss due to plasticity in frictional sliding for individual preset vertical interference cases is essentially the difference between the area under the true horizontal reaction curve and the true vertical reaction plotted against the true sliding distance scaled by the coefficient of friction, μ. The value thus obtained is called the net energy lost due to plastic deformation, U_{net}, and is normalized by U_c from Table 1.

Figure 31 shows the plot of U_{net}/ U_c for each of the preset vertical interferences, ω^*, as calculated from the FE simulations. A second order polynomial curve is then fitted to the numerical data. It represents the trend followed by energy loss for the range of the applied vertical interference, ω^*, and is found to closely capture the increasing energy loss with increasingly elastic-plastic loading. The fitted equations are as follows:

$$\frac{U_{net}}{U_c} = 0.690 - 2.980(\omega^* - 1) + 16.991(\omega^* - 1)^2 \qquad 1 \le \omega^* \le 6$$
$$\frac{U_{net}}{U_c} = 410.557 + 240.080(\omega^* - 6) + 9.809(\omega^* - 6)^2 \qquad 6 \le \omega^* \le 20 \tag{10}$$

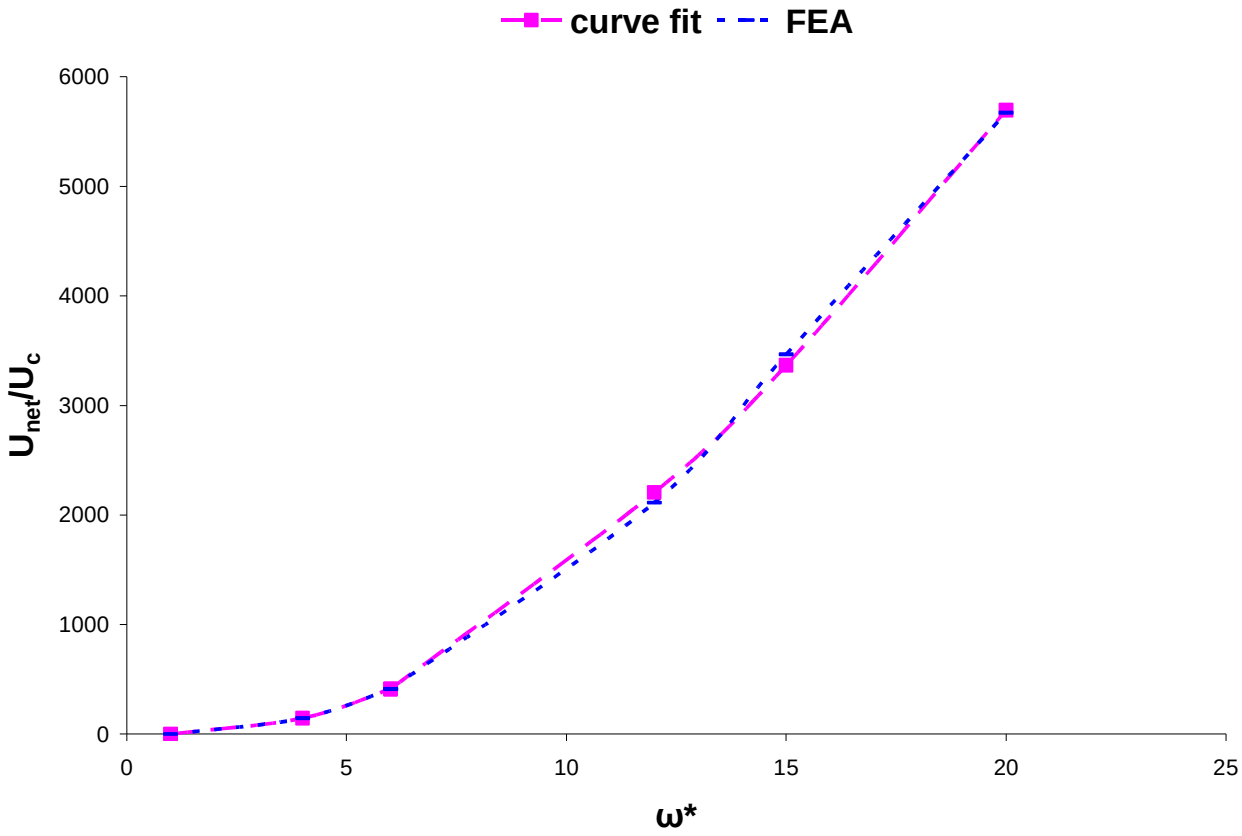

Figure 31: Normalized energy loss vs. normalized vertical interference

4.1.2.5 Contact Half-widths

Figure 32 shows the trend followed by the contact half-width, b, as it changes with each load step as sliding with different vertical interferences progresses. It is normalized by the critical contact half-width, b_c, give in Table 1 and is hence plotted as the ratio b^*. It is observed that the contact half width curves for sliding with all the preset vertical interferences is fairly symmetric about $x/R = 0$.

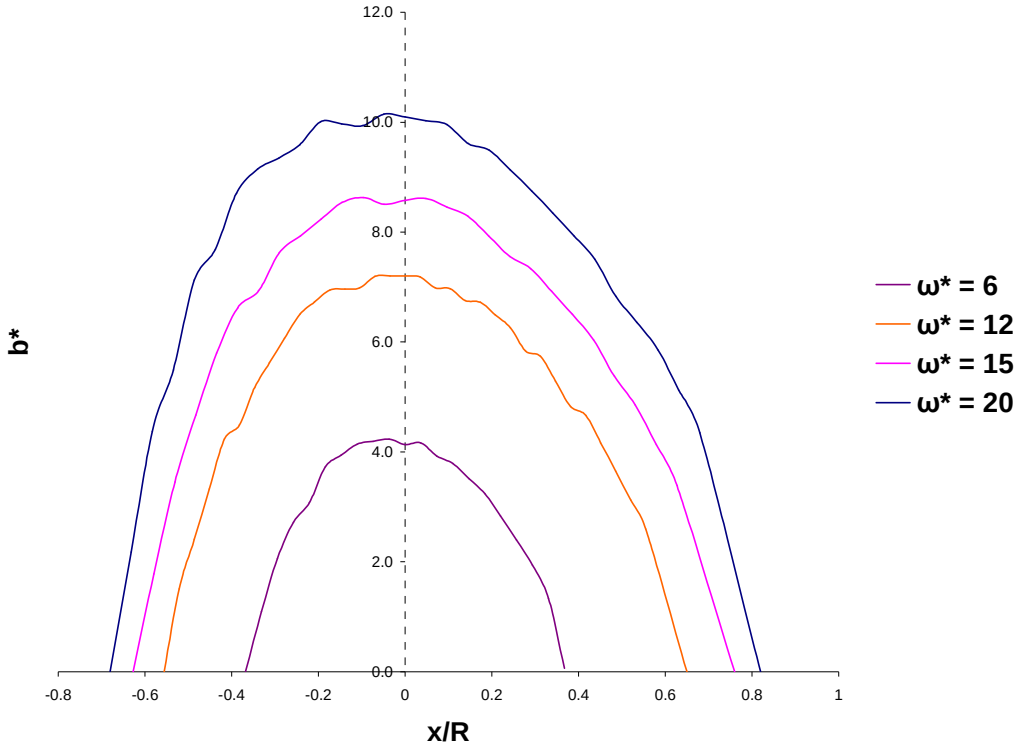

Figure 32: Normalized contact half-width for each load step vs. normalized sliding distance for steel-steel sliding with friction

4.2 Glidcop (Cu) on Al 6061-T651 (Al) Sliding with μ = 0.3

4.2.1 Approach

The methodology adopted for this analysis is the same as the approach used in section 3.2.1, except that in this case a coefficient of friction is introduced between the two sliding cylinders to study the effect of friction in 2D sliding. The coefficient of friction, μ, is given a value of 0.3 for this purpose. Only one-pass sliding is simulated. The critical values of P_c/L, b_c, ω_c, and U_c/L as listed in Table 3 are used.

The FE model used in this analysis is the same as that used in section 3.1. The geometry, meshing, and boundary condition imposed are exactly as described in section

3.1.2. The material for both the cylinders is modeled as elastic-perfectly plastic. The assumptions discussed in the previous section also hold for this analysis.

4.2.2 Results and Discussion

The results are presented for a range of preset normalized vertical interferences, ω^*, from *1* (elastic limit) to *20* (elastic-plastic). Convergence is harder to achieve for the low vertical interference cases as compared to the higher ones. Consequently, the computational times for these FEA are higher for the low vertical interference cases than for the high vertical interferences that induce much more plasticity.

4.2.2.1 Deformations

As in the frictionless sliding Al-Cu sliding case, the deformations experienced by the Al and Cu cylinders vary significantly. Since both cylinders are modeled with the same material properties, the deformation pattern followed by the two is identical. The maximum vertical displacements of the nodes on the cylinder surfaces are monitored in order to understand the deformation of the cylinders. The maximum vertical displacement, $u_{y,}$ is effectively normalized by the critical interference ω_c given in Table 3. Plots of the normalized maximum vertical displacement, u_y/ω_c, with respect to the normalized sliding distance of the top cylinder, x/R, are presented for the aforementioned range of ω^* for both the Al and Cu cylinders in Figure 33 and Figure 34 respectively.

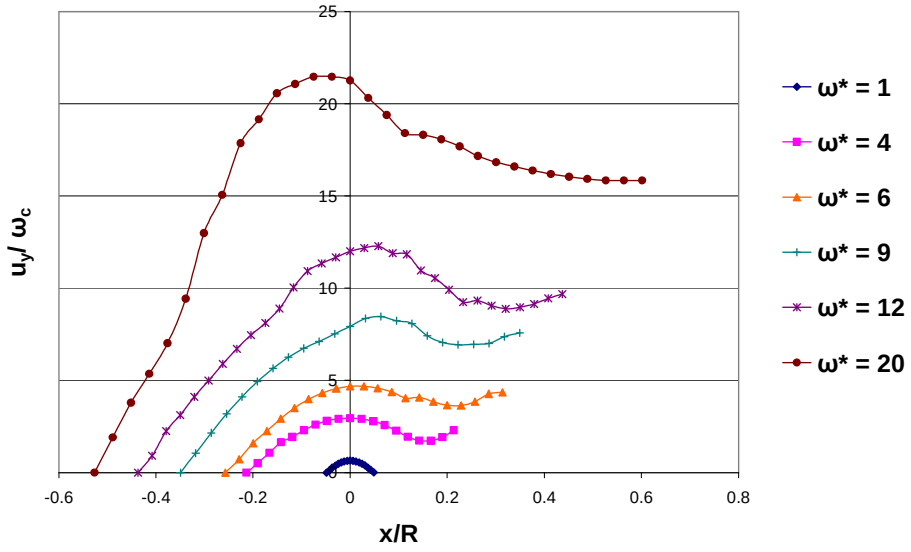

Figure 33: Normalized maximum vertical displacement vs. normalized sliding distance in the Al cylinder for Al-Cu sliding with friction

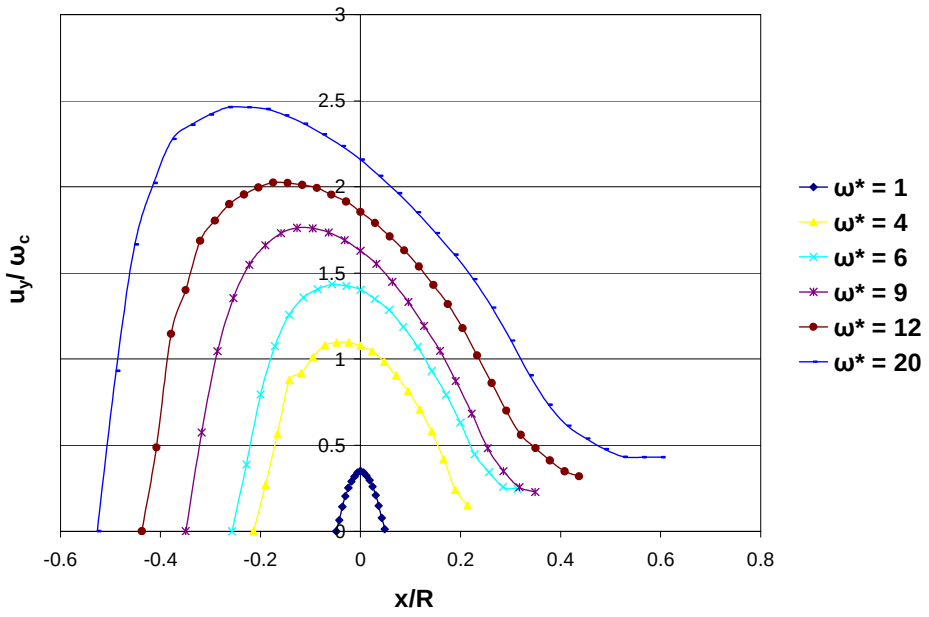

Figure 34: Normalized maximum vertical displacement vs. normalized sliding distance in the Cu cylinder for Al-Cu sliding with friction

The deformation curves for the Al cylinder are shown in Figure 33, and those for the Cu cylinder in Figure 34 for a range of vertical interferences. Cu being much stronger with higher yield strength than Al, the deformations on the Al cylinder are much larger in magnitude than those on the Cu cylinder. For the Al cylinder, the normalized maximum vertical deformation, u_y/ω_c, keeps increasing even after the cylinders have passed $x/R = 0$. It is also notable that the deformation does not seem to decrease by much even after the cylinders have geometrically started moving out of contact. In fact, after a slight dip in the values, it seems to climb a fraction as can be seem from the curves in Figure 33. This can be attributed to material pile-up on the Al cylinder. Such material pile-up occurs heavily for the higher vertical interferences, and is shown in Figure 35 for $\omega^* = 20$. It is clear from this deformation plot that while the Al cylinder experiences heavy plastic deformation, the Cu cylinder has almost negligible pile-up. Thus, the trends seen here are similar to those observed in frictionless Al-Cu sliding (see Figure 14 and Figure 15).

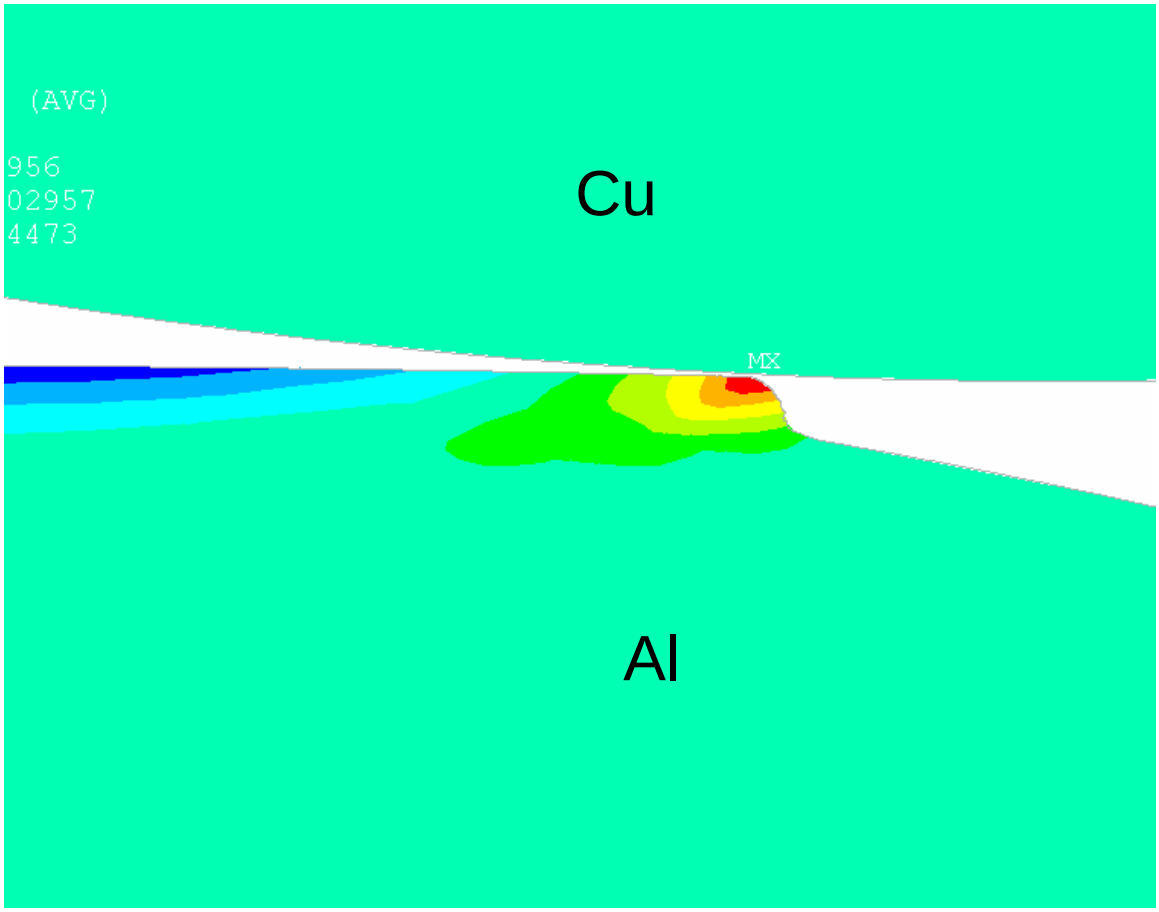

Figure 35: Equivalent plastic strain plot showing material pile-up after sliding for $\omega^* = 20$ for Al-Cu sliding with friction

4.2.2.2 Forces

Reaction forces at the base nodes of the bottom Al cylinder are summed for each load step and plotted against the normalized horizontal sliding distance *x/R*. Both the normal reaction force, F_x, and the tangential reaction force, F_y, are normalized by the critical load, P_c given in Table 3. Figure 36 and Figure 37 show the trends followed by F_x/P_c and F_y/P_c, respectively, as the top cylinder slides across the bottom one.

The curves seen in and Figure 36 and Figure 37 show smooth trends for the normalized horizontal as well as vertical reaction forces for such frictional sliding. It is noteworthy that as the pre-applied vertical interference ω^* increases, the magnitudes of the reaction forces increase correspondingly. Also, the curves skew more and more towards the left of $x/R = 0$ for higher and higher applied vertical interferences. This is evident from Figure 36 and Figure 37.

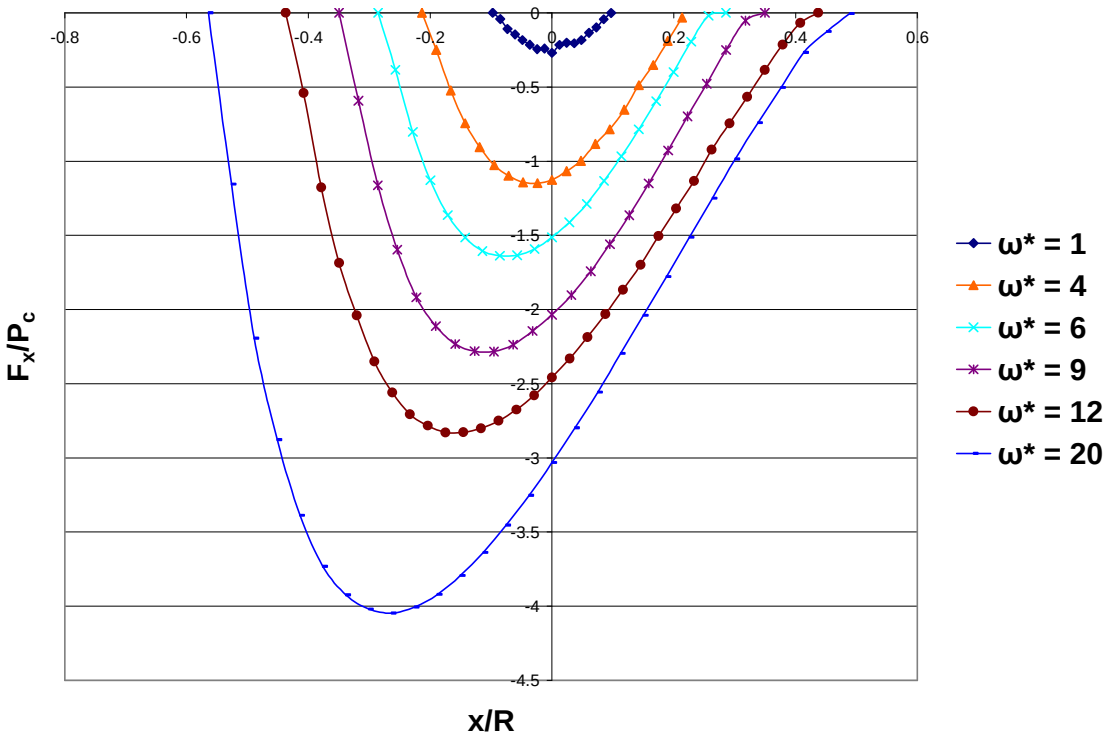

Figure 36: Normalized horizontal reaction force vs. normalized sliding distance for Al-Cu sliding with friction

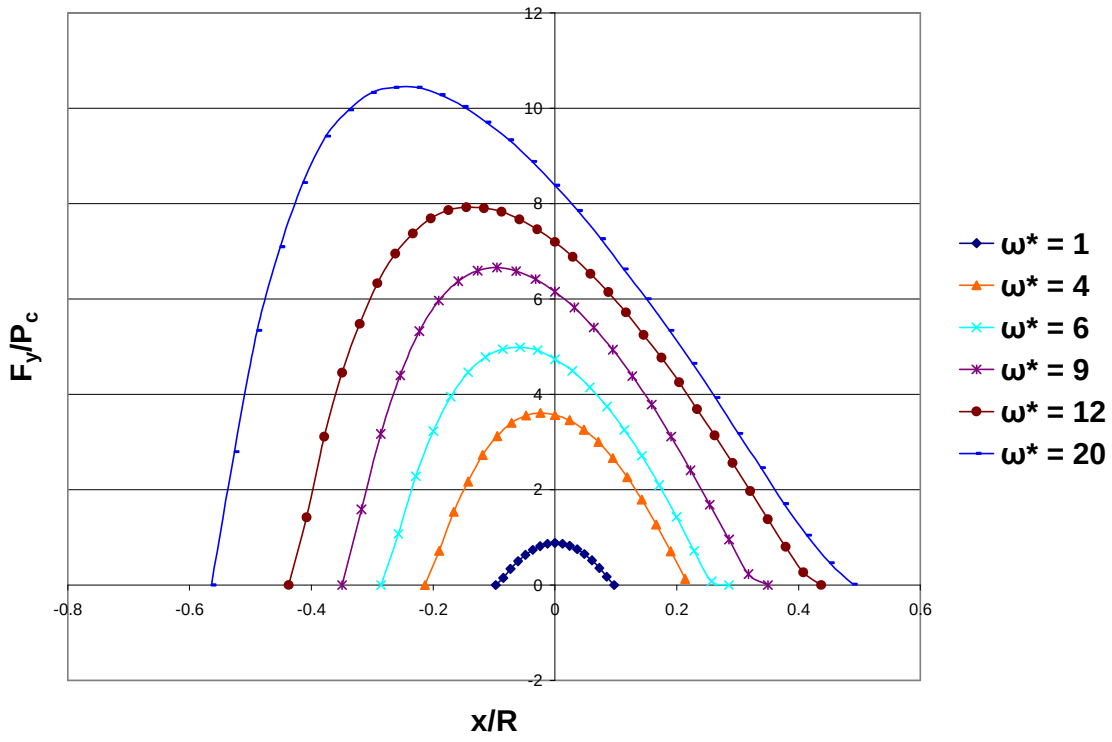

Figure 37: Normalized vertical reaction force vs. normalized sliding distance for Al-Cu sliding with friction

As in the steel-steel frictional sliding case, the load ratio, F_x/F_y, never reaches a positive value for frictional sliding. This load ratio is plotted against x/R in Figure 38. Here, F_x/F_y incorporates the effect of plastic deformation in sliding along with that of friction. It is evident that by and large the load ratio is greater than 0.3. The additional resistance to sliding is due to plasticity. Thus, F_x/F_y incorporates the effect of plastic deformation in sliding along with that of friction. The coefficient of friction, μ, that is assigned a value of 0.3 is also plotted as a line in Figure 38. This line serves as the demarcation between the resistance that is offered by plasticity to sliding and that by friction itself. It is observed that the load ratios are lower than 0.3 in the last stages of sliding. This is attributed to elastic recovery or rebound in the repelling cylinders. It is notable that the trends seen

here as similar to those found in frictionless sliding with a coefficient of friction of 0.3 superposed (see Figure 18).

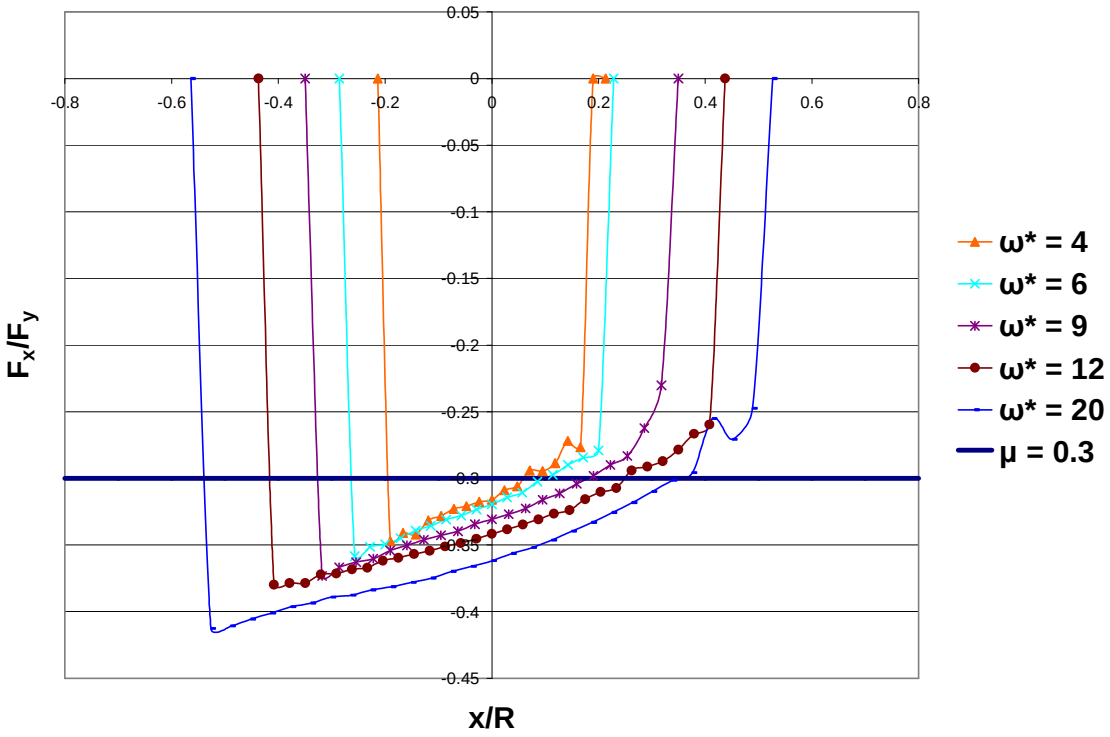

Figure 38: "Load Ratio" vs. normalized sliding distance for Al-Cu sliding with friction

4.2.2.3 Stress Formations

The stress regions formed in Cu and Al cylinders are expectedly found be quite different as both have significantly different material properties. As in the frictionless Al-Cu sliding case discussed in 3.2.2.3, at low interferences the high stress region develops below the contact interface. As sliding progresses and load on the cylinders increases for the elastic-plastic loading ranges, yielding occurs and a sub-surface plastic core develops (see Figure 39). This core is more widely spread in the Al cylinder as compared to the Cu one. Again, development of stresses is observed in the corners of the cylinders that are

against the sliding direction. These stresses are of higher magnitudes as the vertical interference increases. No symmetry is observed in the stress distribution in either cylinder. This is due to the presence of friction and vastly different material properties of Al and Cu. Contour plots for the same vertical interferences for frictionless sliding are shown in Figure 39(i)—(b), (ii)—(b) and (iii)—(b). The stresses clearly develop very differently, and for higher vertical interferences of $\omega^* = 12$ and $\omega^* = 20$ there is a much larger stress build at the corners of the cylinders when friction is present. This is especially true in the Al cylinders since it deforms more than the Cu cylinder. Plasticity is observed to reach the contact interface at approximately $\omega^* = 4$. Since the next highest vertical interference tested is $\omega^* = 6$, it can be roughly assessed that yielding at the contact interface occurs for sliding with $\omega^* = 4$.

Figure 40 shows the distribution of the residual stresses after sliding is completed for the highest tested vertical interference values of $\omega^* = 12$, and $\omega^* = 20$. As expected, the residual stresses in the Al cylinder more widely spread than those in the Cu cylinder. The material pile-up in the Al cylinder is not as massive as in the case of steel-steel sliding with friction as seen in Figure 25. In the Cu cylinder, the pile-up is negligible.

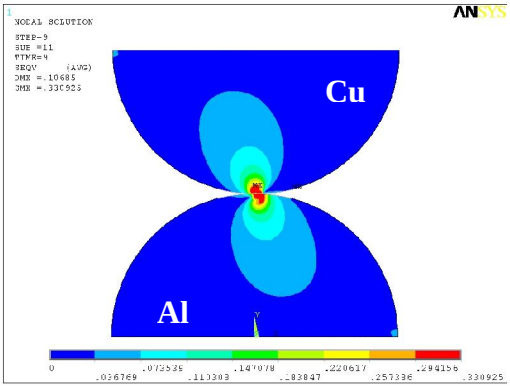

(i -- a) ω* = 4 with friction

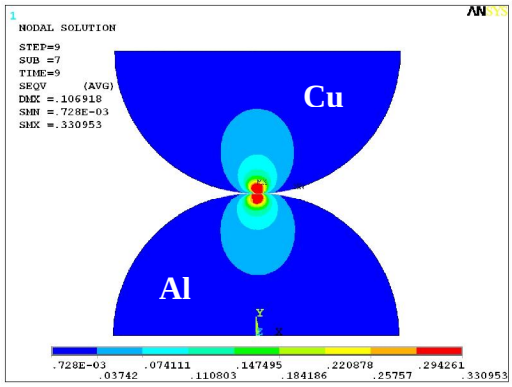

(i -- b) ω* = 4 frictionless

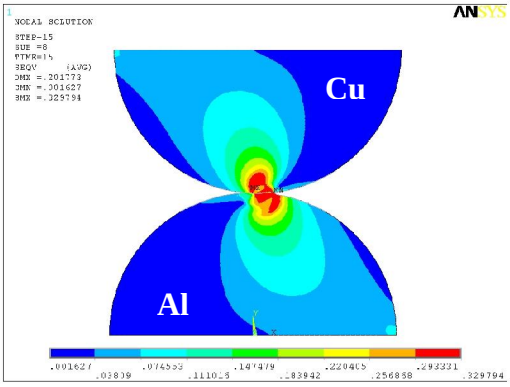

(ii -- a) ω* = 12 with friction

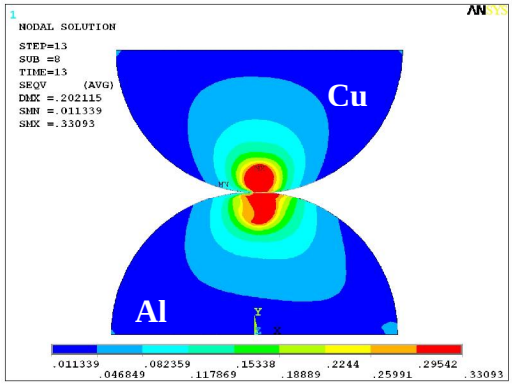

(ii -- b) ω* = 12 frictionless

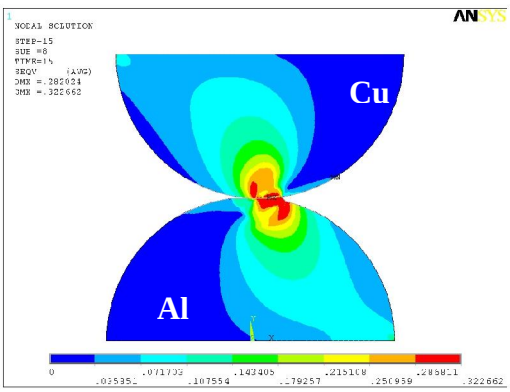

(iii -- a) ω* = 20 with friction

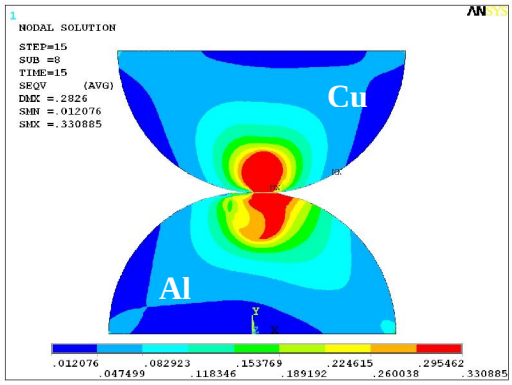

(iii -- b) ω* = 20 frictionless

Figure 39: von Mises stress contours for (a) frictional and (b) frictionless Al-Cu sliding contact for vertical interferences of (i) ω* = 4, (ii) ω* = 12, and (iii) ω* = 20 at the vertical axis of alignment

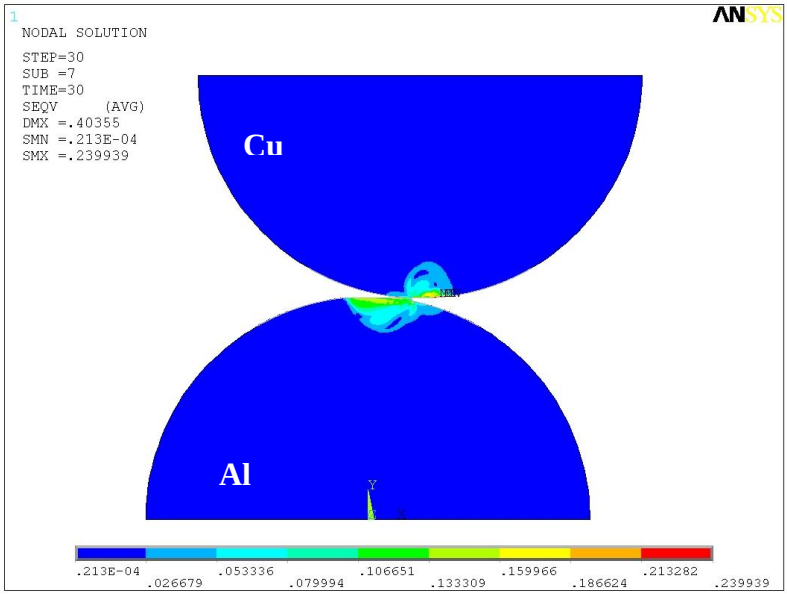

(a) $\omega^* = 12$

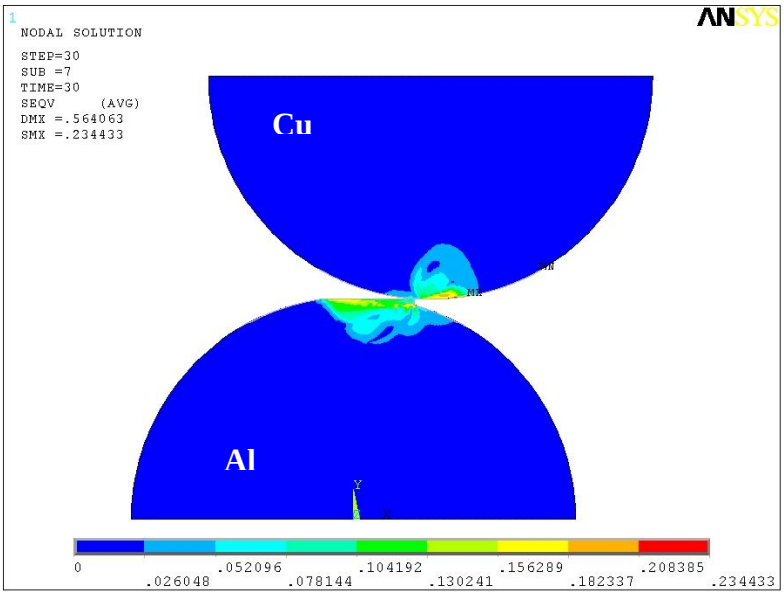

(b) $\omega^* = 20$

Figure 40: Residual von Mises stress contours for Al-Cu sliding contact with friction for (a) $\omega^* = 15$, and (b) $\omega^* = 20$

4.2.2.4 Energy Loss

The net energy loss in frictional sliding can again be defined as in Eq. (10) .The value thus obtained is called the net energy lost due to plastic deformation, U_{net}, and is normalized by U_c from Table 3.

Figure 41 shows the plot of U_{net}/ U_c for each of the preset vertical interferences, ω^*, as calculated from the FE simulations. A second order polynomial curve is then fitted to the numerical data. It represents the trend followed by energy loss for the range of the applied vertical interference, ω^*, and is found to closely capture the increasing energy loss with increasingly elastic-plastic loading. The fitted equation is as follows:

$$\frac{U_{net}}{U_c} = 0 \qquad \omega^* \le 1$$

$$\frac{U_{net}}{U_c} = 4.761 - 4.569(\omega^* - 1) + 3.690(\omega^* - 1)^2 \qquad 1 \le \omega^* \le 6 \qquad (11)$$

$$\frac{U_{net}}{U_c} = 74.165 + 39.649(\omega^* - 6) + 1.552(\omega^* - 6)^2 \qquad 6 \le \omega^* \le 20$$

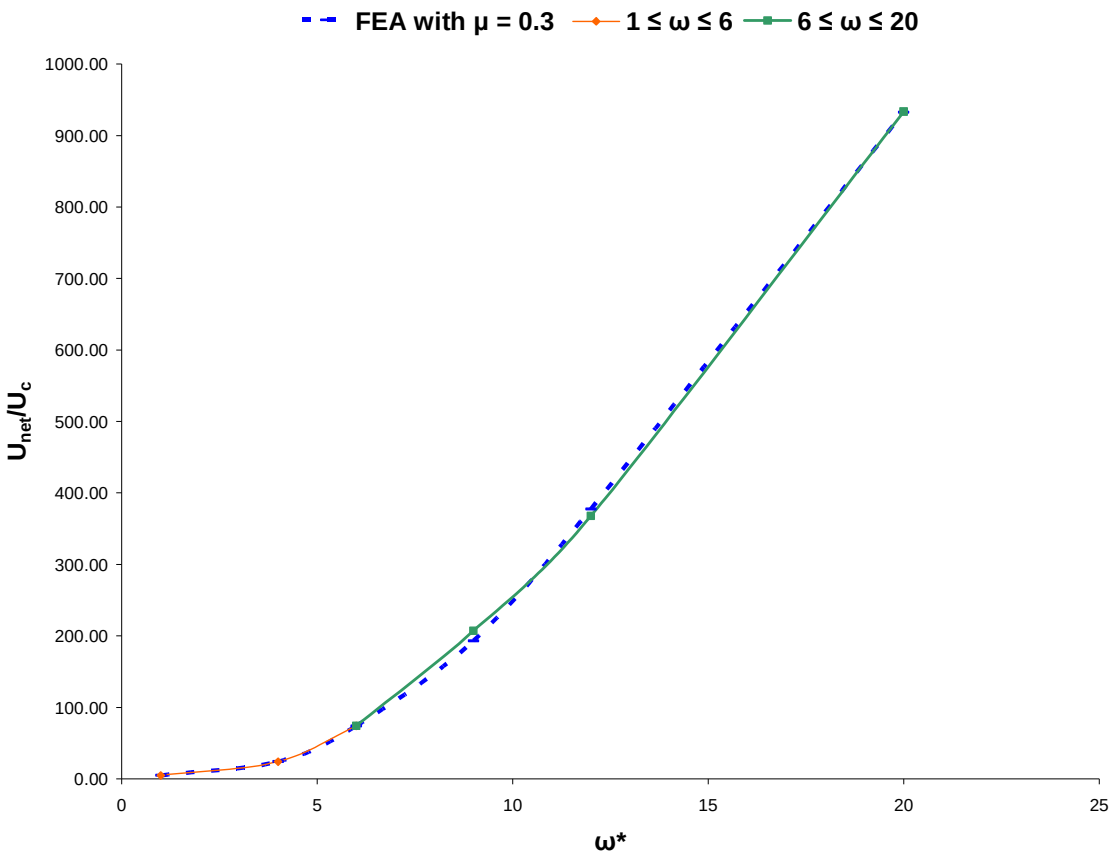

Figure 41: Normalized energy loss vs. normalized vertical interference

4.2.2.5 Contact Half-widths

Figure 42 shows the trend followed by the contact half-width, b, as it changes with each load step as sliding with different vertical interferences progresses. It is normalized by the critical contact half-width, b_c, given in Table 3 and is hence plotted as the ratio b^*. While in the case of steel-steel sliding with friction the contact half-widths are in a symmetric pattern about $x/R = 0$ (see Figure 23), here it is seen that as the vertical interference increases the curves get increasingly skewed towards the left of $x/R = 0$. This is because of the unsymmetrical deformation patterns that develop on the Al and Cu cylinders.

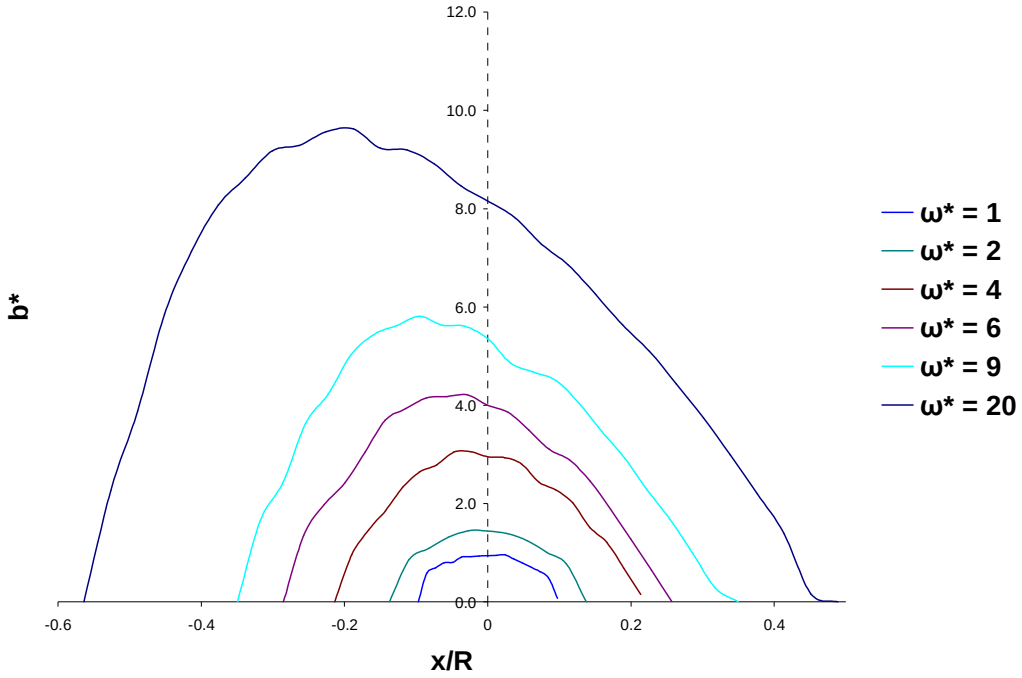

Figure 42: Normalized contact half-width for each load step vs. normalized sliding distance for Al-Cu sliding with friction

4.3 Frictional vs. Frictionless Sliding Comparison

In this section, comparisons are drawn between frictional and frictionless sliding for each of the result parameters that are discussed in the previous sections. This study is carried out for the vertical interference values of $\omega^* = 12$, 15, and 20. This helps in separately analyzing the effect of purely the mechanical process of sliding from the combined effect of frictional and mechanical behavior.

4.3.1 Steel-Steel Comparison

4.3.1.1 Deformations

Figure 43 shows the plot of u_y/ω_c vs. x/R for both the frictionless and frictional steel-steel sliding cases for the highest tested vertical interferences of $\omega^* = 12$, 15, and 20. The peak deformations for $\omega^* = 12$ are about the same, but while for the frictionless sliding case the deformation decreases after reaching the peak, for frictional sliding it increases marginally. For $\omega^* = 15$ and 20, the magnitudes of u_y/ω_c are noticeably higher than those for the frictionless case. For all the cases shown, residual deformation is not captured in the plots for frictional sliding as the cylinders remain in contact even after sliding is completed due to material pile-up. For the frictionless sliding case, the plastic deformations are preserved as can be seen by the flattening of the deformation curves in Figure 43.

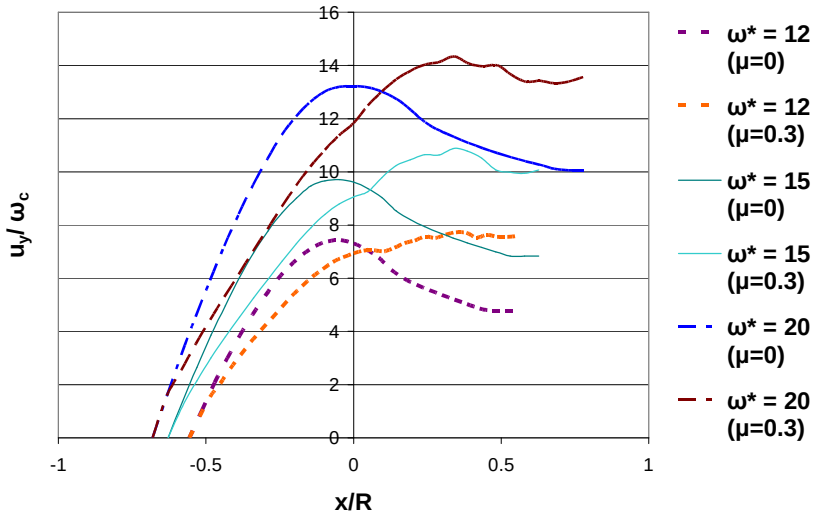

Figure 43: Comparison of normalized maximum deformation plots for steel-steel sliding with and without friction

4.3.1.2 Forces

Figure 44 and Figure 45 show a comparison of the plots of the normalized horizontal force, normalized vertical force, and load ratio for the frictionless and frictional sliding cases. Expectedly, none of the curves that are plotted for the frictional sliding cases show positive values. The peak values for both the frictionless as well as the frictional sliding cases lie before $x/R = 0$. Because of material pile-up in the cases of frictional sliding, the area under the horizontal reaction curve is much larger than that in the frictional sliding cases (see Figure 44). This signifies greater energy loss due to the presence of friction.

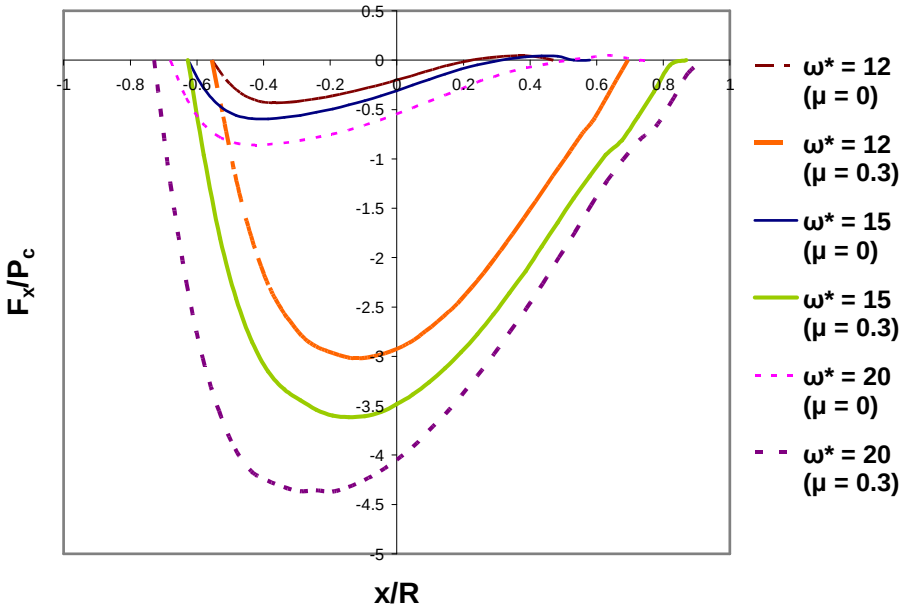

Figure 44: Comparison of normalized horizontal reaction force plots for steel-steel sliding with and without friction

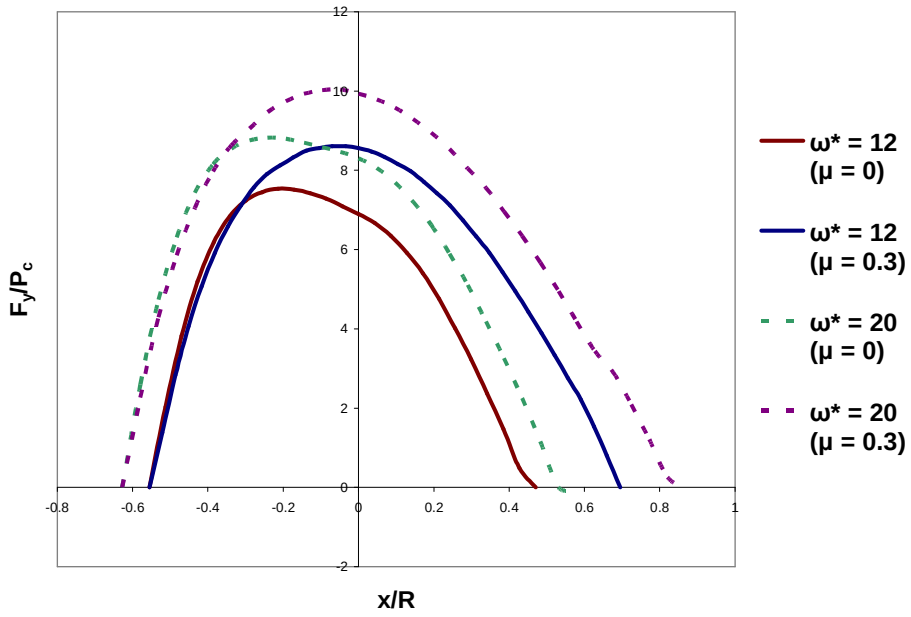

Figure 45: Comparison of normalized vertical force plots for steel-steel sliding with and without friction

4.3.1.3 Stress Formations

Stress formations and residues in sliding are of the highest interest as they help in predicting the region of yield and subsequent failure. For frictionless steel-steel sliding, the von Mises stress contour plots are shown in Figure 10, while Figure 29 captures the development of stresses for frictional sliding between two steel cylinders. The most significant difference in the stress contours of these two cases is the axis of symmetry for the stress pattern. For both frictionless as well as frictional sliding, the stress field in the two sliding steel cylinders is mirrored about the horizontal contact interface (see Figure 10 and Figure 29). However, for frictional sliding the higher stress fields that develop during the course of sliding are tilted towards the normal to the actual plane of contact between the two cylinders. This plays an important role in the progression of yield and diminishment of the elastic core in frictional sliding. Moreover, friction also leads to the

accumulation of stresses at the corners of the two cylinders as seen in Figure 29. As discovered in sections 3.1.4.3 and 4.1.2.3, for high vertical interferences progressively large magnitudes of stresses are found at the base of the cylinders for both frictionless as well as frictional sliding. It is thus reasonable to postulate that for extremely high vertical interference values, these regions with such accumulation of stresses will be the cause of shearing or failure. While in the frictionless sliding case (see Figure 10) such stresses are found to develop equally at both the corners of the base of the cylinders, this is not the case when sliding is simulated in the presence of friction (see Figure 29). For example, at $x/R = 0$ for sliding with a vertical interference of $\omega^* = 15$ the maximum von Mises stress, σ_e, at the base of the bottom cylinder for the frictionless sliding case is found to be 0.453 GPa. On the other hand, for sliding with friction the magnitude of σ_e is 0.715 GPa. This difference holds true for all the vertical interference cases, and the magnitudes of the stresses at the base of the cylinders are always higher for frictional sliding as compared to those for the frictionless sliding cases. It is notable that these stress magnitudes found at the base for both frictionless and frictional sliding are still below the yield strength; hence no yielding has occurred at these locations.

As far as the residual stresses are concerned, it is discovered that the spread is wider on the case of frictionless sliding. This can be observed by comparing Figure 46 and Figure 47, which respectively show the residual von Mises stress distributions for the frictionless and frictional sliding cases for a vertical interference of $\omega^* = 9$. While some of the stresses are found to remain at yield value (i.e., residual plastic strain) for the frictionless sliding case, no such stress magnitudes remain after sliding is completed with friction.

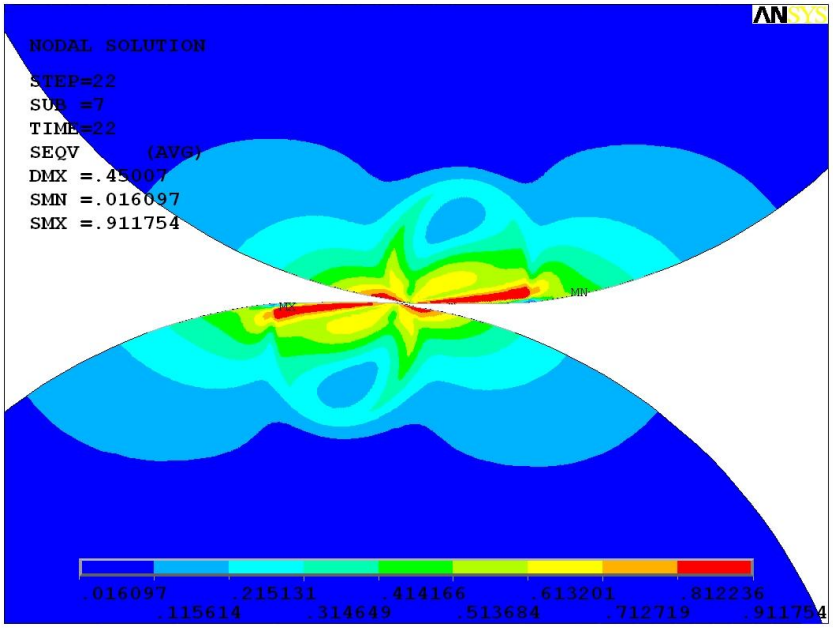

Figure 46: Residual von Mises stress contours for frictionless steel-steel sliding contact for $\omega^* = 9$

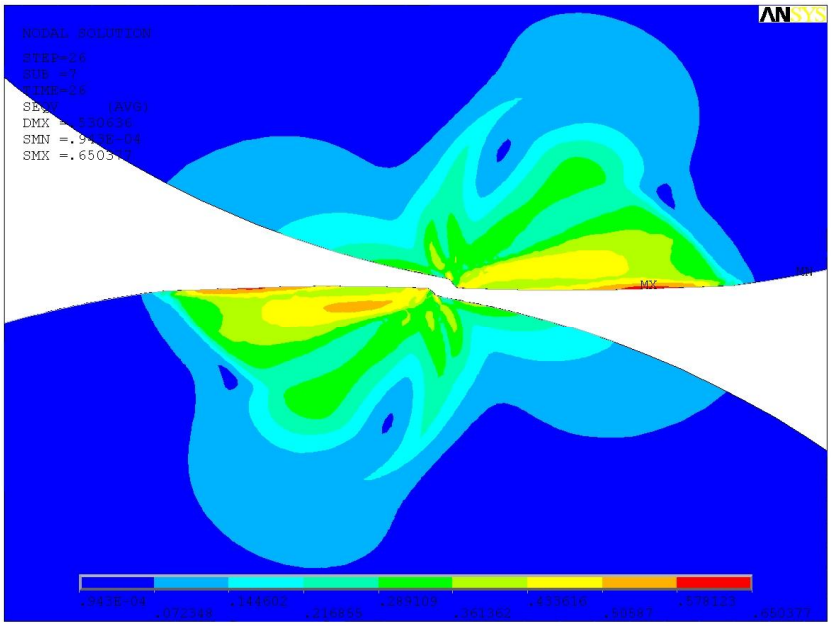

Figure 47: Residual von Mises stress contours for steel-steel sliding contact with friction for $\omega^* = 9$

4.3.1.4 Energy Losses

Figure 48 shows curves representing energy loss due to plasticity in frictionless as well as frictional sliding. It is seen that the magnitudes of energy lost due to plasticity, U_{net}/U_c, are found to be consistently higher in the case of frictional sliding for the various vertical interferences in the elastic-plastic regime. Moreover, these magnitudes are seen to progressively get larger as the vertical interference increases as seen in Figure 48. This observation can be attributed to the occurrence greater plastic deformation in sliding in the presence of friction as compared to sliding without friction. Figure 49 highlights these phenomena.

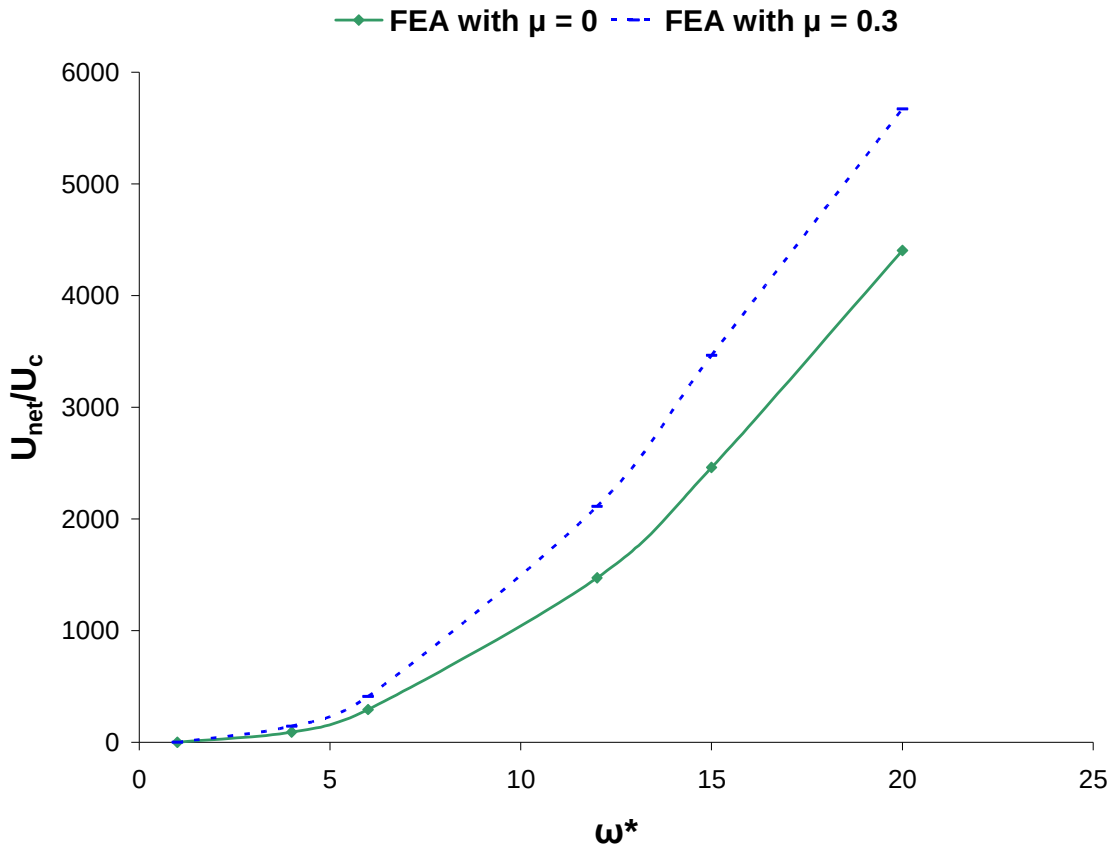

Figure 48: Comparison of energy loss due to plasticity in frictional and frictionless steel-steel sliding

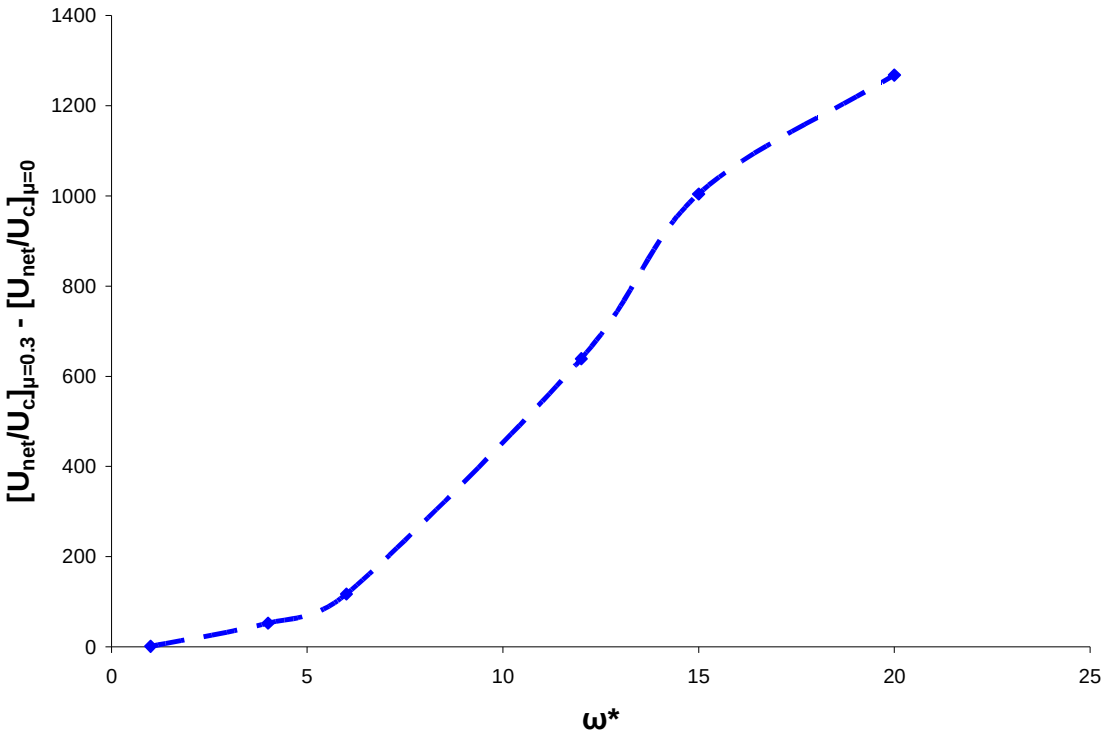

Figure 49: Differences in energy loss due to plasticity between frictional and frictionless sliding

4.3.1.5 Contact half-widths

Figure 50 shows a comparison of the contact half widths, b^*, for $\omega^* = 12$ and $\omega^* = 20$ between frictionless and frictional sliding between two steel cylinders. It is interesting to note that the curves for frictional sliding are more or less symmetric about $x/R = 0$, whereas for frictionless sliding they are skewed towards the left of the vertical axis of alignment. The magnitudes of b^* for frictional sliding are found to be much larger than those for frictionless sliding.

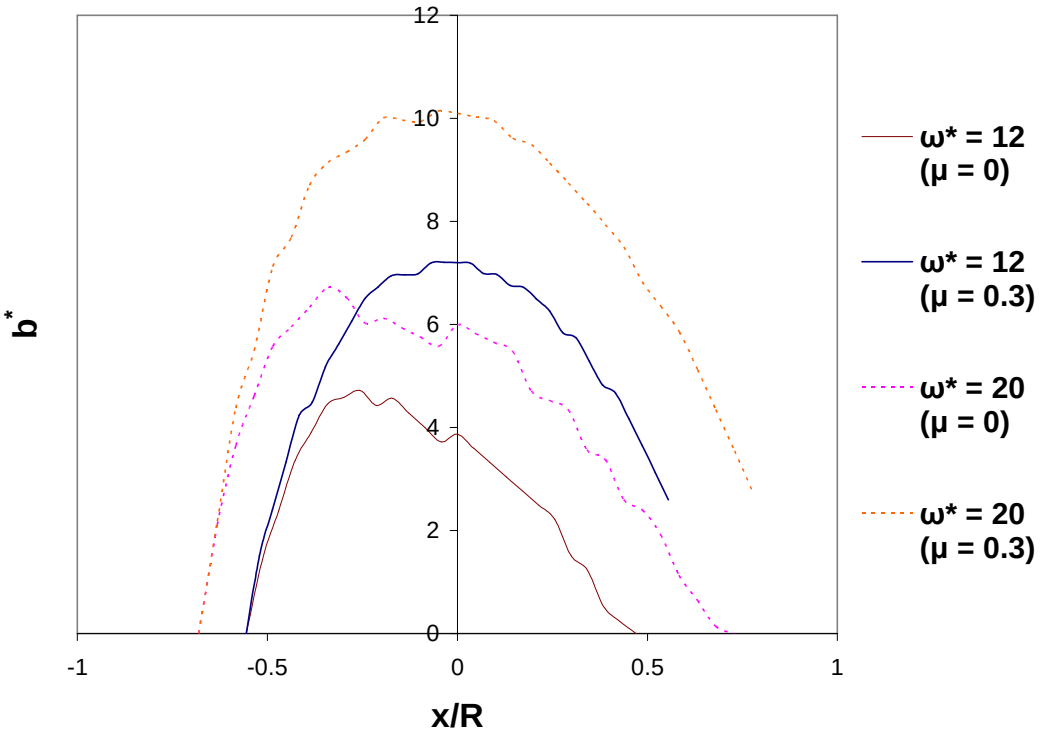

Figure 50: Comparison of normalized contact half-width plots for steel-steel sliding with and without friction

4.3.2 Al-Cu Comparison

4.3.2.1 Deformations

Figure 51 shows the plot of u_y/ω_c vs. x/R in the Al cylinder for both the frictionless and frictional Al-Cu sliding cases for the tested vertical interferences of $\omega^* = 6$, 12, and 20. The peak deformations for $\omega^* = 6$ are about the same, but for $\omega^* = 12$ and 20, the magnitudes of u_y/ω_c for frictional sliding are much higher than those for the frictionless case. This shows that as the vertical interference increases in frictional sliding, the surface deformations in the weaker material (Al) increase progressively due to the presence of friction.

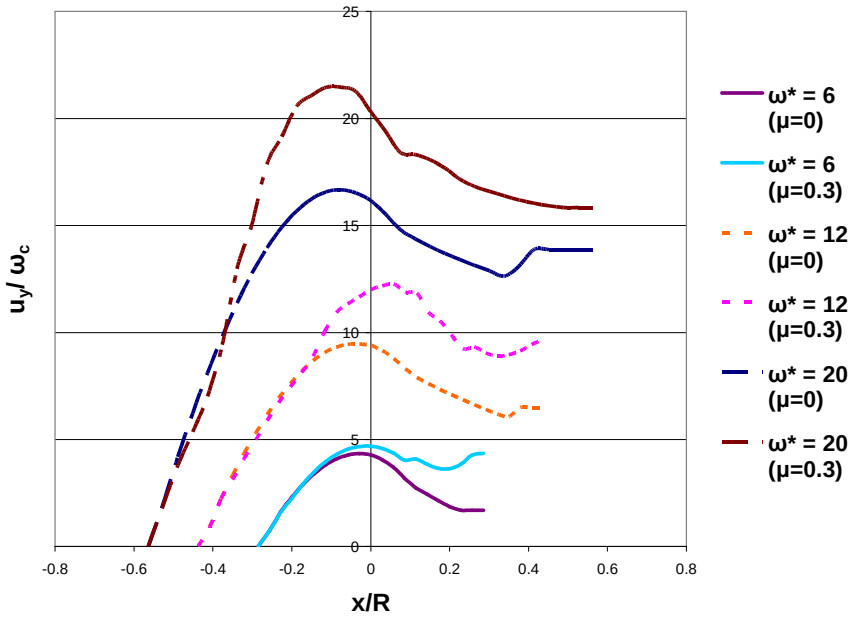

Figure 51: Comparison of normalized maximum deformation plots in the Al cylinder for Al-Cu sliding with and without friction

Deformations in the Cu cylinder are plotted in Figure 52, and are found to be not as large in magnitude as in the Al cylinder for both frictionless and frictional sliding. This is because Cu is a stronger material that Al. Significantly, deformations in the Cu cylinder are much lower in magnitude for frictional sliding as compared to those found in frictional sliding. This gap increases as vertical interference is increased, and can be seen in Figure 52. This trend is completely the opposite of that found in the Al cylinder, where deformations are higher for frictional sliding (see Figure 51). This can be explained by the fact that Cu is a stronger material, and thus does not experience deformations as significant as those found on the Al cylinder. Also, since a displacement boundary condition is employed, the overall vertical displacement of the system is constant. Thus, any additional deformation caused due to friction has to be borne by the weaker material.

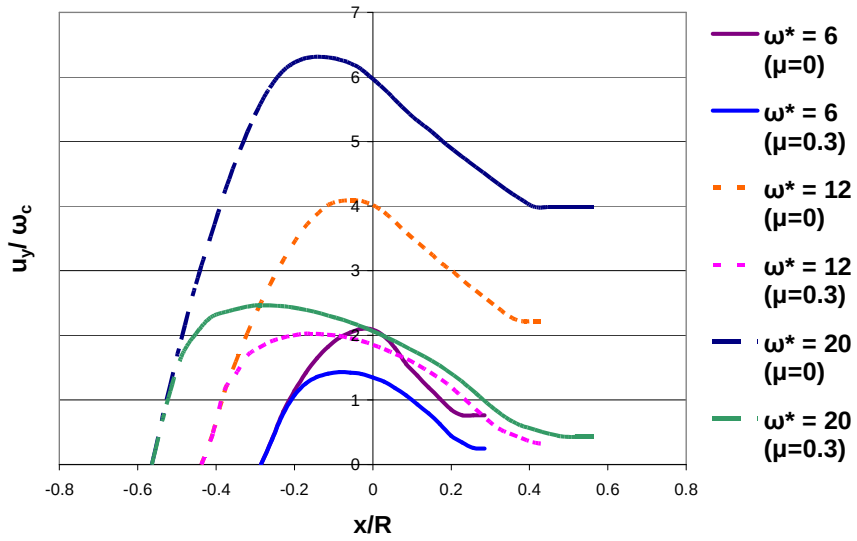

Figure 52: Comparison of normalized maximum deformation plots in the Cu cylinder for Al-Cu sliding with and without friction

4.3.2.2 Forces

Figure 53 and Figure 54 show a comparison of the plots of the normalized horizontal force and normalized vertical force for the frictionless and frictional sliding cases. Expectedly, none of the curves that are plotted for the frictional sliding cases show positive values. The peak values for both the frictionless as well as the frictional sliding cases lie before $x/R = 0$. Because of material pile-up in the cases of frictional sliding, the area under the horizontal reaction curve is much larger than that in the frictional sliding cases (see Figure 44). This signifies greater energy loss in plasticity due to the presence of friction.

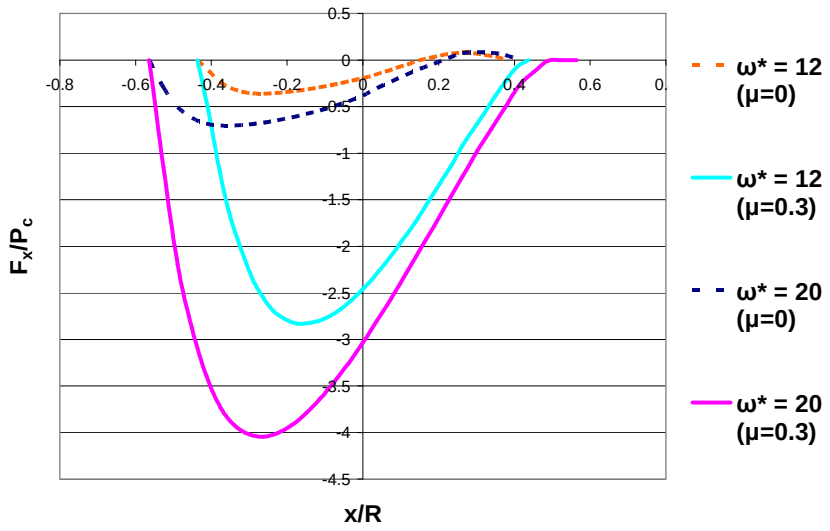

Figure 53: Comparison of normalized horizontal reaction force plots for Al-Cu sliding with and without friction

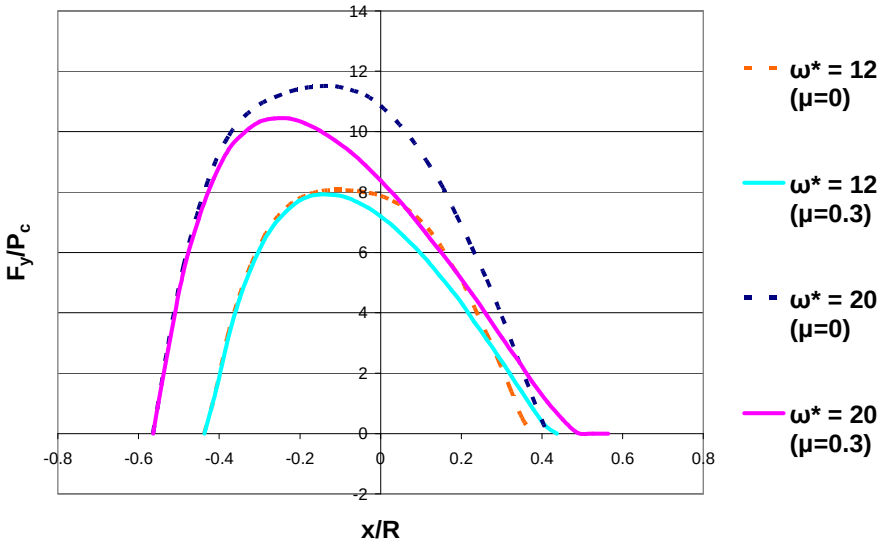

Figure 54: Comparison of normalized horizontal reaction force plots for steel-steel sliding with and without friction

4.3.2.3 Stress Formations

If Figure 19 and Figure 40 are juxtaposed, it is observed that while for high vertical interferences in the frictionless case the stresses are spread more or less evenly in either cylinder, which is not the case for frictional sliding. Due to the presence of friction, the distribution of stresses is skewed in the direction opposite to sliding. Also, stresses in at the base of the cylinders are found to develop only in one corner of the base of the cylinders for the frictionless case as sliding progresses. The magnitudes of these stresses are also higher in frictional sliding. Thus, friction may lead to shearing or failure at the base more rapidly than in the case of frictionless sliding. Figure 55 and Figure 56 show the residual von Mises stress distributions for the frictionless and frictional sliding cases for a vertical interference of $\omega^* = 9$. Stresses are found to be more widely distributed in the Al cylinder for frictional sliding, and the pile-up is visibly heavier than in the frictionless case. On the other hand, the Cu cylinder suffers from even lower stresses than in the frictionless case. Thus, it can be concluded that in sliding with different materials, friction results in a larger deformation of the softer material and this leads to heavier pile-up on the surface of the softer material. This may lead to an earlier failure at the contact interface as compared to the frictionless sliding case.

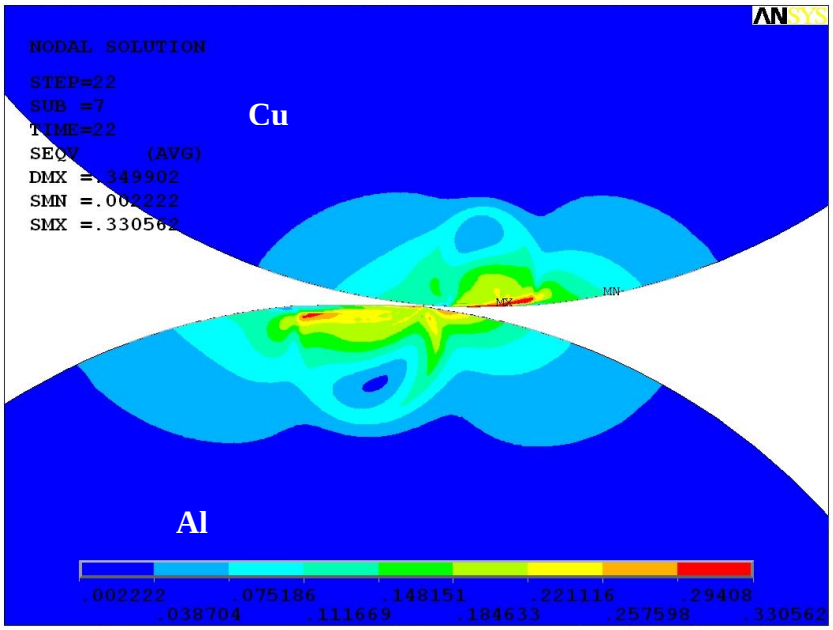

Figure 55: Residual von Mises stress distribution for frictionless Al-Cu sliding with $\omega^* = 9$

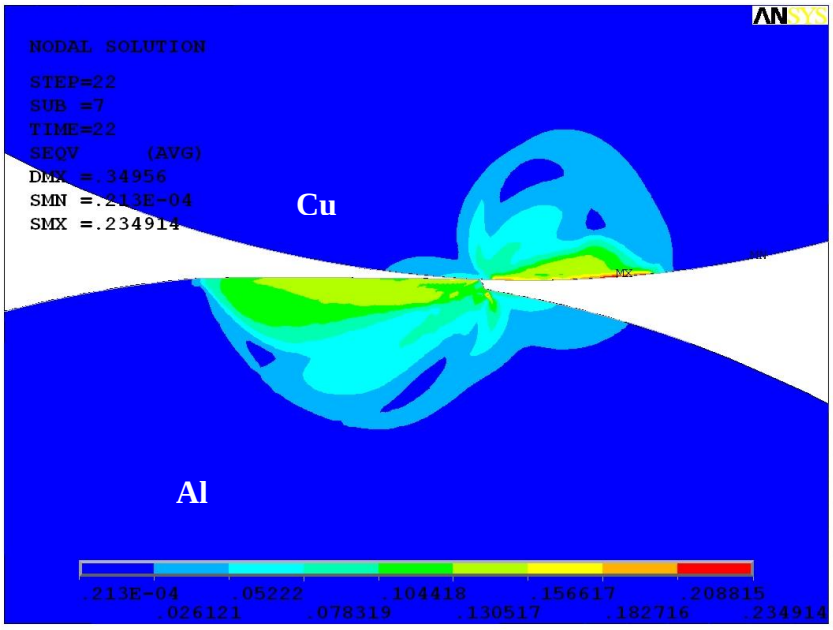

Figure 56: Residual von Mises stress distribution for Al-Cu sliding with friction for $\omega^* = 9$

4.3.2.4 Energy Losses

Figure 57 shows curves representing energy loss due to plasticity in frictionless as well as frictional sliding. It is seen that the magnitudes of energy lost due to plasticity, U_{net}/U_c, are found to be consistently higher in the case of frictional sliding for the various vertical interferences in the elastic-plastic regime. Moreover, these magnitudes are seen to progressively get larger as the vertical interference increases as seen in Figure 57. This observation can be attributed to the occurrence greater plastic deformation in sliding in the presence of friction as compared to sliding without friction. Figure 58 highlights these phenomena.

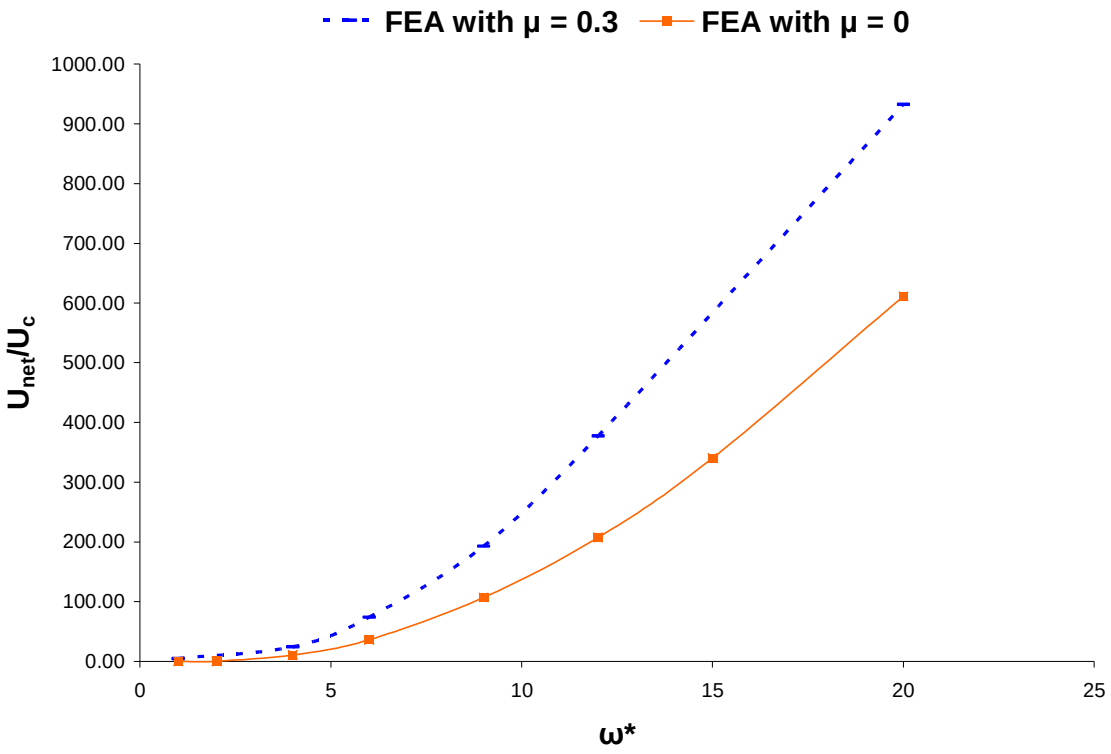

Figure 57: Comparison of energy loss due to plasticity in frictional and frictionless Al-Cu sliding

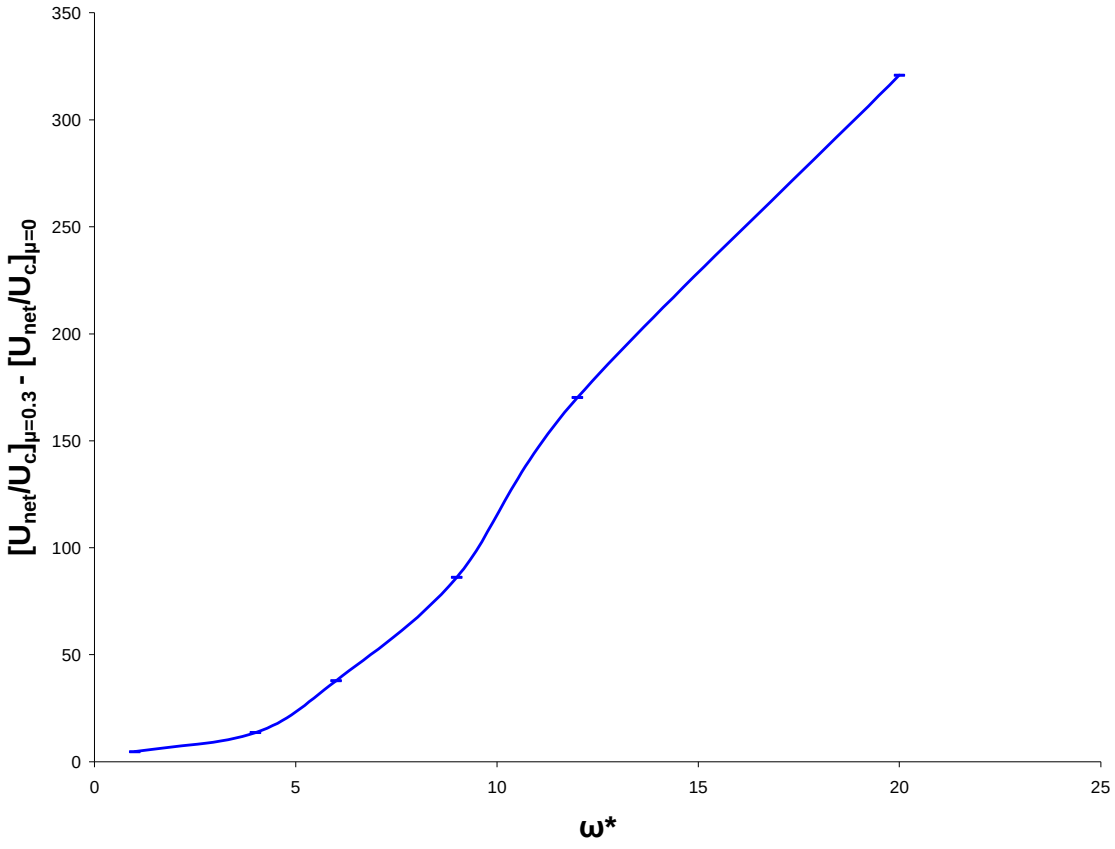

Figure 58: Differences in energy loss due to plasticity between frictional and frictionless Al-Cu sliding

4.3.2.5 Contact half-widths

Figure 59 shows a comparison of the contact half widths, b^*, for $\omega^* = 12$ and $\omega^* = 20$ between frictionless and frictional sliding between Al and Cu cylinders. The magnitudes of b^* for frictional sliding are simply found to be much larger than those for frictionless sliding.

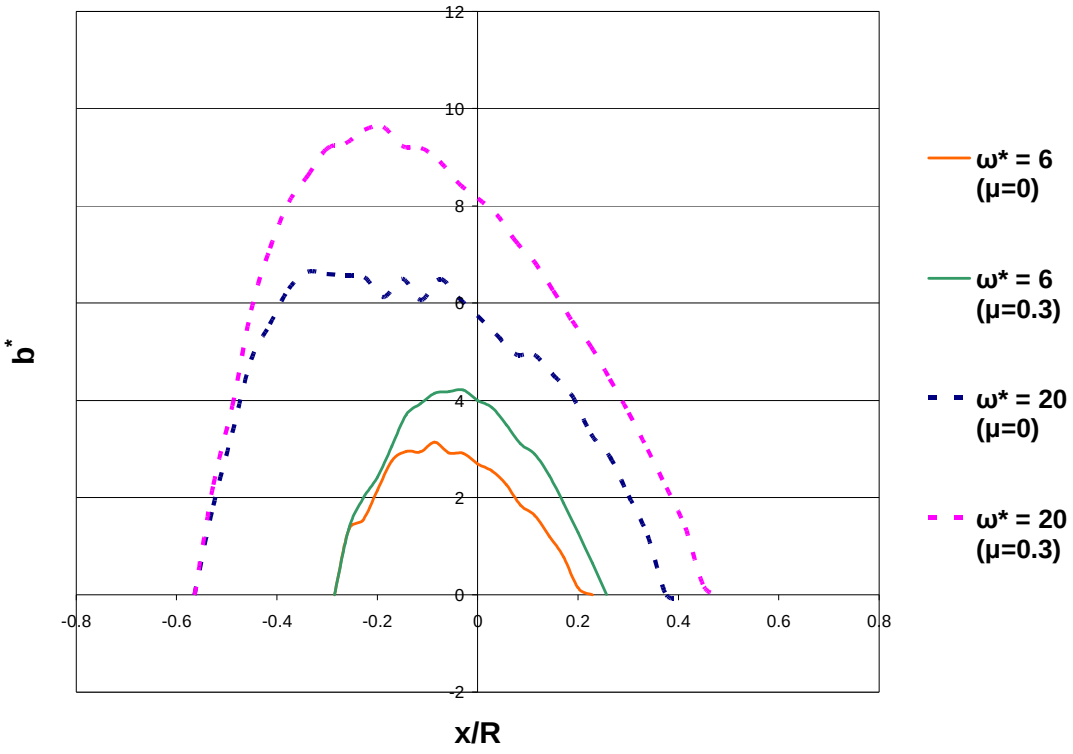

Figure 59: Comparison of normalized contact half-width plots for Al-Cu sliding with and without friction

4.4 Conclusions

It is shown in this section that the behavior of the sliding surfaces in 2D varies significantly with and without the presence of friction. As compared to frictionless sliding, the Al cylinder shows progressively higher vertical deformations on the surface for frictional sliding as the vertical interference is increased. On the other hand, the Cu cylinder shows exactly the opposite trend wherein the deformations are lower for sliding with friction compared to those for frictionless sliding. This shows that friction has a considerable impact on the weaker material for such sliding. This finding is directly

applicable to the EML as it predicts that the Al armature will experience most of the mechanical effects of frictional sliding. On the other hand, the Cu rail will be comparatively unaffected. It is found that the energy losses due to plastic deformation for the same vertical interference are larger in the case of frictional sliding than those that occur in frictionless sliding. The magnitudes of these plastic energy losses are found to be vastly different between steel-steel and Al-Cu sliding for both the frictionless as well as frictional sliding cases. This proves that energy loss due to plasticity is much larger in the stronger material (steel, in this case). Equations capturing all these trends in energy loss are derived and presented. Interestingly, heavier material-pile-ups are found in the frictional steel-steel sliding than in Al-Cu sliding with friction. The horizontal reaction forces are much larger for frictional sliding as compared to frictionless, while the vertical reaction forces show comparable magnitudes. This is due to the fact that the frictional force acts horizontally at the contact interface, and it does not have much effect on the vertical component of the reaction force. The maximum residual stresses in frictional sliding do not reach yield strength magnitudes unlike in the frictionless sliding case. This can be attributed to higher elastic strains in frictionless sliding, which uphold elevated residual stress magnitudes.

Thus, the effects of plasticity and friction have been isolated and separately analyzed to understand the sliding process under elastic-plastic loading in 2D. Now the challenge is to solve the same problem in 3D by means of sliding between hemispherical asperities, so that the overall behavior of rough surfaces can be characterized.

CHAPTER 5: METHODOLOGY FOR 3D ANALYSIS

5.1 Approach and Assumptions

This chapter attempts to lay a foundation for FEA of sliding between two hemispherical asperities in 3D. A rigorous analysis as in the 2D case is prohibited by the large size of the FE model, and the correspondingly huge computational time (~72 hours) that is clocked to run just a single sliding simulation. Two solid hemispheres representing the sliding asperities are modeled and one is made to traverse over the other with a preset vertical interference ω between the two (see Figure 60). Here, sliding is simulated only as a frictionless process, i.e., no coefficient of friction is input in the FE model. Also, repeated sliding is not considered, and hence the top asperity is made to pass over the bottom asperity just once. This is defined as 'one-pass' sliding. Following are the assumptions used to simplify the FE model:

1. Sliding is assumed to be a frictionless process, and hence no coefficient of friction is input in the FE model. This is done in order to isolate the effect of plasticity during sliding that causes elastic-plastic deformation.
2. It is attempted to validate the mesh up to the onset of plasticity by using the Hertzian solution since no closed form solutions are available for this purpose in the elastic-plastic regime. It is assumed that such a mesh is also robust for analysis in the elastic-plastic regime.
3. Deformations in the bulk area are assumed not to have a significant bearing on the effects of sliding in the contact region.

The approach used in this work to simulate sliding contact involves the application of displacement boundary conditions to facilitate interference sliding. This approach also results in a rapid convergence of the solution as compared to the boundary condition where forces are applied instead of displacements. The material of the asperities is assumed elastic-perfectly plastic with identical behavior in tension and compression. Throughout this discussion, the Y-axis corresponds to the vertical direction, the X-axis to the horizontal, and the Z-axis to the out-of-plane direction (see Figure 60).

In the elastic domain and up to the onset of plasticity, the Hertzian solution [27] provides critical values of load, contact half-width, and strain energy. As explained by Jackson et al [29], hardness is not implemented as a unique material property as it varies with the deformation itself as well as with other material properties such as yield strength, Poisson's ratio, and the elastic modulus. Instead, the critical vertical interference, ω_c, as derived by Green [28] for hemispherical contact, is employed. This quantity is derived by using the distortion energy yield criterion at the site of maximum von Mises stress by comparing the stress value with the yield strength, S_y. The critical values of force, half contact width, and interference are given in [28] (See Appendix for a brief summary of the terms):

$$P_c = \frac{(\pi C S_y)^3 \mathrm{R}^2}{6E'^2} \;;\; b_c = \frac{\pi C S_y R}{2E'} \;;\; \omega_c = \left(\frac{CS_y}{2E'}\right)^2 R \tag{12}$$

$$p_o = \frac{3P}{2\pi a^2} = \frac{1}{\pi}\left[6P\left(\frac{E'}{R}\right)^2\right]^{1/3} \tag{13}$$

$$\frac{\sigma_e}{p_o} = \frac{1}{2}\sqrt{\frac{((1-2\nu-2\zeta^2(1+\nu)+2(\zeta+\zeta^3)(1+\nu)ArcCot[\zeta])^2}{(1+\zeta^2)^2}} \tag{14}$$

Where:

$$\frac{1}{R} = \frac{1}{R_1} + \frac{1}{R_2}$$

$$\frac{1}{E'} = \frac{1-\nu_1^2}{E_1} + \frac{1-\nu_2^2}{E_2}$$

$$\zeta_m = 0.38167 + 0.33136\nu \tag{15}$$

$$C = 1.30075 + 0.87825\nu + 0.54373\nu^2 \tag{16}$$

The value of *C* is obtained from elasticity considerations, and the critical parameters are obtained at the point of yielding onset. The maximum elastic energy that can possibly be stored (up to the point of yielding onset) is used to normalize the net energy loss due to plastic deformation after sliding, and is given by Green [28] as:

$$U_c = \frac{\pi\left(CS_y\right)^5 R^3}{60E'^4} \tag{17}$$

The critical values are calculated for a steel material with properties as follows: $\mathrm{E}_1 = \mathrm{E}_2 = 200\,\mathrm{GPa}$, $\nu_1 = \nu_2 = 0.32$, and $S_y = 0.9115\,\mathrm{GPa}$. These values are shown in Table 3. Since all the quantities are subsequently being normalized by the critical parameters in Equation (12), the ensuing results apply for any geometry scale (as long as homogeneous and isotropic continuum mechanics prevails); therefore, the radii for the

asperities in the FE model are subjectively (and conveniently) chosen to be $R_1 = R_2 = 1m$.

Table 4: Critical values of parameters at the onset of plasticity for sliding between two Hemispherical asperities

Parameter	Value
C	1.637
CS_y	1.493 GPa
ω_c	0.22143 mm
P_c	0.346 MN
b_c	0.0105 m
U_c	30.65 kN m

5.2 Geometry, Meshing, and Boundary Conditions

As shown in Figure 60, the nodes at the base of the bottom asperity are constrained from displacement in the X, Y and Z directions. The nodes at the base of the top cylinder are also constrained from displacement in the Y and Z directions, but are allowed to displace freely in the X direction upon sliding. Noteworthy, the computational cost is considerably smaller when using the boundary conditions where displacement is applied to only one of the cylinders as opposed to sliding both asperities. Sliding is performed for $\omega^* = 6$, which is in the elastic-plastic loading regime. Δx is as defined in Figure 3.

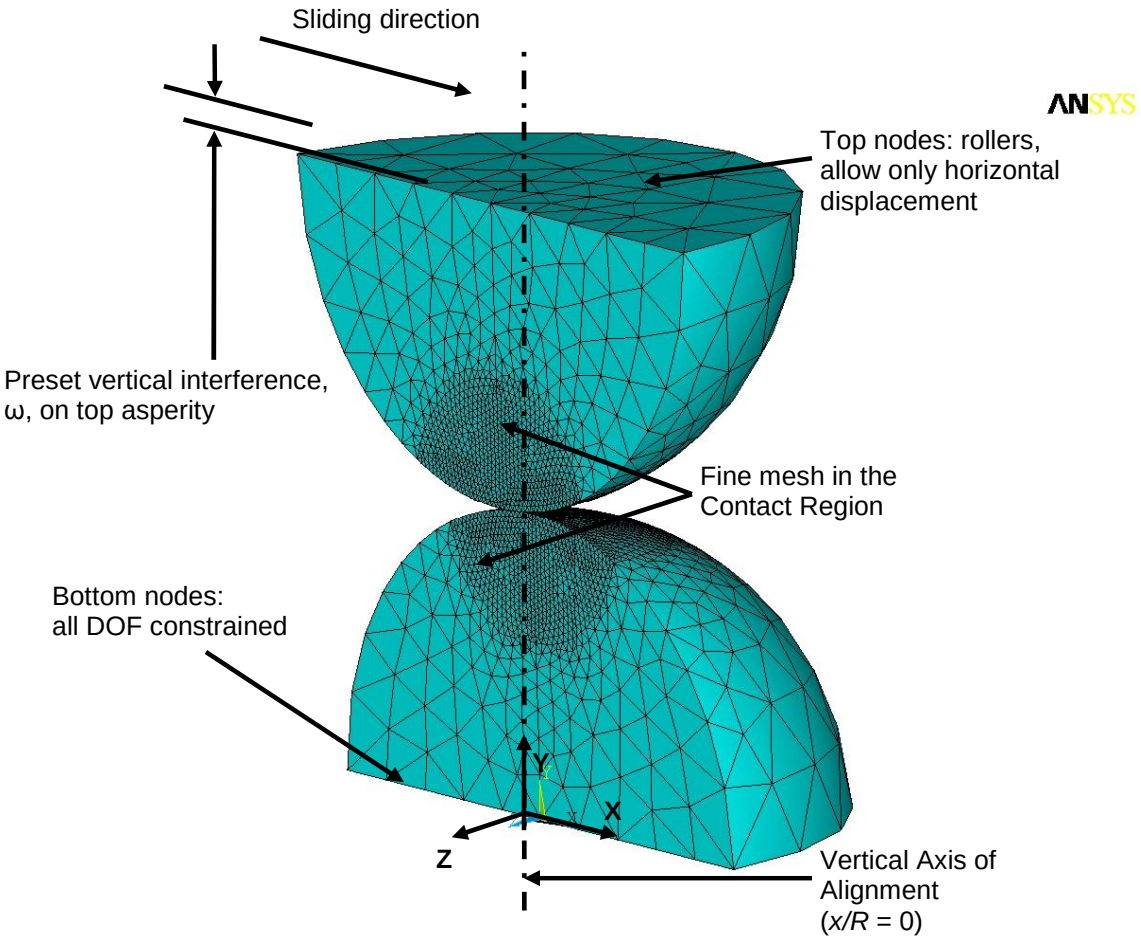

Figure 60: Schematic of the FEA for sliding between hemispherical asperities

To establish confidence in the mesh for the elastic-plastic loading regime, a 3D FEA simulation for the critical vertical interference of $\omega = \omega_c$ or $\omega^* = 1$ is performed wherein the top asperity is vertically pressed on the bottom asperity. As in the 2D model verifications, these results are then compared against the Hertzian solution. This is termed as normal loading of the hemispherical asperities. The meshing for this simulation is similar in approach to that employed by Jackson and Green [20]. However, instead of a representative model consisting of quarter-circle and a rigid flat as in [20], contact in this case is between two actual hemispheres representing the two asperities. In addition, the contact region is encapsulated by a semi-hemispherical region as shown in Figure 60. The mesh is symmetric about the vertical axes of the hemispheres.

The commercial FEA software ANSYS® is used to perform the analyses. The mesh is constructed using ten node tetrahedral elements (Solid 92 in ANSYS) and surface-to-surface contact elements (Contact 174 and Target 170 in ANSYS). A symmetric contact pair, i.e., one wherein either surface has a layer of contact as well as target elements, is defined. This ensures robustness of the contact model. Once the predetermined regions are established, ANSYS is used to automatically mesh the said regions. Since the problem is non-linear, small load steps are used toward incremental (quasi-static) sliding from one end to the other. Various mesh schemes are tried to achieve convergence. The optimized model has 108618 nodes, 75112 elements, and thousands of contact elements in the region of interest (see front view of the zoomed contact region in Figure 61).

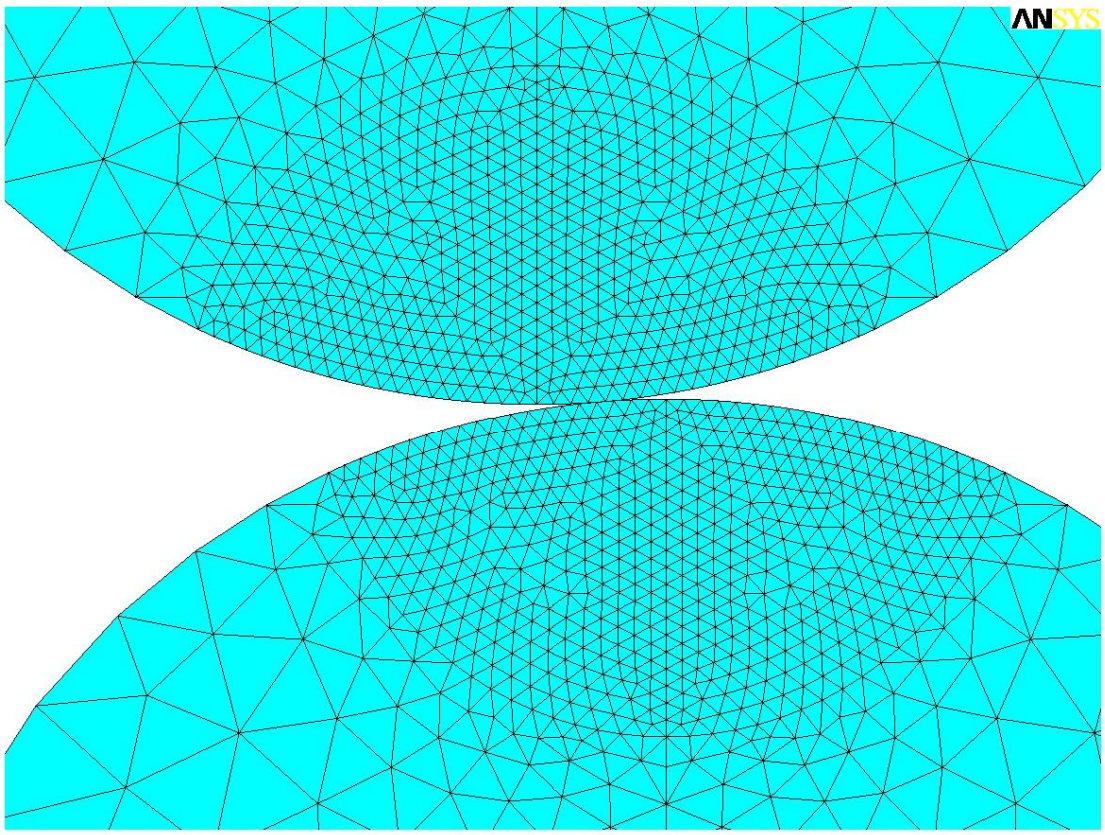

Figure 61: Description of the meshing scheme employed for 3D sliding hemispherical contact

5.3 Comparison of Theoretical and FEA results

The mesh is tested first under non-sliding normal elastic contact, against the empirical solutions obtained by Green [28]. In the FEA model the value of critical vertical interference, ω_c, is imposed and the maximum von Mises stress, σ_e, and the sum of the vertical reaction forces, P_c, are extracted. Corresponding to the imposed interference of $\omega = \omega_c$, the values of σ_e and P_c are as shown in Table 5. The values obtained from the FEA are compared with the theoretical values thus calculated at critical vertical interference. This comparison is shown in Table 5.

Table 5: Comparison of theoretical and FEA values for normal loading with $\omega^* = 1$

ω^*	P_c (theoretical)	P_c (FEA)	%error	σ_e (theoretical)	σ_e (FEA)	%error
1	0.000346	0.0000912	73.64	0.9115	0.3289	63.92

The large errors seen in the critical values obtained from the FEA are due to insufficient mesh refinement performed on the FE model. The university version of the FE software, ANSYS®, available for this study has a limitation on the number of nodes (maximum 128,000) that can be generated to mesh any geometry. As mentioned earlier, the current model has a total of 108618 nodes. This is the highest level of optimization that could be achieved after taking into account factors such as essential higher mesh density in the contact region and gradual coarsening of the mesh into the bulk of the asperity. Moreover, elemental errors such as disproportional shapes and unacceptable aspect ratios have to be encountered while meshing such a large model. Thereafter, during the solution phase some elements undergo excessive plastic deformation during such loading and this leads to distortion and subsequent convergence problems. The Augmented Lagrangian algorithm is utilized since it is found to be the best suited to solve this sliding contact problem.

5.4 Results and Discussion for Sliding in the Elastic-Plastic Regime

The results are presented for a preset normalized vertical interference of $\omega = 1$. The material properties used for the asperities are chosen to be steel, the properties of which are described in section 3.1.1. The computation time is about 72 hours on a dual

processor Xeon *3* GHz PC with hyperthreading turned on to utilize four virtual processors.

The vertical deformation pattern followed by the hemispheres is captured in Figure 62.

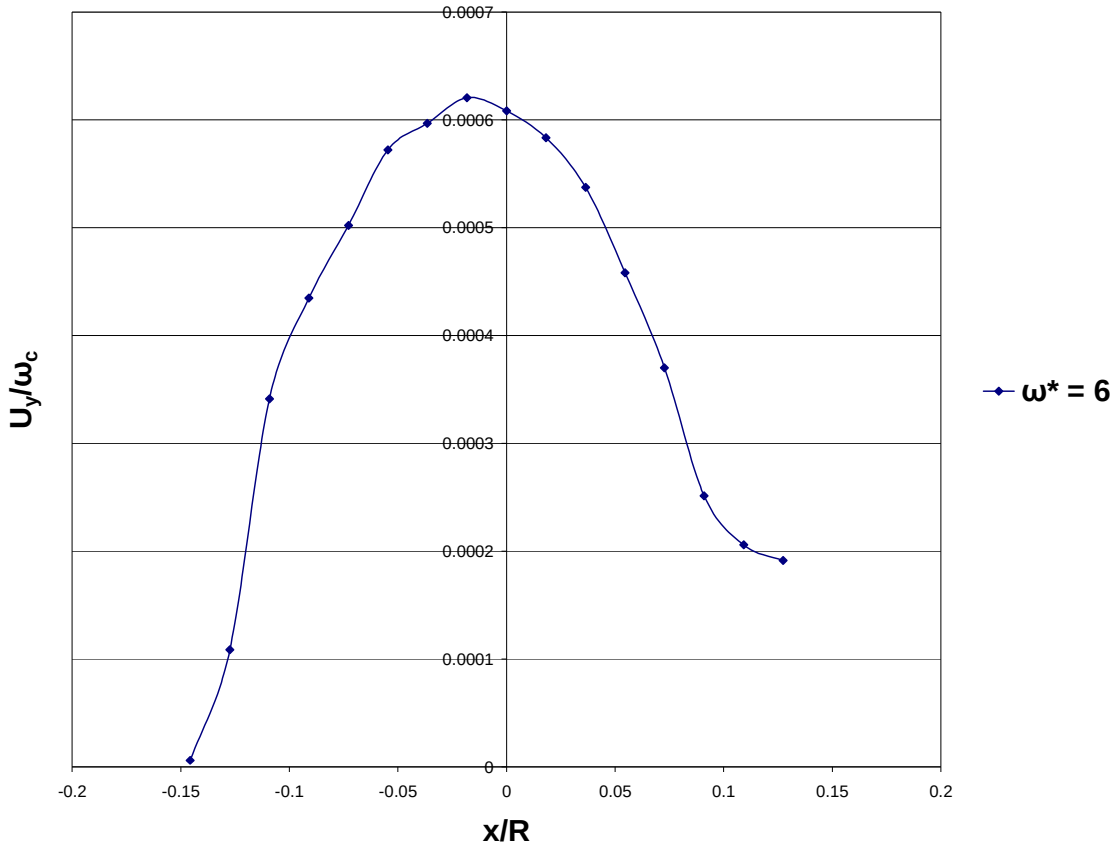

Figure 62: Normalized maximum vertical displacement vs. normalized sliding distance for frictionless sliding between hemispherical asperities

Results from work by Vincent et al. [30] are used to compare the reaction force patterns obtained through the FEA. Figure 63 and Figure 64 respectively show the FEA plots of the horizontal and vertical reaction forces compared with those obtained from

[30]. It is clear that in consistence with the validation results in Table 5, the results are off by a large magnitude, but are still comparable in trend to those found in [30]. Further refinement of the mesh in the contact region is expected to yield results closer to those expected.

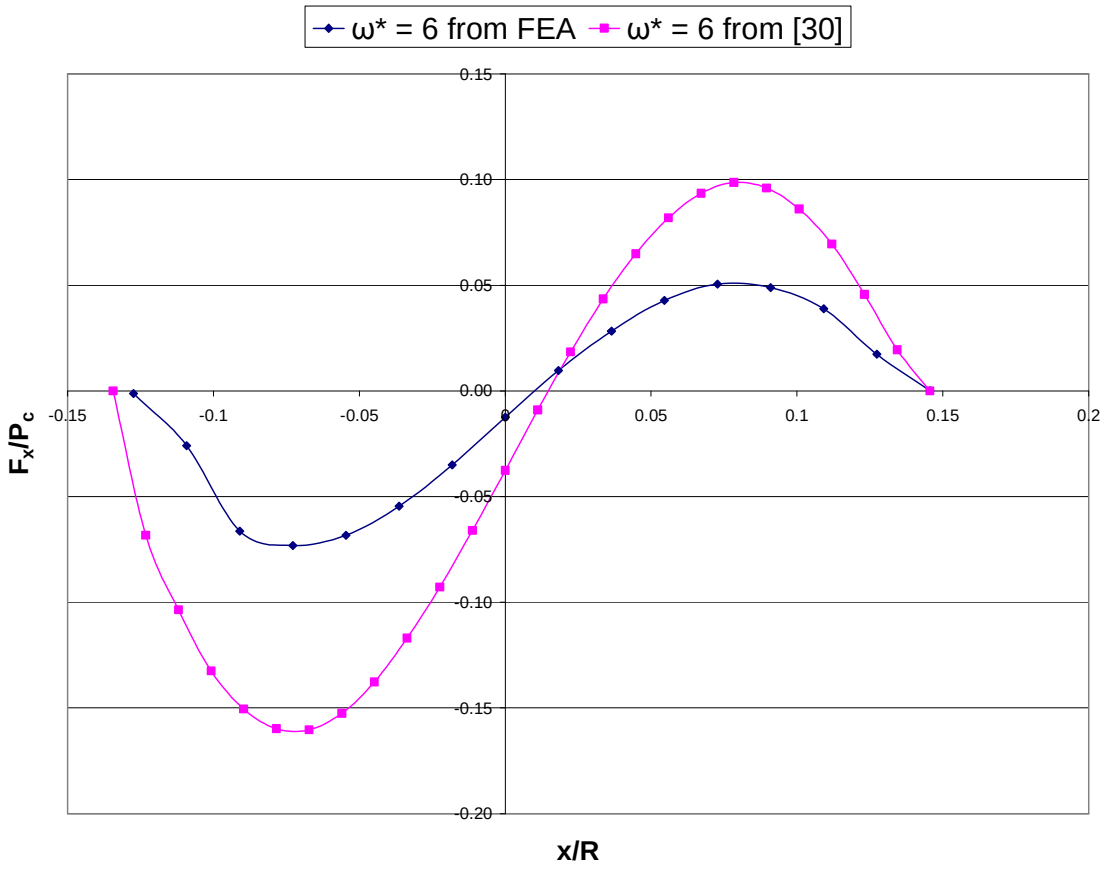

Figure 63: Normalized horizontal reaction force vs. normalized sliding distance for frictionless sliding between hemispherical asperities

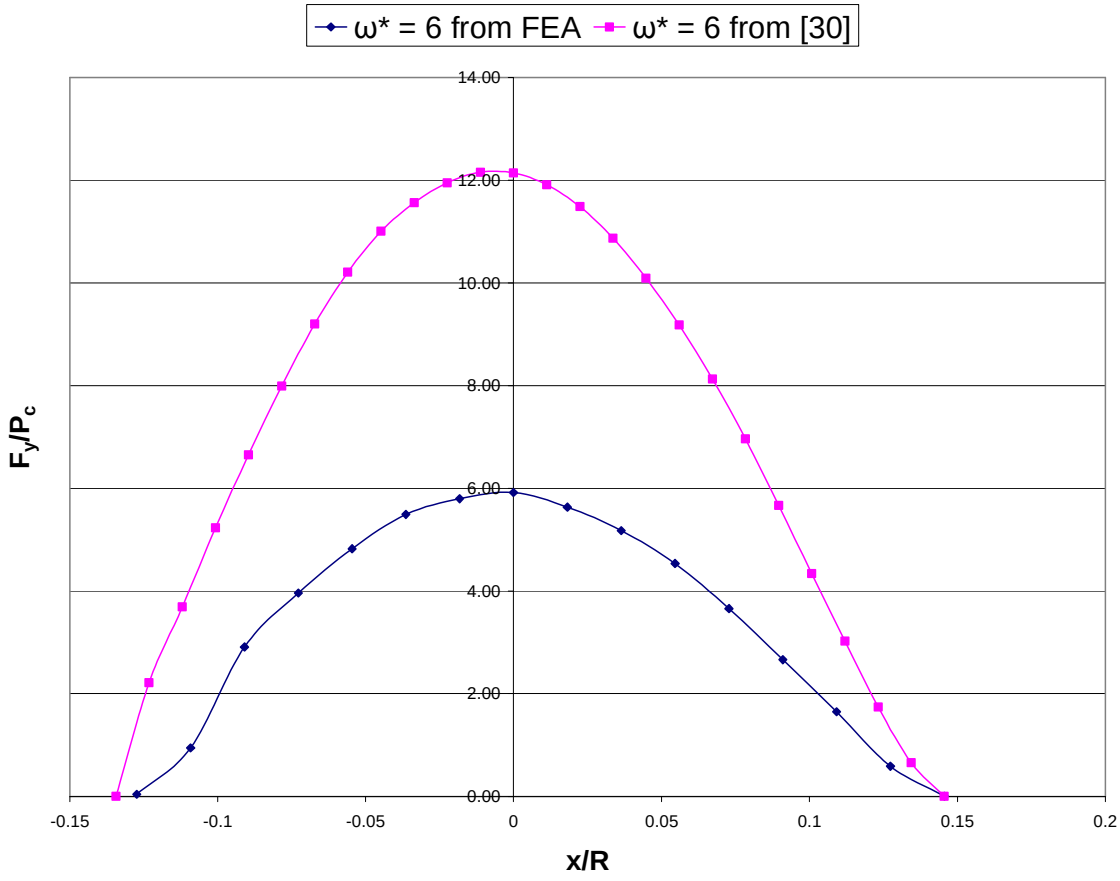

Figure 64: Normalized vertical reaction force vs. normalized sliding distance for frictionless sliding between hemispherical asperities

Since optimal mesh refinement could not be achieved, the plots shown in this section are only for the purpose of understanding the general trends followed by the sliding asperities under elasto-plastic loading. The magnitudes of the various parameters in these plots are thus not true, and can only be confidently determined once rigorous mesh validation and convergence studies are performed.

von Mises stress contours at $x/R = 0$, i.e., the vertical axis of alignment are shown in Figure 65, while Figure 66 shows the residual stress contours for hemispherical sliding at a vertical interference of $\omega = 6$.

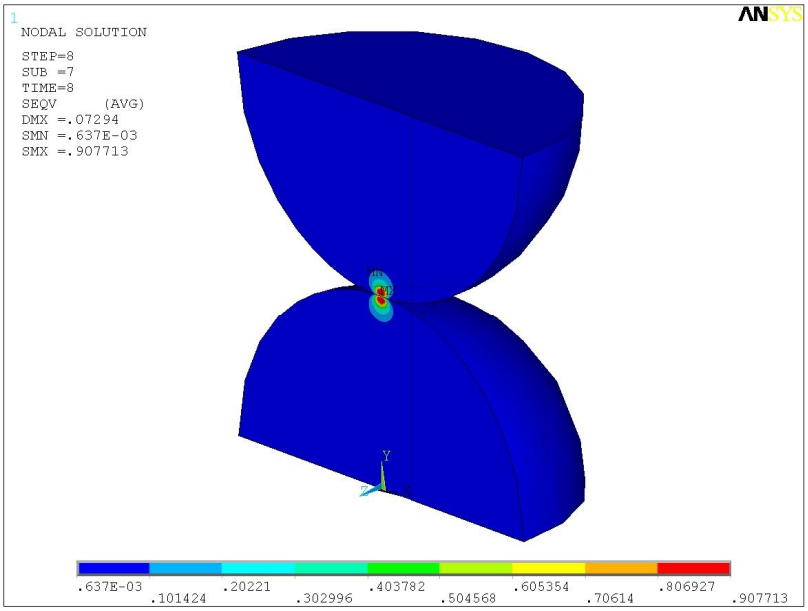

Figure 65: von Mises stress distribution at *x/R*=0 for frictionless sliding between hemispherical asperities

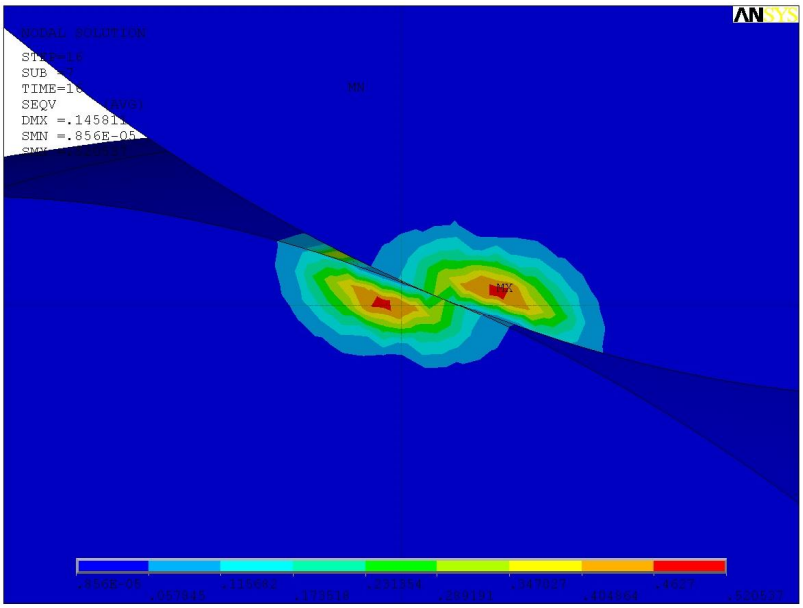

Figure 66: Residual von Mises stress distribution for frictionless sliding between hemispherical asperities

CHAPTER 6: CONCLUSIONS

This work presents the results of Finite Element Analyses (FEA) used to simulate sliding in two (2D) and three dimensions (3D) between two interfering elasto-plastic bodies. Cylinders are used to model sliding contact in 2D, simplified by the assumption of plane strain. Sliding is studied between two cylinders modeled with material properties of steel, and separately with a Glidcop cylinder sliding over an Al 6061-T651 cylinder. All materials are modeled as elastic-perfectly plastic and follow the von Mises yield criterion. Both frictionless as well as frictional sliding are analyzed. A coefficient of friction of magnitude 0.3 is introduced between the two surfaces to simulate frictional sliding.

It is established through this work that for 2D sliding of steel cylinders with material properties as shown in section 3.1.1, the normalized maximum vertical deformations, u_y / ω_c, show a similar pattern for a range of applied vertical interferences in the elastic-plastic domain. Using the 2D steel-steel sliding model as a benchmark, similar trends are discovered for sliding between the Al 6061-T651 (Al) and Glidcop (Cu) cylinders. The properties corresponding to these materials are cited in section 3.2.1. The residual deformations that remain after sliding show a trend that is also represented by empirical equations for all the above sliding cases. The reaction forces and the load ratio show trends that are related to the applied vertical interference. Upon comparison, it is found that the horizontal reactions are much lower for sliding with friction as compared to those found in frictionless sliding. Interestingly, there is not much difference between

the patterns of the vertical reactions of the two cases. By calculating the areas under the horizontal reaction force curves for a range of vertical interferences, equations are derived to capture the energy loss due to plastic deformation in such sliding. It is discovered that there is greater energy loss due to plasticity in frictional sliding than in frictionless sliding. This is true for both – sliding between similar (steel-steel) and dissimilar (Al-Cu) materials. For both frictional and frictionless sliding, steel-steel sliding shows energy losses due to plasticity as much as an order of magnitude higher as compared to those found in the Al-Cu case. Moreover, significant pile-up is found in the steel cylinders for frictional sliding for high vertical interferences, whereas the pile-ups found in the steel cylinders after frictionless sliding for the same vertical interferences are not as pronounced. For Al-Cu sliding, larger and more widely spread stresses are found in the Al cylinder. The Al cylinder is of particular interest as it is the weaker material and hence experiences relatively more plasticity. Notably, the deformations for the Al cylinder do not settle down even after sliding is completed because of material pile-up near the region of contact. The Al cylinder is seen to flatten out as the Cu cylinder plows through it while not showing much pile-up itself. Similar behavior can be expected for 3D simulations that would represent the actual asperities sliding in the EML set-up. Thus, the armature can be predicted to bear most of the mechanical effects of sliding. Negligible material pile-up is found in the Cu cylinder for both frictionless and frictional sliding. The surface deformations of the weaker material (Al) are higher in the frictional sliding case and increase as the applied vertical interference is increased. On the other hand, the stronger material (Cu) experiences a reverse trend and the deformations are found to be lower in frictional sliding than those in frictionless sliding. Additionally, the

Al cylinder shows considerable material pile-up, more so for frictional sliding. Surprisingly, the pile-ups observed in the Al cylinder are not as pronounced as those seen in the case of the frictional sliding of steel cylinders. Still, most of the consequences of plastic deformation due to sliding under high vertical interferences are observed on the Al cylinder for Al-Cu sliding.

It is found that for lower ranges of elasto-plastic loading, the maximum von Mises stresses arise in the region surrounding the contact interface for all cases of sliding. However, as higher vertical interferences are applied, the plastic region propagates towards the contact region and higher stresses are found to develop at the base of the cylinders. It is thus postulated that failure would occur in this region for extremely high vertical interferences even though the contact region may still yield first. This phenomenon is observed in both 2D frictional and frictionless sliding between cylinders of similar or dissimilar materials. The occurrence of such failure would be accelerated due to the presence of friction. Stress formations are symmetric the vertical axis of alignment for steel-steel sliding for both the frictionless as well as frictional sliding. A significant observation is that while some of the residual stresses are found to be at the yield value for frictionless sliding with high vertical interferences, for frictional sliding these stresses do not quite reach the same magnitudes.

The 3D FE model for frictionless sliding between two steel hemispherical asperities is developed and preliminary results are documented. The trends shown for loading in the elasto-plastic regime by the horizontal and vertical reaction forces are found to be similar to those seen in the 2D sliding cases. The exercise is computationally very intensive, and the need for a more refined mesh for thorough validation and

convergence studies is underlined. The current model is optimized to the best possible level given the FE and computational limitations, and could serve as the base for detailed FEA of sliding in 3D.

APPENDIX: THEORETICAL BACKGROUND

Critical Values for Spherical Contact (3D)

This is only a concise summary of the analysis by Green [28], and the nomenclature and references herein are consistent with that work. Let the *x* and *y* axes reside in the circular area of contact between the two spheres, and the *z* axis is the coordinate into the spheres. The maximum (and principal) stresses occur at *x=y=0*. Under the total load, *P*, the maximum pressure is generated at the origin (Johnson [2])

$$p_o = \frac{3P}{2\pi a^2} = \frac{1}{\pi}\left[6P\left(\frac{E'}{R}\right)^2\right]^{1/3} \tag{4}$$

where the Hertzian contact radius is given by:

$$a = \left(\frac{3PR}{4E'}\right)^{1/3} \tag{5}$$

and the deflection is given by Eq. (1). Defining $\zeta = |z/a|$, then the stresses for the spherical contact, as given by Shigley [8], are

$$\sigma_x = \sigma_y = \left(\frac{1}{2(1+\zeta^2)} - (1+\nu)\left(1 - \zeta\, ArcTan\left[\frac{1}{\zeta}\right]\right)\right) p_o \tag{6}$$

$$\sigma_z = -\frac{p_0}{1+\zeta^2} \tag{7}$$

These stresses are calculated in either material 1 or 2, permitting obviously only $\zeta \geq 0$ in both materials. While Φ_z is independent of Poisson's ratio, Φ_x and Φ_y are both dependent upon it. While the theoretical limit of Poisson's ratio is between $-1 < \nu \leq 1/2$, it is rare to

encounter engineering materials with negative Poisson ratios. Most materials will fall in the range $0 \le \nu \le 1/2$ and the discussion herein is limited to this range.

Based upon Eqs. (6, 7) the von Mises stress, σ_e, normalized by the contact pressure, p_o, is calculated by:

$$\frac{\sigma_e}{p_o} = \frac{1}{2}\sqrt{\frac{((1-2\nu-2\zeta^2(1+\nu)+2(\zeta+\zeta^3)(1+\nu)ArcCot\left[\zeta\right])^2}{(1+\zeta^2)^2}} \tag{8}$$

The above varies with ζ where ν is a parameter. A plot of this ratio is given in Fig. 2. Notably there is a single stationary point that resides inside the material signifying the point of greatest distress. The maximum von Mises stress is obtained by letting $d(\sigma_e / p_o)/d\zeta = 0$. Applying that to Eq. (8) and considering just the numerator gives,

$$\begin{aligned}&\left(-\zeta(4+\nu+^2(1+\nu))+(1+\zeta^2)^2(1+\nu)ArcCot\left[\zeta\right]\right)\\ &\qquad\left(1-2\nu-2\zeta^2(1+\nu)+2(\zeta+\zeta^3(1+\nu)ArcCot\left[\zeta\right]\right)=0\end{aligned} \tag{9}$$

This transcendental equation is solved numerically for ζ_m where ν as a parameter is varied in the aforementioned range. The solution is curve fitted, giving the location of maximum von Mises stress at

$$\zeta_m = 0.38167 + 0.33136\nu \tag{10}$$

The numerical values of ζ_m (not the curve fitted ones) are substituted back into Eq. (8) for finding the maximum value of σ_e / p_o. Defining its reciprocal, $C = p_o / \sigma_{e-\max}$, results clearly in $C = C(\nu)$. A curve fit procedure gives

$$C = 1.30075 + 0.87825\nu + 0.54373\nu^2 \tag{11}$$

with almost indistinguishable error, where ν is the Poisson ratio of either material (i.e., it is either ν_1, or ν_2). The true interpretation of C is that it represents the ratio between the maximum contact pressure and the maximum von Mises stress. At yielding p_o takes on the critical value p_{oc}, and by definition $\sigma_{e-\max} = S_y$, which gives $C = p_{oc} / S_y$. The maximum von Mises stress occurs beneath the surface at some location, z, which varies with p_o. However, the value of C is determined for the ratio of z/a (a being the contact radius) and thus is independent of z by itself. The same is true for the locus of maximum von Mises stress, i.e., $\zeta_c = \zeta_m$. To obtain the critical interference the value of p_o is replaced with CS_y in Eq. (1), and solving Eq. (4, 5) gives

$$\omega_c = \left(\frac{\pi C S_y}{2E'} \right)^2 R \quad ; \quad P_c = \frac{\left(\pi C S_y \right)^3 R^2}{6E'^2} \quad ; \quad a_c = \frac{\pi C S_y R}{2E'} \tag{12}$$

where $CS_y = \min\left(C(\nu_1) S_{y1}, C(\nu_2) S_{y2} \right)$, accounting for the possibility of two different material properties. The above parameters are useful for design purposes as well as for the calibration and convergence of FEA codes (to be discussed below). Another useful parameter is the potential (strain) energy stored during elastic deformation, equaling to the work done

$$U = \int P d\omega = \frac{8}{15} E' R^{1/2} \omega^{5/2}$$
$$= \int P \frac{d\omega}{dP} dP = \frac{1}{5} \left(\frac{9P^5}{2E'^2 R} \right)^{(1/3)}$$

The result is expressed by either the deflection (interference), or load. Substituting Eq. (12) in the above results in the maximum elastic energy that can possibly be stored (i.e., on the verge of yielding, or plastic deformation)

$$U_c = \frac{\left(\pi C S_y\right)^5 R^3}{60 E'^4} \tag{13}$$

In the above it is idealized that linear elasticity prevails to yielding. While the strain energy is given for the entire conjunction that includes both elastic bodies, it is apportioned amongst them based upon their relative stiffness.

Critical Values for Cylindrical Contact (2D)

This is only a concise summary of the analysis by Green [28], and the nomenclature and references herein are consistent with that work. Let *x* be the axis along the line of contact, the *y* axis is tangent to the two cylinders, and the *z* axis is the coordinate into the cylinders. Subject to normal loading the maximum (and principal) stresses occur at *x=y=0*. Under a total load per unit length, *P/L*, maximum pressure is generated at the origin

$$p_o = \frac{2P}{\pi b L} \tag{15}$$

where the Hertzian half-width is given by:

$$b = \left(\frac{4(\lambda_1 + \lambda_2) P R_1 R_2}{L(R_1 + R_2)} \right)^{1/2} = \left(\frac{4PR}{\pi L E'} \right)^{1/2} ; \; \lambda_i = \frac{1 - \nu_i^2}{\pi E_i} ; \quad i = 1, 2 \tag{16}$$

Now defining $\zeta = | z / b |$, then the stresses for cylindrical contact are

$$\sigma_y = \left(2\zeta - \sqrt{1 + \zeta^2} \left(2 - \frac{1}{1 + \zeta^2} \right) \right) p_o \tag{17}$$

$$\sigma_z = -\frac{p_o}{\sqrt{1+\zeta^2}} \tag{18}$$

These two stresses are calculated in either material 1 or 2, where only $\zeta \geq 0$ is allowed in both materials, noting that both stresses are independent of Poisson's ratio. Assuming the state of plain strain then the transverse stress is $\sigma_x = \nu(\sigma_z + \sigma_y)$ which reduces to,

$$\sigma_x = 2\left(\zeta - \sqrt{1+\zeta^2}\right)\nu\, p_o \tag{19}$$

The discussion is limited to the range *0 ≤ ν ≤ 1/2*. Conveniently, letting ζ approach zero leads to a bi-axial stress state (i.e., plane stress). The maximum von Mises stress, σ_e, normalized by the contact pressure, p_o, is calculated by,

$$\frac{\sigma_e}{p_o} = \sqrt{\frac{\left[1-2\zeta\left(\sqrt{1+\zeta^2}-\zeta\right)\right]\left[1+4\zeta^2+4\left(1+\zeta^2\right)(\nu-1)\nu\right]}{1+\zeta^2}} \tag{20}$$

The above varies with ζ, where ν is a parameter. The maximum von Mises stress is obtained from $d(\sigma_e / p_o)/d\zeta = 0$. Defining, $C = p_o / \sigma_{e-\max}$, results in $C = C(\nu)$, and the analysis of which gives the following:

$$\begin{aligned} C &= \frac{1}{\sqrt{1+4(\nu-1)\nu}} && \nu \leq 0.1938 \\ C &= 1.164 + 2.975\,\nu - 2.906\,\nu^2 && \nu > 0.1938 \end{aligned} \tag{23}$$

This value of *C* is valid for as long as the material is elastic, i.e., up to yielding onset. This value is used to calculate critical parameters. The maximum deformation in a cylindrical line contact is given by

$$\omega = \frac{1}{\pi E'}\frac{P}{L}\left[\ln\left(\frac{4\pi E' R}{P/L}\right)-1\right]$$

Using the distortion energy (von Mises) theory to predict yielding onset, then with the aid of the definition of *C*, the critical values for force per unit length, interference, and half-width are derived,

$$\frac{P_c}{L} = \frac{\pi R\left(CS_y\right)^2}{E'} \; ; b_c = \frac{2R(CS_y)}{E'} \; ; \; \omega_c = R\left(\frac{CS_y}{E}\right)^2\left[2\ln\left(\frac{2E'}{CS_y}\right)-1\right] \tag{24}$$

where $CS_y = \min\left(C(\nu_1)S_{y1}, C(\nu_2)S_{y2}\right)$ accounts for the possibility of two different material properties. The maximum potential (strain) energy per unit length that can possibly be stored (up to the point of yielding onset) is

$$\frac{U_c}{L} = \frac{\pi\left(CS_y\right)^4 R^2}{4E'^3}\left\{4\ln\left[\frac{2E'}{CS_y}\right]-3\right\} \tag{25}$$

REFERENCES

1. Fair, H.D., *Electric Launch Science and Technology in the United States.* IEEE TRANSACTIONS ON MAGNETICS, 2003. **39**(1): p. 11-17.

2. Chen, J., et al., *Stress analysis of the human temporomandibular joint.* Medical Engineering & Physics, 1998. **20**(8): p. 565.

3. Liu, G., Q.J. Wang, and C. Lin, *A Survey of Current Models for Simulating the Contact between Rough Surfaces.* Tribology Transactions, 1999. **42**: p. 581-591.

4. Thomas, T.R., *Rough Surfaces.* 1982.

5. Greenwood, J.A., *A unified Theory of Surface Roughness.* Proceedings of the Royal Society of London, A, 1984. **393**: p. 133-157.

6. Greenwood, J.A. and J.B.P. Williamson, *Contact of Nominally Flat Surfaces.* Proceedings of the Royal Society of London. Series A, Mathematical and Physical Sciences, 1966. **295**(1442): p. 300-319.

7. Greenwood, J.A. and J.H. Tripp, *The Elastic Contact of Rough Spheres.* ASME Journal of Applied Mechanics, 1967. **34**: p. 153-159.

8. Lo, C.C., *Elastic Contact of Rough Cylinders.* Int. J. Mech. Sci., 1969. **11**: p. 105-115.

9. Whitehouse, D.J. and J.F. Archard, *The Properties of Random Surface of Significance in their Contact.* Proceedings of the Royal Society of London, A316, 1970: p. 97-121.

10. Tsukizoe, T. and T. Hisakado, *On the Mechanism of Contact between Metal Surfaces: Part 2 - The Real Area and the Number of Contact points.* ASME Journal of Lubrication Tribology, 1968. **F90**: p. 81-90.

11. Bush, A.W., R.D. Gibson, and T.R. Thomas, *The Elastic Contact of Rough Surfaces.* Wear, 1975. **35**: p. 87-111.

12. Bush, A.W., R.D. Gibson, and G.P. Keogh, *Strong Anisotropic Rough Surface.* ASME Journal of Tribology, 1979. **101**: p. 15-20.

13. Abbot, E.J. and F.A. Firestone, *Specifying Surface Quality - A Method Based on Accurate Measurement and Comparison.* Mechanical Engineering, 1933. **55**: p. 569.

14. Chang, W.R., I. Etsion, and D.B. Bogy, *Elastic-Plastic Model for the Contact of Rough Surfaces.* Journal of Tribology, Transactions of the ASME, 1987. **109**(2): p. 257.

15. Evseev, D.G., B.M. Medvedev, and G.G. Grigoriyan, *Modification of the Elastic-Plastic Model for the Contact of Rough Surfaces.* Wear, 1991. **150**: p. 79-88.

16. Chang, W.R., *An Elastic-Plastic Contact Model for a Rough Surface with an Ion-Plated Soft metallic Coating.* Wear, 1997. **212**: p. 229-237.

17. Zhao, Y.W., *An Asperity Microcontact Model Incorporating the Transition from Elastic Deformation to Full Plastic Flow.* ASME Journal of Tribology, 2000. **122**: p. 86-93.

18. Vu-Quoc, L., X. Zhang, and L. Lesburg, *A Normal Force-Displacement Model for Contacting Spheres Accounting for Plastic Deformation: Force-Driven Formulation.* ASME Journal of Applied Mechanics, 2000. **67**: p. 363-371.

19. Kogut, L. and I. Etsion, *Elastic-plastic contact analysis of a sphere and a rigid flat.* Journal of Applied Mechanics, Transactions ASME, 2002. **69**(5): p. 657.

20. Jackson, R.L. and I. Green. *A finite element study of elasto-plastic hemispherical contact*. 2003. Ponte Vedra Beach, FL, United States: American Society of Mechanical Engineers, New York, NY 10016-5990, United States.

21. Wang, F. and L.M. Keer, *Numerical simulation for three dimensional elastic-plastic contact with hardening behavior.* Journal of Tribology, 2005. **127**(3): p. 494.

22. Hamilton, G.M. and L.E. Goodman, *The Stress Field Created by a Circular Sliding Contact.* Journal of Applied Mechanics, 1966. **33**: p. 371-376.

23. Hamilton, G.M., *Explicit equations for the stresses beneath a sliding spherical contact.* Proceedings of the Institution of Mechanical Engineers, Part C (Mechanical Engineering Science), 1983. **197**: p. 53.

24. Kogut, L. and I. Etsion, *A semi-analytical solution for sliding inception of a spherical contact.* Journal of Tribology, 2003. **125**(3): p. 499.

25. Faulkner, A. and R.D. Arnell, *Development of a finite element model to simulate the sliding interaction between two, three-dimensional, elastoplastic, hemispherical asperities.* Wear, 2000. **242**(1): p. 114.

26. Nosonovsky, M. and G.G. Adams, *Steady-state frictional sliding of two elastic bodies with a wavy contact interface.* Journal of Tribology, Transactions of the ASME, 2000. **122**(3): p. 490.

27. Johnson, K.L., *Contact Mechanics.* Cambridge University Press, 1985.

28. Green, I., *Poisson Ratio Effects and Critical Values in Spherical and Cylindrical Hertzian Contacts.* International Journal of Applied Mechanics, 2005. **10**(3): p. 451-462.

29. Jackson, R., I. Chusoipin, and I. Green, *A finite element study of the residual stress and deformation in hemispherical contacts.* Journal of Tribology, 2005. **127**(3): p. 484.

30. Boucly, V., D. Nelias, and I. Green, *Modeling of the Rolling and Sliding Contact Between Two Asperities Part II: Hemispherical Sliding Contact.* Journal of Tribology, 2006. **Submitted**.